Downloaded from orbit.dtu.dk on: Dec 17, 2017

Technical University of Denmark

Integration of Nanocomponents in Microsystems

Kjelstrup-Hansen, Jakob; Brandbyge, Mads; Bøggild, Peter

Publication date:
2007

Document Version
Publisher's PDF, also known as Version of record

Link back to DTU Orbit

Citation (APA):
Kjelstrup-Hansen, J., Brandbyge, M., & Bøggild, P. (2007). Integration of Nanocomponents in Microsystems.

DTU Library
Technical Information Center of Denmark

General rights
Copyright and moral rights for the publications made accessible in the public portal are retained by the authors and/or other copyright owners and it is a condition of accessing publications that users recognise and abide by the legal requirements associated with these rights.

- Users may download and print one copy of any publication from the public portal for the purpose of private study or research.
- You may not further distribute the material or use it for any profit-making activity or commercial gain
- You may freely distribute the URL identifying the publication in the public portal

If you believe that this document breaches copyright please contact us providing details, and we will remove access to the work immediately and investigate your claim.

Integration of Nanocomponents in Microsystems

Ph.D. Thesis
MIC - Department of Micro and Nanotechnology
Technical University of Denmark

Jakob Kjelstrup-Hansen

September 30, 2006

Preface

This thesis has been submitted as a partial fulfillment of the requirements to obtain the Ph.D. degree at the Technical University of Denmark (DTU). The main part of the work has been carried out at MIC - Department of Micro and Nanotechnology at DTU from October 1, 2003 to September 30, 2006. A smaller part has been performed at the Department of Physics and Astronomy at the University of North Carolina (UNC), USA.

During this project period I have been part of the Nanointegration group. The project has been supervised by Associate Professor Peter Bøggild and was financed by DTU through a grant within the Electronics and Communication program. Apart from this thesis, a number of other publications have also been made during this project. These are listed in appendix A.

I am grateful to a large number of people for their help, support, and collaboration during this project. First and foremost, I would like to thank Peter Bøggild for his tremendous support, both scientifically as well as personally. The members of the Nanointegration group - present as well as previous - have also been a great help. In particular, I wish to thank Kristian Mølhave for his never failing enthusiasm and for his help on numerous problems. Also, I am grateful to Kjetil Gjerde for great collaboration and for countless discussions on quite a few topics. In addition, I would like to thank Maria Dimaki for initially teaching me the ropes of mask design and process recipe development. I also thank Lauge Gammelgaard for his help on numerous microfabrication questions and Ramona Mateiu for her help with proof-reading of this thesis.

I am grateful to Horst-Günter Rubahn from the University of Southern Denmark for our collaboration and for his help and support with the work on organic nanofibers. A special thank goes to Henrik Henrichsen for great collaboration and interesting discussions.

During his visit to MIC in 2004, Russell Taylor from UNC helped setting up a system for tool motion control in our manipulation set-up, for which I am very grateful. Also, I would like to thank Russell for inviting me to stay in his home during my visit to North Carolina. I would like to thank Richard Superfine for inviting me to visit his group at UNC and Michael Falvo for helping with the experimental challenges.

Several people at MIC have given their help and support. In particu-

lar, I would like to thank Ole Hansen for answering questions on several topics. Also, I wish to thank Mads Brandbyge for discussions on a number of theoretical subjects. The staff at DANCHIP has been a great help with the microfabrication aspects of this work. Especially Helle Vendelbo Jensen deserves my gratitude for helping with the practical cleanroom work.

During my project period, I have had the privilege to (co-)supervise a number of student projects, which has been very rewarding. Trying to answer apparently straight-forward questions is sometimes difficult and can prompt additional scrutiny of the problem and thereby a deeper understanding. I would in particular like to acknowledge Casper Hyttel Clausen and Daniel Engstrøm for their work and collaboration during their master projects towards the end of my own project.

Finally, I want to thank my family and friends for their invaluable encouragement and support.

September 30, 2006

Jakob Kjelstrup-Hansen
MIC - Department of Micro and Nanotechnology
Technical University of Denmark
Building 345 East
DK-2800 Kgs. Lyngby
Denmark

Abstract

Many nanostructures have special properties that suggest technological applications where each nanostructure must be accurately positioned in a microsystem. Special techniques are required in order to integrate such components and thereby establish an electrically and mechanically reliable connection to the surroundings. This work covers the development and testing of methods to integrate two widely different types of nanostructures, each in relation to a specific application.

Carbon nanotubes have unique mechanical and electrical properties. For example, they have a yield strength that is 100 times that of steel and they can be either semiconducting or metallic depending on their geometric structure. These special properties have led to the fabrication of for example sensors and transistors. In this project, the possibility is explored of using a multi-walled carbon nanotube as a strain gauge instead of a microfabricated silicon sensor in a microcantilever-based sensing system. For this purpose, a 3-D micro- and nanomanipulation set-up has been constructed, which can be used for integration of nanocomponents in prefabricated microsystems during the prototyping phase. Using this set-up, individual carbon nanotubes have been integrated in microcantilever systems and characterized. A small part of the investigated sensors had a sensitivity comparable to or larger than that of similar silicon sensors. However, it is concluded that it is not worthwhile to use multi-walled carbon nanotubes due to too large variations in performance and too large intrinsic noise caused by the minute size, unless an extremely small sensor is required.

A further challenge is to fabricate more devices than manipulation can facilitate. For this purpose, a parallel integration method is required that can facilitate wafer scale fabrication. This could be in-situ growth, where the nanotube is synthesized from a catalyst particle that already has been placed at the desired position in the microsystem. This has been investigated by developing and fabricating microsystems with integrated catalyst particles and by constructing and optimizing a chemical vapor deposition system for nanotube growth.

Organic nanofibers consisting of *para*-hexaphenylene molecules stacked in a crystal structure can potentially be used for the fabrication of a nanoscale light source. However, these nanofibers are much more fragile than

carbon nanotubes which makes mechanical handling difficult. Their mechanical properties have been investigated and particularly gentle manipulation methods, which facilitate integration, have been developed.

Light emission from a organic semiconductor can occur through *electroluminescence* in which an electron-hole pair recombines and emits a photon. This requires injection of both electrons and holes from a cathode and anode, respectively. Here, the charge injection and transport properties of individual nanofibers with metal contacts have been investigated. The use of either gold, aluminum, or chromium results in injection-limited current, i.e. the contact rather than the nanofiber bulk is the main current limiting factor. Of the investigated metals, gold has the best hole injection properties, while a suitable cathode material, which can inject an electron current of similar magnitude, is still not found.

Dansk Resumé

En række nanostrukturer har specielle egenskaber, der lægger op til teknologiske anvendelser, hvor den enkelte nanostruktur skal placeres meget præcist i et mikrosystem. For at kunne integrere sådanne komponenter og derved etablere elektrisk og mekanisk pålidelig forbindelse til omverdenen kræves specielle teknikker. Denne afhandling omhandler udvikling og afprøvning af metoder til at integrere to vidt forskellige typer nanostrukturer, hver især i relation til en konkret applikation.

Kulstof nanorør har unikke mekaniske og elektriske egenskaber. De har for eksempel en brudstyrke, der er 100 gange større end brudstyrken af stål, og de kan være enten halvledende eller metalliske afhængig af deres geometriske struktur. Disse specielle egenskaber har givet anledning til fabrikation af for eksempel sensorer og transistorer. I dette projekt undersøges muligheden for at benytte et flervægget kulstof nanorør som strain gauge i stedet for en mikrofabrikeret silicium sensor i et mikrobjælke-baseret målesystem. Til det formål er der konstrueret en opstilling til 3-D mikro- og nanomanipulation, som kan bruges til integration af nanokomponenter i præfabrikerede mikrosystemer under prototype-fasen. Ved hjælp af denne opstilling er individuelle kulstof nanorør blevet integreret i mikrobjælkesystemer og karakteriseret. En mindre del af de undersøgte sensorer havde en følsomhed, der var sammenlignelig med eller overgik tilsvarende silicium sensorer, men alt i alt er konklusionen, at det ikke kan betale sig at anvende flervæggede kulstof nanorør på grund af for store variationer i performance og for stor intrinsisk støj på grund af den ringe størrelse, medmindre der stilles krav om en ekstremt lille sensor.

En yderligere udfordring er at kunne fremstille større styktal end manipulation tillader. Til det formål behøves en parallel integrationsmetode, der kan muliggøre fabrikation på wafer-skala. Dette kunne være *in-situ* dyrkning, hvor nanorøret bliver syntetiseret fra en katalysepartikel, der i forvejen er placeret det ønskede sted i mikrosystemet. Dette er undersøgt ved at udvikle og fabrikere mikrosystemer med indbyggede katalysepartikler og ved at konstruere og optimere et chemical vapor deposition system til dyrkning af nanorør.

Organiske nanofibre bestående af *para*-hexaphenylen molekyler arrangeret i en krystalstruktur kan potentielt bruges til fremstilling af en

nanoskala lyskilde. Dog er disse nanofibre meget mere skrøbelige end kulstof nanorør, hvilket gør mekanisk håndtering vanskelig. Deres mekaniske egenskaber er blevet undersøgt og særligt skånsomme manipulationsmetoder, som muliggør integration, er blevet udviklet.

Lysudsendelse fra en organisk halvleder kan ske gennem *elektroluminescens*, hvor et elektron-hul-par rekombinerer og derved udsender en foton. Dette kræver injektion af både elektroner og huller fra hhv. en katode og en anode. Her er egenskaberne omkring ladnings-injektion og -transport i individuelle nanofibre med metalkontakter blevet undersøgt. Brugen af enten guld, aluminium eller krom resulterer i injektionsbegrænset strøm, dvs. kontakten snarere end nanofiberen selv er den væsentligste strømbegrænsende faktor. Ud af de undersøgte metaller har guld de bedste hul-injicerende egenskaber, mens et passende katodemateriale, som kan injicere en elektronstrøm af samme størrelsesorden, endnu ikke er fundet.

Contents

1 Introduction **11**
- 1.1 A Perspective on Engineering 11
- 1.2 Nanostructures as Components 12
- 1.3 Methods of Integration 13
- 1.4 Nanocomponent Function 15
- 1.5 Device Development 15
- 1.6 Key Topics 16

2 Nanocomponents **19**
- 2.1 Carbon Nanotubes 20
  - 2.1.1 Geometric Structure 20
  - 2.1.2 Electronic Structure 22
  - 2.1.3 Electrical and Electromechanical Properties 23
  - 2.1.4 Synthesis of Carbon Nanotubes 27
  - 2.1.5 Noise in Carbon Nanotubes 28
- 2.2 Organic Nanofibers 31
  - 2.2.1 Geometric Structure 31
  - 2.2.2 Electronic Structure 33
  - 2.2.3 Electrical and Optical Properties 34
  - 2.2.4 Synthesis of Organic Nanofibers 37

3 Manipulation and Integration **39**
- 3.1 Micro- and Nanomanipulation Forces 39
- 3.2 Manipulation Systems 42
  - 3.2.1 2-D Manipulation Systems 43
  - 3.2.2 3-D Manipulation Systems 45
- 3.3 Components and Tools 48
  - 3.3.1 Component Considerations 49
  - 3.3.2 Tool Selection 49
  - 3.3.3 3-D Manipulation Example 54
- 3.4 Manipulation of Carbon Nanotubes 56
  - 3.4.1 2-D Manipulation of Carbon Nanotubes 56
  - 3.4.2 3-D Manipulation of Carbon Nanotubes 57

3.5 Manipulation of Organic Nanofibers 58
3.5.1 2-D Manipulation of Organic Nanofibers 59
3.5.2 3-D Manipulation of Organic Nanofibers 66
3.6 Integration by Shadow Masking 68
3.7 Summary 72

4 In-situ Growth of Carbon Nanotubes 73
4.1 Microsystem Design and Fabrication 74
4.1.1 Process Recipe Development 76
4.1.2 Process Recipe Tests 80
4.1.3 Improving the Recipe 84
4.2 Nanotube Growth 87
4.2.1 Construction of Chemical Vapor Deposition System . 87
4.2.2 Growth Process 90
4.2.3 Results and Discussion 91
4.3 Summary and Outlook 94

5 Cantilever Sensor with Carbon Nanotube Piezoresistor? 97
5.1 Theory of Piezoresistive Cantilever Sensors 98
5.2 Fabrication and Integration 102
5.2.1 Integration of Si Piezoresistors by Microfabrication . . 102
5.2.2 Fabrication of Cantilevers and Integration of CNTs . . 103
5.3 Performance Comparison 106
5.3.1 Sensitivity 107
5.3.2 Noise 112
5.4 Discussion and Outlook 116

6 Electrical Properties of p6P Nanofibers 119
6.1 Charge Injection and Transport Theory 120
6.1.1 Charge Injection 121
6.1.2 Charge Transport 125
6.2 Experimental Investigations of Electrical Properties 128
6.2.1 Current-Voltage Characteristics 129
6.2.2 Temperature Dependence of the Injection Current . . 133
6.2.3 Influence of UV Light Exposure on Current Flow . . . 135
6.2.4 Additional Experiments 138
6.3 Summary and Outlook 138

7 Conclusions 141
7.1 Outlook 145

A List of Publications 147

B Process Recipe 149

Chapter 1

Introduction

1.1 A Perspective on Engineering

Many Ph.D. theses within the area of small things would start out something like "In 1959 at Caltech, Feynman gave his famous speech *There's Plenty of Room at the Bottom*, where he foresaw..." This thesis will not start like that. Instead it will linger shortly on science fiction.

In 1863 Jules Verne wrote *Paris in the 20th Century*, in which he correctly predicted several modern technological inventions but also an increased barrenness of modern society that seems not far from todays reality. In 1932 Aldous Huxley described an ironic utopia in *Brave New World* with an apparently all-happy and carefree humanity, which, however, is governed by a totalitarian state that controls all aspects of life through advanced technology. Despite being far-fetched, traits of similar ideas have emerged in some societies. In 2002 Michael Crichton wrote *Prey*, which forecasts intelligent, autonomous, self-replicating systems that end up threatening all life on Earth. Some people might argue that such science fiction will never come true, however, they should bear in mind Clarkes 1st 'law', which says "When a distinguished but elderly scientist states that something is possible, he is almost certainly right. When he states that something is impossible, he is very probably wrong."

But why does science fiction turn into science and technology, and what are the consequences? It could seem as if we are more keen on using technology for destruction[1] rather than construction, for narcissistic scrutiny of all men's doings and sayings[2] rather than for exploration, or for building the ultimate soldier[3]. That we are simply using technology to precipitate our ultimate fate. In view of this, it would make sense to stop.

However, one could also choose a less pessimistic view. Despite the fact

[1] http://en.wikipedia.org/wiki/Manhattan_Project
[2] http://www.nsa.gov/
[3] http://web.mit.edu/isn/

that new technology can be abused, its main purpose is to improve quality of life - such as to detect and cure diseases, or to provide means of communication and education. Given the recent advance of modern societies, it appears that if new technology is used with care, it indeed is beneficial.

1.2 Nanostructures as Components

Much recent technological progress has been founded on microelectronics, which has provided us with the ability to perform complicated calculations fast. It has been revolutionizing in the sense that it has spun entirely new structures in our societies and has had a profound impact on peoples lives.

Nanotechnology has been hailed as the next big 'thing' - a revolution with even more impact than the computer. However, at least part of the technology that today is being characterized as nanotechnology is more evolutionary in character, since a general trend of much of technology development simply has been to scale down. The integrated transistors of modern electronics are almost exclusively fabricated in silicon by a top-down approach. The development in this field has primarily relied on advancing the present top-down fabrication methods for example by developing lithography techniques capable of ever smaller line widths. However, two aspects are suggesting the introduction of a different kind of components that are not made by a conventional top-down approach. First, it becomes increasingly difficult to control the fabrication processes as the dimensions of the components shrink. For instance, as the channel width of a field-effect transistor shrinks to few tens of nanometers, the exact position of the dopant atoms becomes increasingly important and they can no longer just be treated on a statistical basis. Second, advances in chemical synthesis has enabled the fabrication of a range of self-assembled macromolecules - or nanostructures - with unique properties. Of particular interest is the fact that such synthesis techniques can provide control of size, shape and composition - in principle at the atomic level. Two of the most important nanostructures are carbon nanotubes[1] and inorganic semiconducting nanowires[2], which in combination have a variety of interesting properties in both the electrical, mechanical, and optical domain as well as in overlapping domains such as the electro-mechanical and the electro-optical. However, also less well-investigated nanostructures exist such as biologically inspired nanotubes[3] and organic crystalline nanofibers[4] with equally appealing properties.

Making use of such nanostructures requires the ability to interface these, i.e. to excite these and probe their response. This could for instance be realized by integrating these in a top-down fabricated microsystem to establish electrical contact. Here, integration means placing individual nanostructures at desired positions and creating the necessary interface with the surrounding circuitry, thus turning these nanostructures into nanocomponents.

1.3 Methods of Integration

Conventional top-down fabrication methods allow us to define, deposit, etch, and thus construct very small structures typically on a silicon platform. Chemical synthesis techniques can produce millions or billions of engineered, self-assembled nanostructures. A major challenge lies in bringing these two domains together, i.e. in integrating nanocomponents in microsystems[4]. Where chemical synthesis typically produces a vast amount of nanostructures with less concern about the exact position of the individual units, the concept of using such structures as components calls for this kind of control. Therefore, techniques to controllably position and interface individual nanocomponents in microsystems should be developed.

A significant number of different integration methods have been developed, which can be broadly divided into four classes: 1) Random positioning, 2) Semi-controlled positioning, 3) Controlled positioning, and 4) In-situ fabrication. Fig. 1.1 shows examples from each of these four classes of methods.

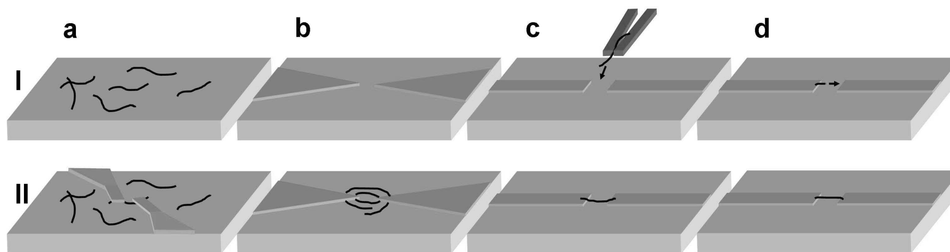

Figure 1.1: Conceptual illustrations of examples from each of the four classes of integration methods. (a) The nanocomponents are dispersed randomly on a pristine substrate. A suitable component is located and custom-designed electrodes are made. (b) Semi-controlled positioning can be realized by attracting nanocomponents from a liquid dispersion towards electrodes using electric fields. (c) Mechanical manipulation can be used to controllably position nanocomponents at specific positions in a microsystem such as between two electrodes. (d) In-situ growth can facilitate component fabrication directly at the desired position in the microsystem.

1. **Random positioning** Some of the first investigations of the electrical properties of carbon nanotubes used randomly positioned nanotubes. The nanotubes are dispersed in solution and deposited on a substrate with prepatterned alignment markers. A suitable nanotube is located,

[4]Heinrich Rohrer: *The Challenges of Nanotechnology*, Talk given at TNT05, September 2, 2005, Oviedo, Spain, abstract: `http://www.phantomsnet.net/files/abstracts/TNT2005/TNT05_kEYNOTE_Rohrer.pdf`

and through electron beam lithography and metal evaporation a set of contacts is made[5] as shown in fig. 1.1(a). Alternatively, the nanotube dispersion can be applied to a substrate with a lithographically predefined pattern of metal electrodes. Subsequent imaging can locate an individual nanotube, which happens to bridge a set of electrodes and which can then be electrically characterized[6, 7].

2. **Semi-controlled positioning** Less random methods, where the position of the components is better controlled, have also been developed. One possibility is to use fluidic alignment to orient several nanocomponents before contacting these via lithographic techniques[8]. Another option is to selectively position the nanocomponents on a chemically patterned substrate[9]. A third method (dielectrophoresis) uses electric fields to guide nanotubes dispersed in a liquid medium towards predefined electrodes[10] as depicted in fig. 1.1(b).

3. **Controlled positioning** The methods of the second class provide some control of nanocomponent position but their stochastic nature results in an inherent randomness in the exact position and number of the components. More controlled positioning is possible through mechanical manipulation. It has been shown how a carbon nanotube can be positioned between two electrodes by sliding it along a surface (2-D manipulation)[11]. Mechanical manipulation can also be extended to 3 dimensions[12] to facilitate pick-and-place operations for example to position a nanocomponent between electrodes as shown in fig. 1.1(c).

4. **In-situ fabrication** The last class of methods employs in-situ growth of nanocomponents in a microsystem. These methods typically use catalytic particles, from which the nanocomponent can grow often via a vapor deposition process as depicted in fig. 1.1(d). An example is chemical vapor deposition of carbon nanotubes, which can be grown between opposing metal electrodes[13] and with the additional option of guiding the growth direction by an applied electric field[14]. In-situ growth can also be used for inorganic nanowires, in which case epitaxy can control the direction[2], while the position can be determined by positioning the catalytic particles prior to nanowire growth[15].

Even though examples can be found, which do not fit exactly into the classes of this scheme, it still gives the possibility to evaluate different generic methods and compare them to one another. The 'random' methods work on planar substrates and have the advantage of providing relatively fast means of constructing a few prototype devices to study component properties. However, the random nature limits the possibilities in terms of high-volume fabrication. The second class of methods also requires a planar substrate and some additional processing to realize the positioning system.

However, the more controlled positioning is desirable from an application-oriented point of view since it can allow parallel device fabrication. Controlled positioning via mechanical manipulation can be advantageous in particular cases such as positioning in a 3-D microsystem. Also, it can be used to position components in prefabricated microsystems which is preferred in situations where post processing can have damaging effects. The fourth and final strategy has the advantage of eliminating both the randomness of the first strategies and the serial component positioning step of the third, and it is fairly straight-forward to develop into a parallel process for high-volume fabrication. However, it requires a microsystem that can withstand and in some cases facilitate the nanocomponent fabrication typically by having prefabricated catalytic particles to define the nanocomponent positions.

1.4 Nanocomponent Function

Integration of nanocomponents in microsystems can enable engineering of a new class of components where the functionality can be designed at the atomic level. An interesting class of nanocomponents are those with semiconducting properties, which can be used in nanoscale transistors - for example based on semiconducting single-walled carbon nanotubes (SWCNTs) [16] or inorganic nanowires[17]. Another related area, where nanocomponents can offer distinct advantages, is as chemical sensors. A SWCNT has all its atoms located at its surface. If a particular kind of molecule can be made to bind specifically to the nanotube, such a binding event could alter its electrical properties thus creating a signal that can be read out. Since a SWCNT is 'all surface', this has the potential of being a very sensitive chemical sensor[18]. A third interesting nanocomponent function is light emission. A nanoscale light-emitting device (LED) could for example have applications in optoelectronic or photonic circuitry[19]. This function has been demonstrated with different nanocomponents such as two crossed nanowires[17], a single nanowire with built-in p-n junction[20], or a SWCNT[21].

1.5 Device Development

Development of a device based on nanocomponents requires consideration of the three aforementioned aspects: component, integration, and function. However, since these factors influence each other, it is necessary during device development to also consider their interaction as illustrated in fig. 1.2. Most nanocomponent devices can be characterized with the framework provided by fig. 1.2, where a particular device can be described by: 1) the type of nanocomponent(s), 2) the method used for integration of the nanocomponent(s), and 3) their function. Fig. 1.3 shows three examples of nanocomponent devices described within this scheme.

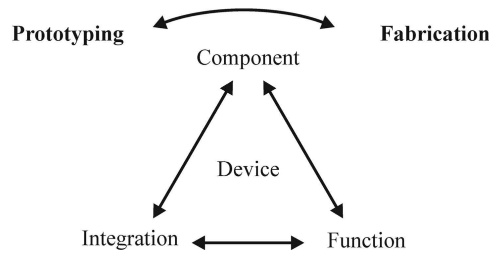

Figure 1.2: The development of a device requires consideration of several aspects. The component(s) will influence the function and the choice of integration method. The function will determine which components and integration methods can to be used. Finally, the technologically available integration methods will affect the choice of components and can have a significant influence on the function. Therefore, a consideration of all aspects is necessary both in the prototyping phase and in a fabrication process.

As indicated in fig. 1.2, this type of consideration applies both for prototyping and for fabrication. The difference between these two primarily lies in the integration methods and in the requirements that are put on these. In both cases the integration methods must provide accurate positioning of the nanocomponent with respect the microsystem and must not damage neither the nanocomponent nor the microsystem. The objective of prototyping is to produce relatively few - but still sufficiently many - devices to investigate and improve their performance. Therefore, the corresponding methods should preferably be as flexible or 'generic' as possible to be able to handle different types of components while the parameters influencing the integration should be tunable to investigate their effect. It should be able to produce a sizeable number of prototype devices, but does not have to be scalable. In contrast, a fabrication method is typically more specific, i.e. it focusses on one particular type of component, but it must then be capable of producing a much larger number of devices.

1.6 Key Topics

The basis of this thesis will be the concepts illustrated in fig. 1.2 with particular emphasis on two different components, two different integration methods, and two different functions. These six areas have been selected under consideration of their individual relationship. The two components will be multi-walled carbon nanotubes (MWCNTs) and organic crystalline nanofibers[4]. From the point of view of investigating integration methods, these two components complement each other nicely. The nanotubes are very robust structures that can sustain significant external load both in

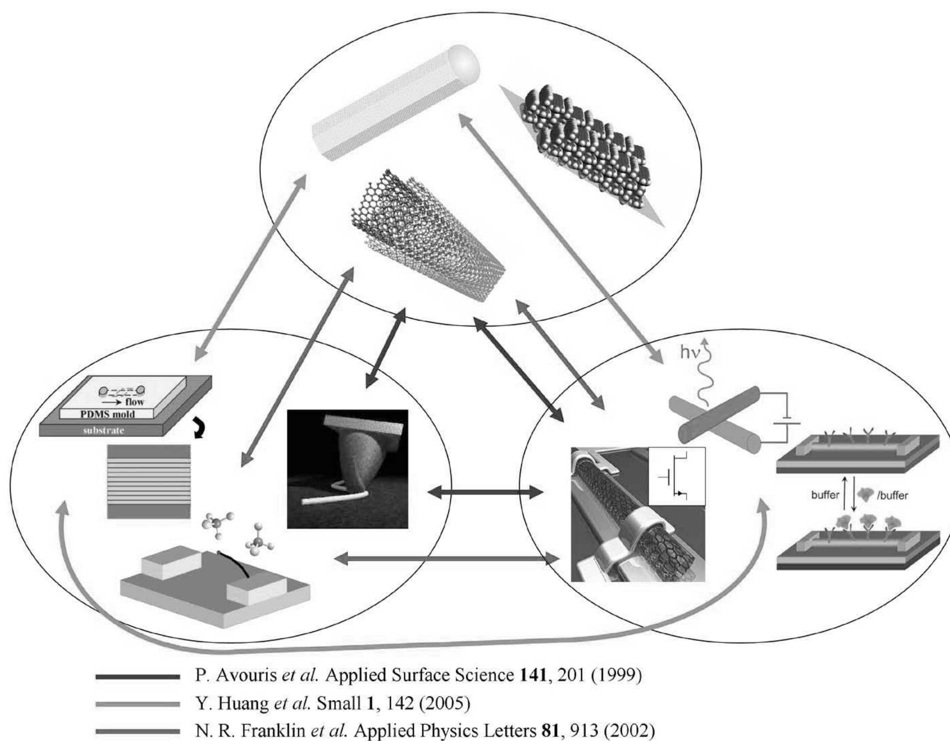

Figure 1.3: A particular nanocomponent device can be characterized as a set consisting of: {component, integration, function}. The examples here are carbon nanotube transistors produced either by mechanical manipulation[11] or in-situ growth[13], or nanoscale LEDs made by fluidic assembly of inorganic nanowires[22]. Illustrations adapted from [8, 23], Science Magazine vol. 294 no. 5545, and http://www.research.ibm.com/.

the mechanical, thermal, chemical and electrical domain. Most integration methods can therefore be applied to nanotubes including different types of lithography, manipulation, fluidic alignment, dielectrophoresis, and in-situ growth. In contrast, the nanofibers are significantly more fragile thus placing severe constraints on the integration method and thereby significantly limiting the number of possible methods. Chapter 2 will describe these two different nanostructures.

The two integration methods are also chosen so they complement each other. The first is mechanical manipulation for precise positioning of a nanocomponent in a prefabricated microsystem. This is a quite general method that can be applied to different types of nanocomponents. The mechanical manipulation method will therefore be examined both for MWCNTs and for organic nanofibers - both as a method for nanocomponent positioning but also in terms of investigating mechanical properties. This includes the

construction of a manipulation set-up and an evaluation of manipulation tools and strategies, and will be the topic of chapter 3.

The second integration method is in-situ growth. This has a better potential of high-volume device fabrication but it is also more specific to a particular nanostructure. Chapter 4 describes investigations of the prerequisites for using in-situ growth as a method for integrating a MWCNT between electrodes on a microcantilever. This involves fabrication of a suitable microcantilever system and construction and testing of a chemical vapor deposition system for nanotube growth.

The next two chapters treat particular aspects of MWCNTs and organic nanofibers, respectively, to explore the possibilities of using their intrinsic properties to realize a particular function. Carbon nanotubes have been shown to change their electrical properties significantly when exposed to mechanical strain[24]. This suggests that it should be possible to construct a miniaturized strain sensor with a high sensitivity based on a carbon nanotube. This is investigated in chapter 5 by considering a specific application: the use of a MWCNT as a strain sensor in a microcantilever system as depicted schematically in fig. 1.4(a).

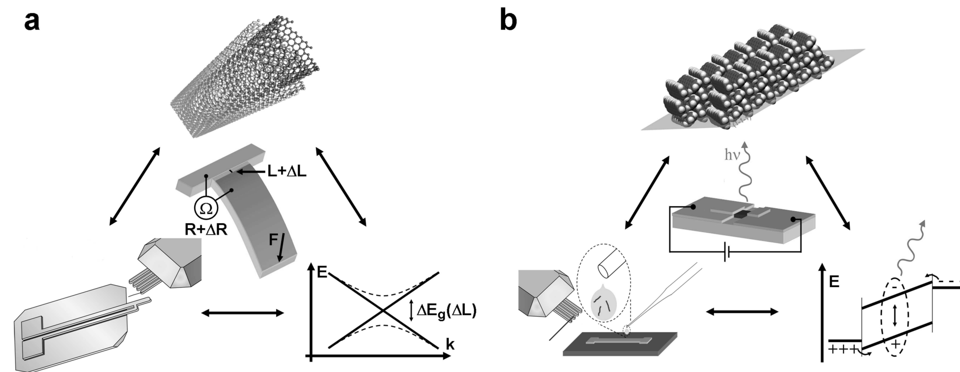

Figure 1.4: The topics of chapter 5 and 6 illustrated within the framework of fig. 1.2. (a) Device 1: Multi-walled carbon nanotube integrated in a microcantilever system for strain sensing. (b) Device 2: Organic nanofiber integrated in a microsystem for light generation.

The final point to be studied is the possibility of using organic nanofibers as components with the ultimate goal of establishing electroluminescence in order to construct a nanoscale LED as illustrated in fig. 1.4(b). The prerequisites for such nanoLED construction are examined by investigating manipulation as an integration method and by investigating charge injection and transport properties of the constructed devices to establish an understanding of these aspects, which are crucial to the process of light generation. This will be the topic of chapter 6.

Chapter 2

Nanocomponents

The term 'nanocomponents' is used here to describe self-assembled rod-like structures with cross-sectional dimensions of tens of nanometers or less. Such structures can have several attractive properties with large potential for applications[25].

Carbon nanotubes (CNTs) were first observed by Iijima in 1991[1]. These are hollow cylinders of one or more rolled-up graphene sheets and display a number peculiar effects such as being mechanically very strong and electrically either metallic or semiconducting depending on the geometric structure. This has stimulated an intense research effort both in exploring their fundamental properties[26] and in applying these in numerous fields such as for high-strength composite material, field-emission displays, sensors, and semiconductor devices and interconnects[27].

Inorganic, crystalline, semiconducting nanowires are a second class of appealing nanostructures. These include a number of different types: elemental nanowires such as silicon or germanium[28] or binary compounds - typically from III-V materials - such as gallium arsenide or indium arsenide[29]. Also more complicated nanowire compositions such as superlattice structures consisting of two alternating materials[20, 30] or core-shell structures[31] have been realized - something that is not possible with carbon nanotubes. Such nanowires could find applications in similar areas to carbon nanotubes as sensors or semiconductor devices. In addition, the ability to fabricate heterostructure nanowires facilitates tailoring of their properties by constructing for example in-wire tunnel barriers[30] or core-shell structures with very low carrier scattering[32].

Apart from these two classes of nanostructures, which have been investigated extensively, a variety of other types of nanostructures exist[33]. One example is peptide nanotubes[34], which are of special interest due to their biocompatibility and possible function as scaffolds for other types of nanostructures such as silver nanowires[3]. Metal nanowires also comprise a significant research area with particular focus on sensing applications[35, 36].

Another example is a class of organic nanofibers made up of small organic molecules stacked in a crystal structure[4]. These nanofibers are of technological interest due to their optical and electro-optical properties[37].

This chapter will introduce the two types of nanocomponents that are investigated in this work: carbon nanotubes and organic nanofibers.

2.1 Carbon Nanotubes

A fascinating aspect of carbon nanotubes is their mechanical properties such as high strength, high stiffness, and low density[38]. Similarly interesting are their electronic properties. A single-walled carbon nanotube can be either metallic or semiconducting depending on the atomic arrangement[39]. Here, an introduction will be provided to set up the required concepts, however, for a broader overview the reader is referred to one of the numerous review articles or books on carbon nanotubes[26, 38, 40, 41, 42].

2.1.1 Geometric Structure

The simplest type of carbon nanotube consists of just one layer of graphene rolled up in the form of a seamless cylinder, known as a single-walled carbon nanotube (SWCNT) with a typical diameter of just a few nanometers. Larger diameter nanotube structures are nanotube ropes, consisting of many individual, parallel nanotubes closed-packed into a hexagonal lattice, and multi-walled carbon nanotubes (MWCNTs) consisting of several concentric cylinders nested within each other. Fig. 2.1 shows transmission electron microscope (TEM) images of both MWCNTs (a-c) and a SWCNT rope (d).

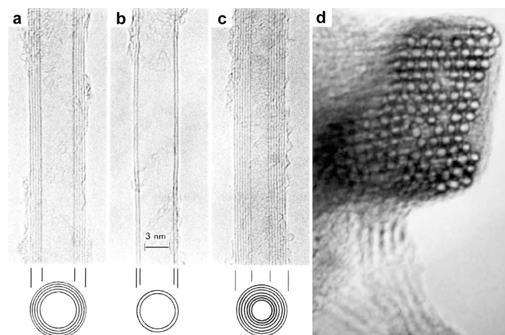

Figure 2.1: TEM images showing side views of (a) a MWCNT with five shells and an outer diameter (OD) of 6.7 nm (b) a MWCNT with two shells and an OD of 5.5 nm (c) a MWCNT with seven shells and an OD of 6.5 nm. Reproduced from [1]. (d) TEM image showing an end view of a rope of SWCNTs, each with a diameter of ∼ 1.4 nm. Reproduced from [43].

The basic configuration is thus the SWCNT. Its structure is most easily illustrated as a cylindrical tube conceptually formed by the wrapping of a single graphene sheet. The hexagonal structure of the 2-dimensional graphene sheet is due to the sp^2 hybridization of the carbon atoms, which causes three directional, in-plane σ bonds separated by an angle of 120°. The nanotube can be described by a chiral vector $\mathbf{C}$ that can be expressed in terms of the graphene unit vectors $\mathbf{a}_1$ and $\mathbf{a}_2$ as $\mathbf{C} = n\mathbf{a}_1 + m\mathbf{a}_2$ with the set of integers (n, m) uniquely identifying the nanotube. This chiral vector or 'roll-up' vector describes the nanotube circumference by connecting two crystallographically equivalent positions i.e. the tube is formed by superimposing the two ends of $\mathbf{C}$. Fig. 2.2(a) illustrates the chiral vector for the case of a $(n, m) = (4, 3)$ nanotube. In addition, it illustrates the chiral angle θ between the chiral vector $\mathbf{C}$ and the zig-zag direction. Based on the chiral angle SWCNTs are defined as zig-zag tubes ($\theta = 0° \leftrightarrow m = 0$), armchair tubes ($\theta = 30° \leftrightarrow n = m$), or chiral tubes ($0° < \theta < 30°$). Examples of the structure of these three types of nanotubes are shown in fig. 2.2(b-d).

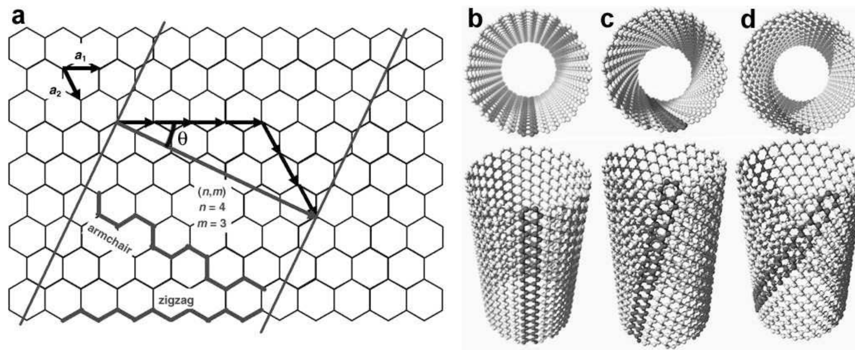

Figure 2.2: (a) The hexagonal lattice of graphene with unit vectors $\mathbf{a}_1$ and $\mathbf{a}_2$ are used to illustrate the structure of a nanotube described by a chiral vector $\mathbf{C} = n\mathbf{a}_1 + m\mathbf{a}_2$. In this example $(n, m) = (4, 3)$. Also shown are the patterns of carbon atoms along the circumference of a zig-zag and an armchair nanotube. Reproduced from [44]. (b) $(n, m) = (13, 13)$ armchair nanotube, (c) $(n, m) = (20, 10)$ chiral nanotube, and (d) $(n, m) = (25, 0)$ zig-zag nanotube. Adapted from http://www.nanoelectronics.jp/freestuff.htm

MWCNTs are composed of a number of SWCNTs in a coaxial geometry as shown in fig. 2.1(a-c). Each nested shell has a diameter of $d = \sqrt{3}a_{C-C}(m^2+n^2+mn)^{1/2}/\pi$ where a_{C-C} is the length of the carbon-carbon bond which is 1.42 Å. The difference in diameters of the individual shell means that their chiralities are different, and adjacent shell are therefore in general non-commensurate, which causes only a weak intershell interaction. The intershell spacing in MWCNTs is ~ 0.34 nm - quite close to the interlayer spacing in turbostratic graphite[42].

2.1.2 Electronic Structure

The electronic structure of a SWCNT is most easily described by again considering a single graphene sheet. The 2-D, hexagonal-lattice graphene sheet has a 2-D reciprocal space with a hexagonal Brillouin zone (BZ) as shown in fig. 2.3(b).

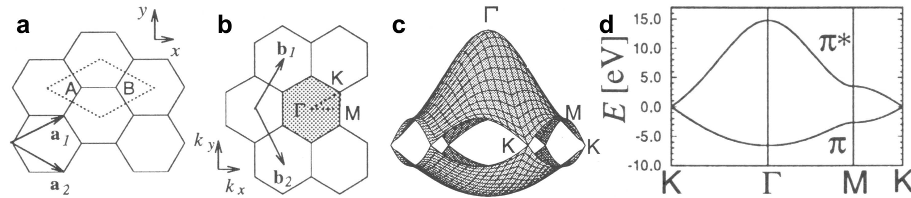

Figure 2.3: (a) The hexagonal lattice of graphene with unit vectors $\mathbf{a}_1$ and $\mathbf{a}_2$. The dotted line indicates the unit cell containing the two carbon atoms A nd B. (b) The reciprocal lattice of graphene with reciprocal lattice vectors $\mathbf{b}_1$ and $\mathbf{b}_2$. The shaded area indicates the Brillouin zone. Also shown are the high symmetry points Γ, K, and M. (c) 3-dimensional rendering of the energy band structure arising from the π bands within the BZ. (d) Energy bands along the high symmetry directions. Reproduced from [41].

The σ bonds are mainly responsible for the mechanical properties, while the electronic properties are mainly determined by the π bands. By a tight-binding approach the band structure of these π bands can be calculated - see fig. 2.3(c-d)[41]. Graphene is a zero-gap semiconductor with an occupied π band and an unoccupied π^* band meeting at the Fermi level at six K points in the BZ, thus it behaves metallic, a so-called semimetal. Upon forming the tube by conceptually wrapping the graphene sheet, a periodic boundary condition is imposed that causes only certain electronic states of those of the planar graphene sheet to be allowed. These states are determined by the tube's geometric structure, i.e. by the indices (n, m) of the chiral vector. The wave vectors of the allowed states fall on certain lines in the graphene BZ as shown in fig. 2.4.

Based on this scheme it is possible to estimate whether a particular tube will be metallic or semiconducting. When the allowed states include the K point, the system will to a first approximation behave metallic. However, as indicated by the open circles in fig. 2.4 the points where the π and the π^* bands meet are shifted slightly away from the K point due to curvature effects, which causes a slight band opening in some cases[39]. This leads to a classification scheme that has three types of nanotubes:

1. **Metallic** These are the armchair tubes where the small shift of the degenerate point away from the K point does not cause a band opening for symmetry reasons. This corresponds to fig. 2.4(b).

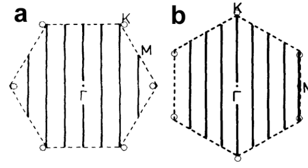

Figure 2.4: (a) The Brillouin zone of graphene (dashed line) with the wave vectors of the allowed states of a $(n, m) = (6, 0)$ zig-zag tube shown as full lines. The open circles show the points where the π and $\pi*$ bands meet. These are slightly offset from the K points due to the curvature of the nanotube. (b) Similar to (a) but for a $(n, m) = (4, 4)$ armchair tube. Adapted from [39].

2. **Small-bandgap semiconducting** These are characterized by $n - m = 3j$ with j being an integer. Here, the wave vectors of the allowed states cross the K point, but due to the slight shift of the degenerate point a small gap will be present, the size of which is inversely proportional to the tube diameter squared with typical values between a few and a few tens meV[45]. This corresponds to fig. 2.4(a).

3. **Semiconducting** In this case $n - m \neq 3j$. This causes a larger bandgap, the size of which is inversely proportional to the tube diameter: $E_g = k/d$ with experimental investigations suggesting a value of k of 0.7-0.8 eV/nm[46, 47].

Typically the bandgap of the type 2 nanotubes is so small that they can be considered metallic at room temperature. Based on this it can be inferred that 1/3 of all tubes should behave metallic whereas the remaining 2/3 should be semiconducting. However, it should be noted that due to the inverse proportionality between the bandgap and the diameter of the semiconducting tubes, large-diameter tubes will tend to behave metallic at room temperature. This is especially important in regards to large-diameter MWCNTs. From a electrical point of view a MWCNT can be seen as a complex structure of many parallel conductors that are only weakly interacting. Since probing the electrical properties typically involves electrodes contacting the outermost shell, this shell will be dominating the transport properties[48]. In a simplistic view, this can be compared to a large-diameter SWCNT, which will therefore typically display metallic behavior.

2.1.3 Electrical and Electromechanical Properties

Many studies have focused on SWCNTs for exploring the fundamental properties of nanotubes. Due to their essentially 1-D nature and intriguing electronic structure, SWCNTs exhibit a range of interesting quantum phe-

nomena at low temperature[26, 42]. The discussion here will, however, primarily be limited to room temperature properties.

The conductance G of a 1-dimensional conductor such as a SWCNT is given by the Landauer formula[49]: $G = (2e^2/h)\sum_i T_i$, where $2e^2/h = (12.9\ \mathrm{k\Omega})^{-1}$ is the conductance quantum G_0 and T_i is the transmission coefficient of the contributing channel i. Since there are two channels at the Fermi level, a metallic SWCNT would have a (low bias) resistance of $h/4e^2 = 6.5\ \mathrm{k\Omega}$ in the absence of scattering ($T_1 = T_2 = 1$)[40], in which case it would behave as a ballistic conductor where the electron mean free path is longer than the device length. In a practical device there will additional contributions to the resistance. Imperfect contacts will cause a contact resistance R_c. Also, scattering events can limit the electron flow, thus giving rise to an additional, ohmic term, inversely proportional to the electron mean free path l_m. A model of the total resistance contains these three terms[50]:

$$R = \frac{h}{4e^2}\left(1 + \frac{l}{l_m}\right) + R_c \tag{2.1}$$

with l being the device length.

Experiments on metallic SWCNTs have demonstrated ballistic transport by electrical transport measurements (in particular at low temperature)[51] and using scanning probe microscopy to investigate the spatial potential distribution[52]. Often electron-phonon scattering limits the mean free path in metallic SWCNTs. In the low-bias regime, l_m is of the order of a few μm whereas much stronger scattering occurs at higher bias thus limiting the mean free path down to ~ 10 nm[53]. In this high bias regime, the scattering causes the current to saturate around 20 μA for increasing voltages[54]. Semiconducting SWCNTs are often investigated in a field-effect transistor (FET) configuration as first reported in 1998[16]. In this scheme a gate voltage is used to control the current flow either by altering the Schottky barriers at the contact-nanotube interface[55] or by changing the electrostatic potential of the nanotube bulk[56], thus enabling switching between ON and OFF states similar to the function of conventional Si based FETs.

MWCNTs are complex composite structures consisting in general of both metallic and semiconducting shells. Therefore, much experimental research has focused on the more well-defined SWCNTs. However, from an integration point of view, SWCNTs are significantly more troublesome due their very small diameter of typically just a few nm, which makes handling and positioning of individual nanotubes difficult. This makes MWCNTs an interesting alternative since many of the same properties must be anticipated.

Ballistic transport has been observed in MWCNTs where the conductance was found to be quantized typically at integer values of G_0[48]. Here, the low conductance was attributed to current conduction taking place in just one shell. However, in most cases the transport is diffusive[7, 57]. A

simple estimation of the intrinsic conductance is the Drude model[58]

$$G = \frac{\sigma}{l} = \frac{ne^2\tau}{m^*}\frac{1}{l}, \tag{2.2}$$

where σ is the conductivity, n is the carrier density, τ is the mean free time, and m^* is the effective carrier mass.

The Avouris group has investigated both the low- and the high-bias behavior of MWCNTs[59]. At high bias a current saturation effect is observed similar to the SWCNT case but at significantly higher current values due to the larger cross section. This indicates that at higher bias voltages current is injected into deeper-lying shells and is not limited to the outer shell. This could be due to an energy dependence of the intershell coupling, where electrons are more easily injected into deeper-lying shells at high bias. Their work also demonstrates how electrical breakdown of individual shells can be used to controllably remove the outermost shells in a step-wise fashion and thereby probe the remaining, deeper-lying shells.

The exact nature of the current conduction paths at low bias is less clear. Using the method of alternatingly removing the outermost shell and measuring the low-bias characteristics of the remaining shells, it was shown that part of the current is flowing in the deeper-lying shells also at low bias[59]. However, the low-bias conductance dropped to approx. one tenth of its initial value upon the first breakdown, which indicates that the majority of the current was initially carried by the outermost shell(s). A more recent study probed the intershell conductance by nonlocal four-point measurements[60]. Here, the voltage drop was measured between electrodes placed outside the two current biased electrodes (fig. 2.5(c)). A non-zero nonlocal voltage drop indicates a complex conduction path including deeper-lying shells as shown in fig. 2.5(a). The nonlocal voltage drop shows an exponential dependence on separation distance between current and voltage electrodes with a decay

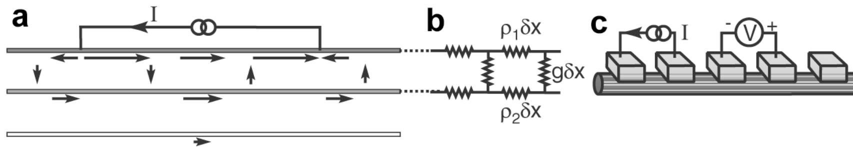

Figure 2.5: (a) The conduction pathways in a MWCNT. The three lines represent the three outermost shells with the current applied to the outermost. Part of the current enters the inner shells which causes the current pathways not to be confined to the area between the electrodes. (b) Transmission line model of the MWCNT including the two outermost shells. (c) The nonlocal voltage is measured between two electrodes located outside the current biased electrodes. Reproduced from [60].

length of $\sim 1\ \mu$m. Thus, when the electrode separation is of the same order, only a negligible part of the current will reach the third shell, and a model containing just the two outermost shells (fig. 2.5(b)) will suffice. The intershell conductivity (g in fig. 2.5(b)) was found to be $\sim (10\ \text{k}\Omega)^{-1}/\mu$m.

The electromechanical properties have primarily been investigated for SWCNTs. Theoretical work has focused on bandgap changes in response to strain (relative elongation). Using a tight-binding approach and neglecting the effect of curvature, the bandgap change with respect to strain $|dE_g/d\epsilon|$ for metallic and semiconducting SWCNTs (type 1 and 3) was found to be[61]

$$|dE_g/d\epsilon| = 3t_0(1+\nu)\cos 3\theta, \tag{2.3}$$

where t_0 is the tight-binding overlap integral ~ 2.66 eV, ν is Poisson's ratio ~ 0.2, and θ is the chiral angle.

A second study included the effect of curvature to investigate the response of small-bandgap semiconducting SWCNTs (type 2)[62][1]

$$|dE_g/d\epsilon| = \frac{3}{2}a_{C-C}b\cos 3\theta, \tag{2.4}$$

where b is the change in overlap integral with bond length ~ 3.5 eV/Å.

From eq. 2.3, metallic (armchair) SWCNTs, which have a chiral angle of 30°, are thus expected not to respond to tensile strain, whereas zig-zag SWCNTs ($\theta = 0°$) will be the most sensitive both in the small-bandgap and in the semiconducting case with bandgap changes of 76 and 96 meV pr % strain, respectively. An important point is that the bandgap change can be either positive or negative, depending on the chiral vector[61].

Using the Landauer formula, the low-bias resistance due to the change in electronic bandgap can be modelled as[63, 64]

$$R(\epsilon) = R_0\left(1+\exp\left(\frac{E_g(\epsilon)}{\alpha k_B T}\right)\right) + R_c, \tag{2.5}$$

where R_0 is a prefactor of the order of $1/G_0$, R_c is the contact resistance, k_BT is the thermal energy, and α is a factor, whose exact value depends on the assumed energetics of the electrode-nanotube interface and which has been suggested to be either 1[63] or 2[64]. Assuming a value of $\alpha = 2$, an estimate of the maximum gauge factor $g = (1/R)(dR/d\epsilon) = (1/R)(dR/dE_g)(dE_g/d\epsilon)$ can be found to be ~ 190 for a zig-zag semiconducting SWCNT assuming negligible contact resistance. Assessing the response in the diffusive regime can be done on the basis of eq. 2.2. The carrier density n is controlled by Fermi statistics, and its value will therefore depend on the bandgap and on the position of the Fermi level. This suggests that an increased bandgap should cause a reduction in the carrier density and thus in the conductivity.

[1] Please note the different definition of chiral angle in [62].

Quantitative modelling would require knowledge of the Fermi level position, which is difficult to predict. In addition, since strain alters the electronic band structure it will most likely influence the effective carrier mass which also will change the conductance. However, these aspects have not been considered further and the attention is turned to experimental investigations.

In a pioneering experiment, Tombler and co-workers used the tip of an atomic force microscope (AFM) to deflect the center part of a SWCNT that was suspended across a trench. This caused the nanotube conductance to reversibly drop by two orders of magnitude when strained up to 3 %[24]. Based on theoretical simulations on an armchair nanotube, it was suggested that this conductance drop was caused by the local deformation of the nanotube just below the AFM tip. It was later suggested that modelling it as a zig-zag rather than an armchair SWCNT could explain the conductance drop as the result of a uniform axial strain that caused a change in the bandgap [65]. The Dai group and the McEuen group simultaneously reported similar studies where a nanotube in a FET configuration was stretched while its electrical properties were probed[63, 64]. These studies indicated that the bandgap change explanation could only partly account for the observed behavior as gauge factors up to ~ 1000 was observed[64] which is comparable to the effect observed by Tombler[24]. Both studies also found that for some nanotubes the conductance increased with strain in agreement with theory. However, both studies also included large local deformations of the nanotube, and it was not possible to rule out that this also contributed to the observed resistance changes. Recently, Stampfer *et al.* have demonstrated a SWCNT based pressure sensor, in which the nanotube exhibited a gauge factor of ~ 210[66].

2.1.4 Synthesis of Carbon Nanotubes

Several methods exist for the fabrication of carbon nanotubes. The first carbon nanotubes were observed in carbon-soot made by an arc-discharge process[1]. Here, a helium plasma is created between two opposing carbon electrodes by passing a high current through, which causes carbon atoms to be evaporated and assemble in different forms including as MWCNTs. The fabrication of SWCNTs requires the presence of a metal catalyst, for instance by having a small amount of cobalt incorporated in the carbon anode[67]. Another method, developed by Smalley and co-workers, also involves evaporating carbon atoms from a carbon target containing small amounts of catalyst[43]. Here, a laser is used for ablating the carbon target in a 1200°C hot tube furnace. An inert gas flow is passed through the furnace during growth to carry the produced nanotubes to a cold-finger, where they can be collected.

A third method, chemical vapor deposition (CVD), involves the decomposition of a hydrocarbon gas aided by a catalyst material, typically a tran-

sition metal[68]. Here, catalyst material is placed in a furnace, which is heated to typically 700-900°C, and a hydrocarbon gas is led through the furnace for a period of time. The hydrocarbon molecules decompose at the catalyst particles where the carbon atoms dissolve in the metal particle. The nanotube growth then occurs by precipitation of carbon atoms from the saturated particle and form nanotube structures. A range of different variants of the CVD method have been used for nanotube growth. For example, a plasma can be used as an additional energy source for the hydrocarbon decomposition, which can then occur at lower temperatures than in a purely thermal process.

An advantage of both the arc-discharge process and the laser ablation method is that they produce nanotubes with very few defects - presumably due to the high reaction temperature of $\geq 3000°C$ which allows the carbon atoms to anneal into perfect crystal structures. For MWCNT growth, the lower reaction temperature of CVD based methods causes a larger concentration of defects[42]. However, CVD based methods provide other advantages. By patterning a catalyst nanoparticle dispersion on a silicon wafer, the Dai group demonstrated how horizontal SWCNTs could be grown at selected positions[69] and later contacted for electrical characterization[70]. Lateral growth between two opposing metallic electrodes has allowed the construction of a nanotube FET[13]. It has also been demonstrated how an applied electrical field during growth can align the nanotubes with the field direction, for instance by using the self-bias field in plasma enhanced CVD to obtain vertically aligned CNTs[71] or using an applied field but no plasma[72]. Lateral growth in a direction determined by an applied electric field has been demonstrated both for supported[14] and suspended[73] SWCNTs as well as suspended MWCNTs[74]. Since CVD growth is facilitated by metallic nanoparticles, electron beam lithography (EBL) can provide control over the exact location of individual catalytic particles and thereby individual nanotubes[75], while the size of the catalytic particle will determine the diameter of the nanotube[76].

However, one of the significant remaining problems is that it is today still not possible to fabricate nanotubes with a predefined geometric and thereby electronic structure. The fabricated nanotubes will therefore in general be a mixture of both metallic and semiconducting. However, it has been demonstrated how particular fabrication methods can produce preferentially semiconducting SWCNTs[77] or how post-processing techniques can be used to sort between metallic and semiconducting nanotubes[10].

2.1.5 Noise in Carbon Nanotubes

When attempting the use of carbon nanotubes as sensors, an important factor is the signal to noise ratio. A poor signal to noise ratio will compromise the sensivity. This aspect is of particular importance in relation to carbon

nanotubes since they have been reported to generate much internal noise.

Mathematically, noise is often described as a spectral noise power density $S_v(f)$, which, according to the Wiener-Kinchine theorem, is found as the Fourier transform of the auto-correlation function $C_V(\tau)$

$$S_V(f) = 4\int_0^\infty C_V(\tau)\cos(2\pi f\tau)d\tau \quad (2.6)$$

$$C_V(\tau) = \langle V(\tau)V(0)\rangle. \quad (2.7)$$

Several types of electrical noise exist, which can broadly be divided into two categories: noise originating from external sources and noise generated internally in the circuit. While the first type can be minimized or even eliminated by careful design of the circuit, the latter is more difficult to circumvent but indeed worth studying, since it might be the main limiting factor.

Thermal Noise

Due to thermal fluctuations of the carriers, a sample with resistance R will exhibit a small fluctuating voltage at its terminals. This is also termed the Johnson or Nyquist noise. The thermal spectral density is given by

$$S_{V,T} = 4k_BTR, \quad (2.8)$$

where k_B is the Boltzmann constant and T is temperature. This does not depend on frequency, which has caused the designation *white noise*.

Shot Noise

At finite bias $I_{DC} \neq 0$ the observed noise will be larger than the value predicted by eq. 2.8. One contributing factor is the shot noise, which is caused by the finite charge of electrons. This leads to a noise contribution of the form

$$S_{V,I} = 2qIR^2, \quad (2.9)$$

where q is the electronic charge and I is the current. Shot noise is usually found in systems where the electrons must pass a barrier such as in Schottky barrier diodes or p-n junctions. In macroscopic resistors shot noise is absent due to electron-phonon scattering smoothing out the fluctuations. However, if the dimensions are reduced, shot noise can be found in resistors also.

$1/f$ Noise

At low frequencies a third type of noise will dominate the frequency spectrum also known as flicker or Hooge noise. A phenomenological equation, which fits the low frequency noise found in many systems was given by Hooge[78]

$$S_{V,1/f} = \frac{\alpha_H}{N}\frac{V^2}{f}, \quad (2.10)$$

where N is the number of free carriers in the sample and α_H is a material constant typically $\sim 2 \cdot 10^{-3}$[79]. Eq. 2.10 has been shown to describe the low frequency noise arising from different physical sources and a general description of its origin is therefore impossible to give and is in many cases not known.

Experimental Investigations of Noise in Nanotubes

The first experimental investigation of noise in nanotubes was carried out by Collins and co-workers[80], who found a very large $1/f$ noise in SWCNTs. They investigated both individual SWCNTs as well as larger nanotube assemblies, and found the $1/f$ voltage noise power for all samples to be approximately described by

$$S_{V,1/f,Collins} = A\frac{V^2}{f^{1.06}} \tag{2.11}$$

with $A = 1.0 \cdot 10^{-11}\Omega^{-1}R$. From this it appeared that the $1/f$ noise in nanotubes is up to 10 orders of magnitude higher than in conventional conductors. It was later suggested that the A/R ratio should depend on device length[81], but apparently still not with the expected scaling dependence with N. Recently, however, the Avouris group has clarified these issues[82] by investigating semiconducting SWCNTs in different FET configurations. Here, different gate designs allowed modulation of the device resistance either by modifying the Schottky barriers at the nanotube/metal interface or by modulating the potential of the nanotube channel, with similar low-frequency fluctuations regardless of switching mechanism. As the gate voltage is used to modulate the device resistance, the noise level increases with resistance in qualitative agreement with eq. 2.11, however, with A/R ratios between $2 \cdot 10^{-10}\Omega^{-1}$ and $2 \cdot 10^{-9}\Omega^{-1}$ (on the same device). Using theoretical modelling, which reproduces the transistor characteristics with a high accuracy, the number of carriers in the nanotube N was estimated at different gate voltages. Using these values of N together with eq. 2.10 and a value of $\alpha_H = 2 \cdot 10^{-3}$ resulted in noise estimations in very good agreement with the measured $1/f$ noise. Thus, the noise level in carbon nanotubes appears not to be intrinsically higher than in other, bulk materials. The large observed values of $1/f$ noise are simply due to the small dimensions causing very few carriers. It must therefore be anticipated that the same relations holds for MWCNTs. A few reports of noise in individual MWCNTs exist such as[83], which observe noise levels comparable to or slightly less than Collins[80]. Shot noise has been investigated in SWCNT ropes[84] where it was found that the shot noise at low temperatures was more than 100 times smaller than predicted by eq. 2.9 and practically absent above 77 K.

2.2 Organic Nanofibers

Nanofibers based on organic molecules have been fabricated in various forms[3, 4, 85]. Here, the focus is on a particular kind: a crystalline nanostructure composed of small, organic, semiconducting molecules[4]. Such nanofibers, which have not been explored quite as comprehensively as the carbon nanotube, but which nonetheless have some appealing features that point towards the potential use as components, have most of the features of 'conventional' large-scale organic semiconductors in addition to those gained from its size.

The investigations of organic nanofibers in this work have been focused on a particular type: *para*-hexaphenylene (p6P) nanofibers. This section will therefore describe this type of nanofiber. However, one of the very intriguing features of such nanofibers is that the individual molecules making up the nanofiber can be tailored through chemical synthesis to possess a particular property[86]. So while the work presented here will be on this specific type, the potential of the techniques developed for its handling and the understanding gained of its properties can reach beyond just this type.

Among the interesting properties of p6P nanofibers are their photoluminescence output, which is in the blue range of the spectrum and is highly polarized[87] due to the molecular structure and the ordering of the molecules in the crystal. A similar nanofiber electroluminescence spectrum is expected from thin-film measurements[88]. In addition, these subwavelength nanofiber structures show waveguiding capabilities[87], can act as laser gain medium[89], and resist most chemical treatment.

Similar to the carbon nanotube section, an introduction to the geometric and electronic structure will be given. This will be followed by a description of the electrical and optical properties. The focus of this chapter will be on the intrinsic properties of p6P itself. In a an actual device, where electrodes have been attached to the p6P nanofiber, additional factors originating from the electrode-p6P interfaces can/will contribute significantly to the device properties. This will be further elaborated in chapter 6.

2.2.1 Geometric Structure

Para-hexaphenylene ($C_{36}H_{26}$) is an aromatic molecule consisting of 6 phenylene rings in a linear chain as depicted schematically in fig. 2.6(a). Similar to the carbon nanotube case, the carbon atoms also hybridize to form the sp^2 hybridization in p6P. The three sp^2 electrons form strong σ bonds, while the remaining p electron makes π bonds that in general are delocalized over the entire molecule. In the gaseous phase the p6P molecules are not planar, rather they have interring torsional angles of 30 - 40°[90]. This is due to two competing forces: the intramolecular repulsion caused by the hydrogen atoms and the delocalized π electron system that tends to planarize the molecule. In the solid phase, however, the molecules crystallize in a planar

configuration[91]. The crystal structure is a monoclinic lattice with lattice constants of $a = 8.091$ Å, $b = 5.565$ Å, $c = 26.264$ Å, and $\beta = 98.17°$. The molecules are stacked in a herring-bone structure where the molecular planes are tilted 66° with respect to each other as indicated in fig. 2.6(c). A shift of electronic charge from the hydrogen atoms to the carbon atoms causes a Coulombic interaction between the molecules. This interaction is expected to be stronger than the van der Waals interaction, which is also present[91]. The Coulomb attraction leads to parallel alignment of the molecular axes and to the formation of layers, each with a width of ~ 26 Å as shown in fig. 2.6(b). Between the vertical segments the interaction is almost entirely due to van der Waals forces and therefore weaker than within the layers. Due to the non-covalent intermolecular interaction this material may be expected to be relatively soft and fragile.

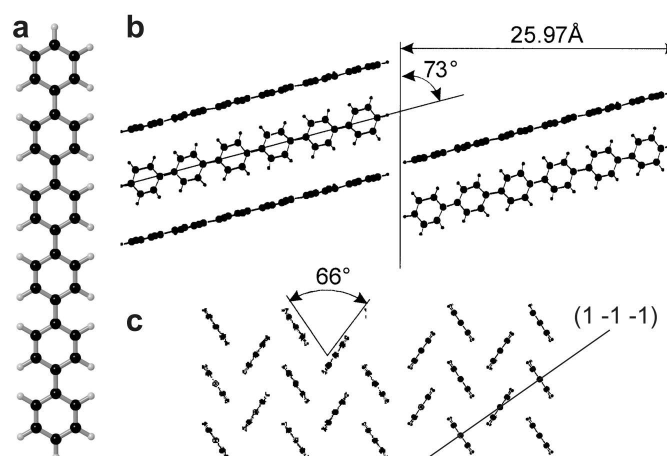

Figure 2.6: (a) Ball and stick model of a p6P molecule. (b) The arrangement of the p6P molecules in the crystal structure in the (1 -1 -1) plane. The molecules form layers of a width of 25.97 Å. (c) The herringbone structure within one layer corresponding to looking at (b) from the right. Reproduced from [91].

A special property of the p6P molecules is that they can form fiberlike crystalline aggregates[4], here termed nanofibers. Fig. 2.7(a) shows a space-fill model of the crystal structure of such a nanofiber, while the TEM image in fig. 2.7(b) indicates the crystalline structure. The fibers have a typical width between 100 and 400 nm, a typical height between 20 and 50 nm, and an as-grown length of typically some hundred μm. The AFM image in fig. 2.7(c) shows a 300 nm wide and 50 nm tall nanofiber along with the cross-sectional profile. Due to tip convolution effects the nanofiber width is slightly overestimated. The fluorescent properties are shown in fig. 2.7(d), where UV light is used to excite the nanofibers.

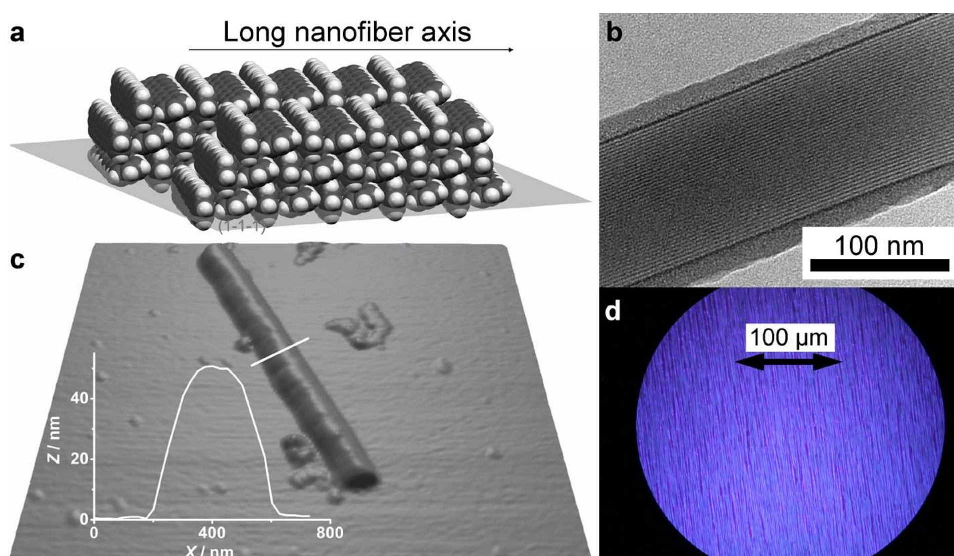

Figure 2.7: (a) Space-fill model of the p6P molecular crystal structure. (b) Transmission electron microscope image of a p6P nanofiber. Courtesy of Annette Thierry, CNRS, Strassbourg. (c) 4.9 μm by 4.9 μm AFM image of a short piece of a p6P nanofiber supported on silicon dioxide. Inset shows the cross-sectional profile measured along the indicated line. (d) Fluorescence microscope image of a growth substrate with many parallel nanofibers.

2.2.2 Electronic Structure

While the strong σ bonds have high binding energies, the energy levels near the Fermi level originate from the molecular orbitals formed by the π electron system. The two most important orbitals are the highest occupied molecular orbital (HOMO) and the lowest unoccupied molecular orbital (LUMO). To a large extent, these two govern the electrical and optical properties of both isolated molecules and the molecular crystal[92].

The electronic structure can be investigated by quantum chemical calculations. For example, the electronic properties of small, isolated, organic molecules can be computed using the Hartree-Fock INDO calculation scheme[93]. Such calculations can provide approximate molecular orbitals (i.e. one-electron wave functions) and their corresponding energy levels. Fig. 2.8(a-b) show the spatial distribution of the HOMO and LUMO, respectively, of the p6P molecule.

In the solid state, the molecules are packed in a crystalline structure as shown above (fig. 2.6). The HOMO is a fully occupied, bonding π-orbital while LUMO is an unoccupied, anti-bonding π^*-orbital. Since the π electron system is thus saturated no intermolecular covalent bonds can form, and the molecular solid is held together only by van der Waals and Coulomb

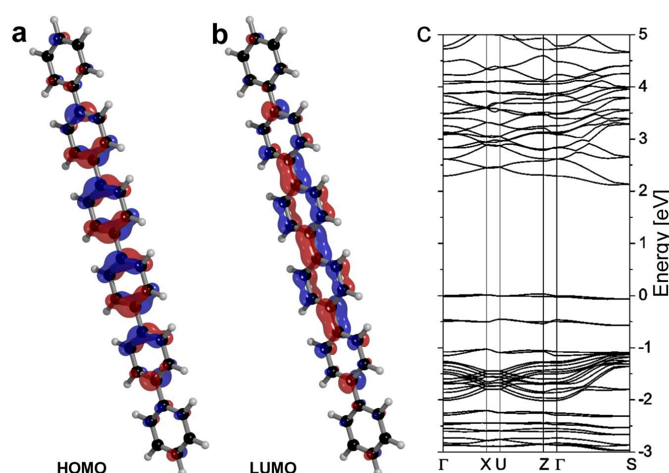

Figure 2.8: (a) HOMO and (b) LUMO of the isolated p6P molecule. The different colors represent the sign of the wave function phase. Courtesy of Henrik Henrichsen, who performed the p6P electronic structure calculations with the *ArgusLab* software. (c) Electronic band structure of p6P along high symmetry directions calculated by density functional theory (DFT). The unoccupied levels have not been adjusted to account for the underestimation of the band gap inherent in DFT (see text). Reproduced from [94].

forces as described earlier. Still, the interaction between adjacent molecules causes the energy levels of the isolated molecules to split up and form energy bands. However, since the overlap of the molecular orbitals between adjacent molecules is small, the splitting is not significant. The electronic structure of the solid is therefore to a large extent determined by the electronic structure of the individual molecules. The electronic band structure of crystalline p6P have been calculated by DFT[94] and is reproduced in fig. 2.8(c). Here, the energy axis is referenced to the position of the HOMO level. This band structure resembles that of a typical inorganic semiconductor where the HOMO levels form a valence band while the conduction band is formed from the LUMO levels although with significantly smaller bandwidths. It should be noted that DFT calculations typically underestimate the band gap, and that the unoccupied bands therefore should be shifted $\sim$ 1.3 eV upwards[94]. A band gap of $\sim$ 3.5 eV is thus predicted from this.

2.2.3 Electrical and Optical Properties

In a simplistic view, the HOMO band supports the conduction of holes, the LUMO band supports the conduction of electrons, and photon generation occurs through the relaxation of an electron-hole pair - analogous to the case of inorganic, covalently bonded semiconductors. However, the situation in

organic semiconductors is more complex. In general, two different transport mechanisms can exist: 1) band-like motion similar to that in inorganic semiconductors, and 2) hopping transport, where localized charge carriers jump between adjacent molecules. Whether the band model or the hopping model applies is determined by the balance between the energy gained by delocalization of a carrier in a carrier band and the energy gained when a molecule relaxes around a carrier to adapt to the excess charge thus forming a self-trapped state i.e. a polaron[95].

In ultrapure single-crystals at low temperature, carrier transport can be described with the band model[96]. In this case, the widths of the valence and conduction bands, formed by the interaction of the HOMO and LUMO levels of the molecules, respectively, determine the hole and electron mobilities. At higher temperatures, electron-phonon scattering increases leading to a high temperature regime where the transport occurs through thermally assisted carrier hopping. This transition occurs well below room temperature[97]. Similarly to the carbon nanotube description, the focus will here be limited to the high temperature case, i.e. the carriers are localized and transport occurs by incoherent hopping.

When a carrier is localized on a molecule in the solid, its energy will be shifted to a lower energy with respect to that of the isolated molecule because of the polarization of the surrounding medium. This polarization energy will include electronic contributions from the electronic charge of both the molecule in question as well as its neighbors, and a vibronic contribution due to the relaxation of the molecular geometry to accommodate for the excess charge[98]. The energy levels associated with charge transport are thus those of electron and hole polarons. The position of these levels can be investigated by photoelectron spectroscopy. Koch *et al.* made such investigations for a p6P thin film and found the LUMO and HOMO levels to be located $\sim$ 2.9 eV and $\sim$ 6.0 eV, respectively, below the vacuum level[99]. These values will be used here, although this system is not completely identical to the nanofiber case since the p6P film is less crystalline[99].

The charge transfer in the localized regime can be expressed as the transfer of one electron (or hole) polaron from a charged molecule to an adjacent, neutral molecule. This can be described theoretically with the Marcus theory, in which the electron transfer rate k_{EF} is given by[100, 101]

$$k_{EF} = \frac{4\pi^2}{h}\frac{1}{\sqrt{4\pi\lambda k_B T}}t^2 \exp(-\frac{\lambda}{4k_B T}), \tag{2.12}$$

where h is Planck's constant, t is the transfer, or overlap, integral, and λ is the reorganization energy. The reorganization energy, which describes the strength of the electron-phonon coupling, is due to the relaxation of the geometries of both molecules involved in the charge transfer. An additional contributing factor stems from the possible polarization/relaxation of the surrounding medium. To a first approximation, the reorganization energy

can be estimated as two times the polaron binding energy[93], which has been found to be 45 meV and 65 meV for the hole and electron polaron in p6P, respectively[102].

The transfer integral t corresponding to a particular molecular orbital can be determined by a number of different theoretical approaches[95]. It is in general proportional to the splitting (bandwidth) of the particular orbital involved in the carrier transport, since a large splitting corresponds to a large interaction between neighboring molecules. In a one-electron picture, t can be estimated as half the splitting of a particular level in a two-molecule system[103] or one fourth the splitting in an infinite 1-D crystal[95].

In general, the transfer rate will be the governing factor of the carrier mobility, however, an exact determination of the mobility requires additional knowledge of the interaction with phonons and the polarization of the surrounding medium[104]. Still, the band structure can provide insight into the transport properties. Examination of the energy bands shown in fig. 2.8(c) reveals different band splittings in different directions. This suggests a higher mobility along a direction perpendicular to than along the long molecular axis[94]. This can also qualitatively be understood from the orbitals in fig. 2.8(a-b). The carrier is primarily located near the center of the molecule, and it therefore has a larger probability of hopping to a molecule within the same layer rather than one in adjacent layers. This is in agreement with experimental findings from ordered p6P films with the molecular axis either parallel or perpendicular to the direction of current flow[105]. For the nanofibers this means that the preferred carrier transport direction will be approximately along the long nanofiber axis.

Also the optical properties of organic semiconductors differ from the inorganic counterparts. When an electron is excited from the HOMO to the LUMO level or when an electron and a hole meet at the same molecule, a Coulomb force will act between the electron and the hole and form an exciton. Due to the Coulomb interaction, the energy of this electron-hole pair is smaller than the difference between the HOMO and LUMO energy levels, and the photon energy emitted when the exciton relaxes is thus also smaller than the band gap. The luminescence spectrum of p6P shows several peaks corresponding to different vibrational levels. Fig. 2.9 shows both the photo- and electroluminescence spectrum of a p6P thin film.

The spectra are dominated by a peak at 425 nm, which is due to a transition from the LUMO vibrational ground state to the first excited vibrational state in the HOMO band (i.e. the (0-1) transition). Also the (0-0) and (0-2) transitions are discernible although less intense. The similarity of the two spectra suggests that the same transitions are responsible for the light emission in both cases. A different study[106] has shown that the nanofiber photoluminescence spectrum shows the same features although with some slight differences: the widths of the individual peaks are smaller and their intensity ratio changes with the (0-1) peak becoming more pronounced.

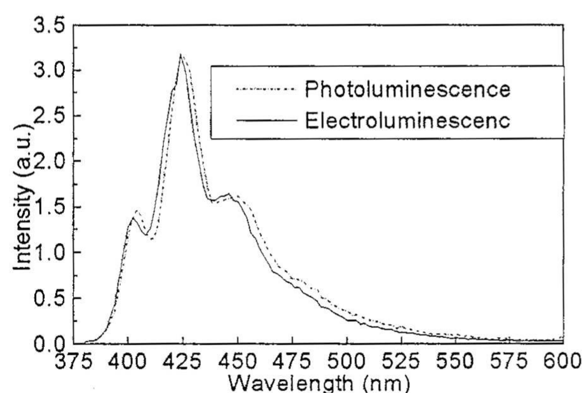

Figure 2.9: Photo- and electroluminescence spectrum of a p6P thin film. The peaks correspond to transitions between different vibrational levels as described in the text. Reproduced from [88].

When the exciton relaxes, the emitted light will be polarized along the direction of the long molecular axis[106] due to the spatial distribution of the orbitals involved in the electronic transition. Since the long molecular axes are all parallel, the emitted light from a nanofiber is highly polarized almost perpendicular to the long nanofiber axis.

2.2.4 Synthesis of Organic Nanofibers

The nanofibers are fabricated via a self-assembly process where the individual molecules align on the surface of the growth substrate through interaction with its surface dipoles[4]. The growth substrate, typically muscovite mica $[K_2Al_4[Si_6Al_2O_{20}](OH)_4]$, is cleaved along the (0001) direction and transferred to the growth chamber. The hetero-epitaxial growth occurs under ultra-high vacuum conditions where the p6P molecules are evaporated towards the mica substrate from a resistively heated Knudsen cell. If the mica substrate is kept at room temperature, a structureless film is formed [107], whereas an elevated substrate temperature of typically ~ 400 K causes the formation of long parallel p6P nanofibers. The surface dipoles polarize the individual molecules, and at elevated temperatures the molecules have sufficient thermal energy to align with the surface dipoles. Similar growth can be obtained with shorter phenylene molecules such as p4P and p5P although the growth direction becomes less well-controlled - presumably due to the decreasing polarizability with decreasing length[107]. The fluorescence microscope image in fig. 2.7(d) shows the mica substrate with the parallel p6P nanofibers after growth. By observing the luminescence under different polarization angles it can be confirmed that the light is polarized approximately perpendicular to the long nanofiber axis.

Chapter 3

Manipulation and Integration

The scope of this chapter is to explore the mechanical manipulation strategy both in terms of investigating mechanical properties of nanostructures and as a method for nanocomponent positioning. This chapter starts with an introduction to the important forces in micro- and nanomanipulation since the behavior of these differ somewhat from what is experienced at the macroscale. This is followed by an introduction to different manipulation systems both for 2-D, AFM based manipulation and for 3-D manipulation, for which an experimental set-up has been constructed. Then, different tools and strategies for 3-D manipulation are described and evaluated, followed by two sections dealing with manipulation experiments on carbon nanotubes and organic nanofibers, respectively. Finally, an experimental method, based on 3-D manipulation, for contacting individual nanocomponents will be detailed.

3.1 Micro- and Nanomanipulation Forces

The word *manipulation* stems from the Latin *manus*: "hand" and has as one of its meanings "To adjust an object by hand". In the present context it therefore means mechanically moving a nanocomponent in a controlled manner either by sliding along a surface (in the case of 2-D manipulation) or by pick-and-place (in the case of 3-D). Manipulation at the micro- and nanoscale differs considerably from the macroscale equivalent due to the scaling of the involved forces. Since the volume of an object scales with the cube of some characteristic length, while the surface area scales with the square, gravity tends to become insignificant for sufficiently small objects. Instead, forces that depend on surface area will become dominating. These include van der Waals (vdW) forces and adhesion forces due to capillary effects and to the interfacial energy between two objects in contact. Most

of these forces are typically attractive. In addition, electrostatic forces and friction forces can also play a significant role for the behavior of nanoscale objects, in particular in relation to manipulation.

This section will give an introduction to the origin of these forces, and approximate quantitative estimates based on a specific example will be made. Typically, manipulation involves the contact between the nanocomponent and a manipulation tool and substrate, respectively. Both types of contact can in a simple picture be modelled as a cylindrical rod (the component) near or in contact with a flat surface (either the tool or the substrate). This will therefore be the example of choice. To be able to provide quantitative estimates, the forces between a 100 nm diameter silicon wire and a glass surface will be considered, since this corresponds approximately to an experimental case considered later in this chapter.

Van der Waals Forces

Van der Waals forces between two objects are due to electromagnetic interactions between the atomic or molecular constituents of the two objects. Typically, the largest contribution to the vdW forces is caused by the instantaneous polarization of one molecule due to charge distribution fluctuations in a nearby molecule which leads to a mutual attraction known as the London dispersion interaction. The vdW interaction energy between two molecules takes the form $E_{vdW}(r) = -C_{vdW}/r^6$, where C_{vdW} is a constant depending on the particular molecules and r is their separation[108]. To a first approximation the total vdW interaction can be found by summing the pairwise interactions between the molecules making up the objects (known as the Hamaker method). In the case of a cylinder with diameter d lying on a planar surface, the vdW forces per unit length, F_{vdW}, take the form[108]

$$F_{vdW} = \frac{A_H\sqrt{d}}{16x^{5/2}}, \tag{3.1}$$

where A_H is the Hamaker constant and x is the separation distance between the cylinder surface and the planar surface. The value of A_H depends on the two interacting materials and the intermediate medium. For interaction between silicon and glass in air, A_H has a value of $\sim 10^{-19}$ J, whereas in water it is around 5 times lower[109]. Assuming a typical Lennard-Jones separation of 0.2 nm[110] gives vdW forces in air of 3.5 μN per μm nanowire. It should be noted that this calculation assumes two smooth surfaces and that surface roughness or any curvature will reduce this value.

Electrostatic Forces

In addition to the dipole forces considered in the previous section, there can be an additional interaction if the objects are electrostatically charged,

leading to a conventional Coulomb interaction. If the object and the tool are electrically conductive it is to some extent possible to control or even use the electrostatic forces by applying appropriate electrostatic potentials. However, if one or both are electrically insulating, this is not possible, and the electrostatic forces are then difficult to predict and thus control[111]. For example, triboelectrification effects can cause charge to build up, which can severely disturb manipulation experiments. Sometimes a scanning electron microscope is used for observation during manipulation. This can lead to additional electrostatic interactions since the electron beam can cause charging effects, especially of surfaces and objects that are not grounded or are poorly conducting.

Capillary Forces

In ambient conditions, a liquid bridge, or meniscus, can form between two objects in close proximity by condensation of humidity from the surroundings. This meniscus will cause an adhesive force between the objects due to a pressure difference across the vapor-liquid interface known as the *Laplace pressure*[112], which is proportional to the surface tension γ_L. This adhesive force is typically the most significant part of the capillary force, which in general, however, contains additional contributions not considered here. Calculating exact values of the capillary force requires a detailed knowledge of the surrounding water vapor pressure as well as surface roughness and wettability properties of both the object and the tool/substrate. This is typically done via numerical calculations and is beyond the scope here, which is to provide an estimate of the relative importance of the involved forces. A simple way of estimating the capillary force relative to the vdW forces is to consider the forces acting between a simple geometry such as a sphere and a plane. A 100 nm diameter sphere separated from a plane by 0.2 nm experiences vdW forces of[108]: $F_{vdW} = A_H d/12x^2 = 21$ nN, where the same Hamaker constant as previously has been used. The capillary force can to a first approximation be found from[112]

$$F_{cap} \approx 2\pi d\gamma_L \cos\theta, \tag{3.2}$$

where θ is the contact angle. A maximum estimate can be found by assuming $\cos\theta = 1$ for a strongly hydrophilic material, which gives a capillary force of 44 nN (a value of $7 \cdot 10^{-2}$ J/m^2 has been used as the surface tension of water[113]). This simple estimate predicts that the vdW forces and the capillary force can be of the same order of magnitude. Since the capillary force is dependent on the experimental surroundings it is necessary to control the ambient conditions for reproducible manipulation for example by always working in a dry environment to reduce the capillary effects, or to use objects with hydrophobic surfaces.

Contact Forces

When two elastic objects come in contact there will be additional adhesive forces that must be overcome to separate the objects. Both objects will experience a deformation, which will generate a contact area that depends on their Young's modules (and on any external forces). Due to the surface energy of the two materials, this generated contact area will cause a lowering of the overall surface energy, which must be overcome in order to separate the objects. This is known as the work of adhesion W and will introduce an additional 'pull-off' force that will depend on the interfacial energy between the two solids[112]. This is typically described within the framework of the JKR theory to provide an estimate of the pull-off force. The pull-off force per length between a cylinder and a plane is[114]

$$F_{\mathrm{pull-off}} = 1.25(KW^2d)^{1/3}, \tag{3.3}$$

where K is the equivalent Young's modulus (equal to $\sim$ 70 GPa for the combination of Si and SiO_2 - see [114] for details) and W is the work of adhesion. Its value is highly dependent on the materials in question. For example the high surface energy of silicon would cause a similar high work of adhesion. However, since a silicon wire must be expected to have a thin native oxide layer, the surface energy and thus work of adhesion will be lower. Assuming a value of W of $3 \cdot 10^2$ mJ/m^2[115] leads to an pull-off force per unit length of nanowire of $\sim$ 10 μN per μm. Again, this is calculated assuming two smooth surfaces in contact. Like with the vdW forces, the surface roughness can lower the resulting pull-off force considerably[108].

Whereas adhesion is of particular importance in 3-D manipulation, where the tool must lift the object off the substrate and release it at the desired position, friction forces play an important role in 2-D manipulation. The friction is classically proportional to the normal force F_n, which will have contributions from some of the aforementioned forces. The macroscopic friction force F_f can be quantified by means of the friction coefficient μ

$$F_f = \mu \cdot F_n, \tag{3.4}$$

where the friction coefficient typically lies in the range between 0.1 and 1. The situation is somewhat different at the nanoscale, where friction has been demonstrated to scale with contact area[116].

3.2 Manipulation Systems

Micro- and nanomanipulation can be divided into two categories: 2-D and 3-D. In 2-D manipulation, the object is constantly supported on a substrate and is moved controllably by the application of a lateral force. In

contrast, 3-D manipulation involves releasing the object from its initial position, transferring it to the target substrate, and releasing it here. The primary applications of the two also differ. Where 2-D manipulation is typically used for exploring fundamental, intrinsic properties of nanostructures and their interaction with each other or the supporting substrate, 3-D manipulation typically has a more technology-oriented scope. It is most relevant as a method of handling nanostructures/components in order to facilitate pick-and-place operations to fabricate prototype devices[12].

To manipulate an object requires overcoming the forces that pin it to its present position. In the 2-D case, this involves applying a force larger than the static friction force. In 3-D manipulation, the object must first be lifted off the initial substrate, i.e. the tool must apply a force larger than the adhesive forces. Then the object must be placed at a target substrate by achieving the opposite force balance: that the adhesive forces towards the target substrate are increased above the force keeping the object on the tool. The increased complexity of 3-D over 2-D manipulation has meant that whereas 2-D manipulation has been demonstrated even with single atoms[117], 3-D manipulation experiments have only been demonstrated with somewhat larger objects such as MWCNTs (with diameters of a few tens of nm and micron lengths) depending on the type of manipulation system. This section will introduce different manipulation systems with particular emphasis on the two systems used here: an AFM based, 2-D system for investigating nanocomponent properties and a 3-D system, based on an optical microscope and xyz translators, for prototype device fabrication by pick-and-place operations.

3.2.1 2-D Manipulation Systems

Manipulation along a surface is typically carried out using the tip of a scanning probe microscope (SPM) as the tool. The high resolution achievable with a scanning tunnelling microscope (STM) has made this instrument the favored choice for manipulation at the scale of single atoms and molecules[118]. The use of an AFM based system enables monitoring of the forces during manipulation, which can provide valuable information both about the mechanical properties of the object as well as its interaction with the substrate. Although the main application of 2-D manipulation is for exploring fundamental properties, it has also been used for more technology-related aspects such as the accurate positioning of an individual MWCNT between two prefabricated electrodes[11]. 2-D manipulation often uses the same probe for imaging and manipulation. This is a significant drawback of 2-D manipulation as an efficient manipulation method for constructing prototype devices since this tends to make 2-D manipulation comparably slower than 3-D manipulation, which typically employs separate imaging and manipulation systems.

The focus here is on AFM based manipulation systems in order to probe mechanical properties of nanostructures/components. Several AFMs with built-in nanomanipulation capabilities are commercially available. Typically, they rely on a similar principle of using the probe tip for imaging and manipulation in separate, successive steps, where the tip during manipulation is used as a tool to laterally push the object.

2-D Manipulation Set-up

In this project, a special nanomanipulation system[1] [119], developed by the Nanoscale Science Research Group at the University of North Carolina, has been used. On top of the aforementioned capabilities, this system includes an advanced visual interface and a haptic device (a force-feedback joystick with 6 degrees of freedom) that allows the force experienced by the AFM tip before and during manipulation to be routed back to the operator thus providing a sense of 'feel' of the nanocomponent. Fig. 3.1 shows a block diagram of the nanomanipulator system.

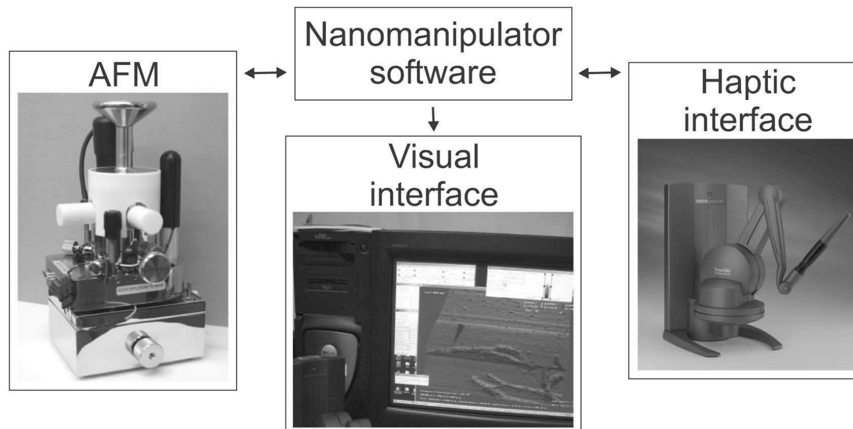

Figure 3.1: Block diagram of the nanomanipulator system.

This system features different ways of performing manipulation ranging from a manual method where the position of the tip during manipulation is controlled directly by the motion of the haptic device to more automated procedures where the tip follows a predefined trajectory. Typically, a medium soft cantilever with a spring constant of ~ 1.5 N/m is used for imaging in tapping mode and manipulating in contact mode. A typical experiment involves first using the AFM to image a substrate with dispersed nanostructures to locate a suitable one. Then, the AFM is switched to an intermediate 'touch mode', where the microscope still operates in tapping

[1] http://www.nanomanipulator.org/

mode, but where the xy position of the tip is controlled directly through the haptic device which allows the user to 'feel' the sample topography. In this way the trajectory, to be followed by the tip during the subsequent automated procedure, can be marked very accurately with the haptic device, and the drift that might have occurred can be taken into consideration since the exact position of the nanostructure can be felt. The AFM is then switched to contact mode with some predefined contact force set-point and the tip performs a lateral movement. During this movement the tip trajectory and lateral forces are recorded simultaneously. In the following, the AFM is switched back to tapping mode imaging to visualize the result of the pushing cycle. Also, it is possible to perform manipulation experiments in a 'direct z' mode, where the tip is not brought into contact mode (i.e. the feedback circuit in not engaged) but where tip position is controlled directly. This is for example used for manipulation of suspended structures. After the initial imaging in tapping mode and the intermediate 'touch mode', the AFM is switched to the 'direct z' mode where the tip can then by used to deflect the suspended structure laterally or vertically.

3.2.2 3-D Manipulation Systems

3-D manipulation systems consisting of a microscope with integrated manipulation tools are most often custom-built systems as no complete systems are commercially available. Examining the prerequisites for 3-D nanomanipulation can be done in a macroscopic view by considering a seemingly trivial task such as picking up a pencil and placing it somewhere else. This requires: 1) the ability to approach the tool (our hand) to the object (the pencil), 2) the ability - aided by the tool - to apply a large enough force to overcome the force that keeps the object at its present position (gravity), 3) the ability to release the object at the desired position, and 4) a feedback system (our vision) to enable the constant monitoring of the procedure thus coordinating the efforts of all the mechanical actuators involved. To be able to do this at a much smaller scale therefore requires a complete system including some type of microscope for monitoring the procedure, a suitable miniaturized tool for applying the necessary force to the object, and a mechanical system both for the coarse approach of the tool to the object and for the delicate movement required for picking and placing. This section will deal in particular with the microscope and the mechanical motion system, whereas the tools will be investigated in the subsequent section.

Two different types of microscopes are frequently used for 3-D manipulation systems: an optical microscope or a scanning electron microscope (SEM). The SEM has the advantage of providing a considerably higher resolution than the optical microscope. However, the increased resolution comes at the expense of significantly more troublesome handling both of the sample and the instruments. A robot, capable of moving the tool into position and

of performing the delicate motion necessary for picking up the object, must be placed inside the SEM vacuum chamber with all necessary connections taken to the outside. The actual tool-to-object coarse approach is also somewhat problematic due to the difficulties of monitoring two objects initially separated a sizeable distance in a SEM. In contrast, most of these difficulties are dramatically reduced with an optical microscope, where the manipulation can be performed under ambient conditions. The most constraining factor here is the limited achievable resolution. A third microscope type has also been used in manipulation experiments. The very high resolution achievable with a transmission electron microscope (TEM) has enabled some remarkable studies of for example telescoping behavior in MWCNTs[120], thus demonstrating the power of a TEM in relation to nanomanipulation experiments by visualizing the microscopic details of the interior of an object during manipulation and of how a tool and an object interact. Similar to the SPMs, the strength of TEM based manipulation lies mostly within studying more fundamental properties, whereas the limited work space within a TEM holder significantly limits the possibilities in terms of pick-and-place manipulation operations with any technological perspective.

As a part of this project, an optical microscope based manipulation system has been constructed in order to investigate the value of such a system for nanocomponent device assembly and to facilitate fabrication of a significant number of prototype devices for further investigation of different nanocomponents. Much research has focused on particular aspects of manipulation such as for example the tool[121, 122], however, it has often concentrated on developing and characterizing the tool or making a few proof-of-principle demonstrations of manipulation. Here a different, system-oriented point of view has been taken. Focus has been on creating an efficient manipulation set-up that not only allows proof-of-principle after many hours of tedious attempts but which can actually be used to assemble prototype devices in a relatively fast and efficient manner.

Construction of 3-D Manipulation Set-up

The experimental set-up consists of an optical microscope and two mechanical stages for sample and tool movement. The optical system is based on a Mitutoyo 50x objective with a long working distance of 13 mm, which eases sample handling and manipulation. Used in combination with a Navitar UltraZoom lens system it offers between 35 and 229 times magnification corresponding to view fields between 188 μm by 141 μm and 29 μm by 17 μm with the attached 1/2" camera that is connected to a computer for image display and still or live image storage.

The sample is mounted on a three-axis manually operated stage, which allows the sample position to be adjusted to fit in the microscope view field. For tool motion, a mechanical motion system is constructed from a Burleigh

PCS-5400 manipulator system, which consists of 3 linear, piezoelectric actuators, each with a resolution of roughly 30 nm and a travel distance of 300 μm. Each piezoelectric actuator is mounted on a linear motion stage based on a manual micrometer screw with a travel distance of several mm for the coarse approach of the tool. This entire actuator system is equipped with an arm carrying the tool, and is mounted on a rotational stage, which allows the arm to swing out for easy tool change. The system is shown in fig. 3.2.

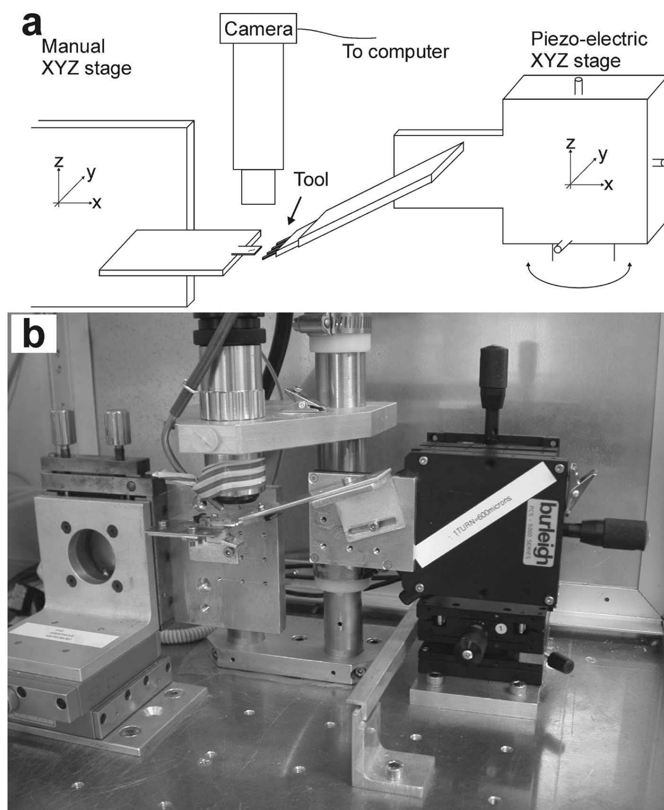

Figure 3.2: (a) Schematic drawing of the optical manipulation set-up. (b) Photograph of the manipulation set-up

The piezoelectric actuators can be controlled by a standard Burleigh controller, where the xyz position is set through 0-60 V voltages via three multi-turn potentiometers. For easier tool positioning, an alternative control system was developed in collaboration with Russell Taylor from the University of North Carolina. This system is based on the Virtual Reality Peripheral Network[2], which is a C++ based set of classes designed to implement an interface between an input device (such as a standard PC

[2] http://www.vrpn.org/

joystick or a more advanced, haptic device) and an output device capable of performing the required motion. The VRPN@MIC system consists of a set of VRPN output servers running on a PC with two National Instruments PCI-6036E DAQ cards, which together provide four 16-bit D/A converters, three of which are used for controlling the x, y, and z axes of the actuator, respectively, while the fourth converter provides an additional channel for the possible actuation of the manipulation tool, such as the closing and opening of a microgripper[123]. The D/A converter outputs are fed to an amplifier with 4 customized channels that recondition the signals to the appropriate levels for the piezoelectric actuators and manipulation tool, respectively. In addition, an input server, running on either the same PC or alternatively on a remote system, reads data from an input device, which here is a standard Logitech PC joystick. Through the VPRN input server, the joystick controls can be adapted to the specific task at hand. Typically, the joystick motion is translated into xy coordinates, while the z coordinate is set by the joystick throttle handle. Finally, two different joystick buttons are used for tool actuation tasks, for example for *gripper close* and *gripper open*. After having read the joystick commands, the input server sends all four channels to the output server, which updates its output channels at an appropriate rate. The VRPN system has the additional option of providing bi-directional communication between the servers. If a force-feedback signal could be produced, for instance from a microgripper[124], this could be routed back to the joystick and provide a sense of how much force is applied to the object by the tool.

Some additional features were built into this set-up, however, they were not used in the experiments presented in this work. A possible use of the system is for electrical four-point measurements of nanostructures[125]. A sample cooling system, which can be mounted on the manual translation stage, was also constructed to facilitate such measurements at lower temperatures. The sample is placed on top of a metallic compartment, through which liquid nitrogen is passed. A second use of the set-up is for characterization of microfabricated grippers[126]. This characterization system, initially developed by Peter Bøggild, consists of a LabVIEW program that controls the voltage applied to the gripper, while the actual gripper actuation is recorded by live processing of the microscope image data.

3.3 Components and Tools

In SPM based manipulation, the imaging probe is also the manipulation tool. The probe tip interacts with the substrate and object during imaging and by increasing the interaction, the tip can apply a lateral force and push or drag the object sideways. The tool is therefore an integrated part of the system which limits the flexibility and number of possible tools. In 3-

D manipulation, more tools and manipulation strategies are available since the tool and imaging system are much more independent. The choice of manipulation tool can be adapted to which components are to be handled. This section will discuss different tools and their performance, evaluated on the basis of different manipulation scenarios.

3.3.1 Component Considerations

When evaluating if a particular component is suitable for manipulation, different aspects should be considered. An important point is component size. Firstly, it must be visible in the type of microscope in question. If its diameter is in the 10 to 20 nm range or smaller, optical microscopy[3] is less useful and SEM is preferable. Also, tool selection is influenced by component size, as too bulky a tool will render manipulation difficult.

A second important aspect is the fragility of the component. There will for example be a mechanical load during manipulation that can damage or even destroy fragile structures. Also the sensitivity against other types of load such as electric fields or high temperatures should be considered as some tools can cause such loads[126].

The initial arrangement of the components is also of significant relevance. Whether the components are available in the form of a liquid dispersion, a powder, or standing/lying separately on a substrate will influence the choice of tool and manipulation strategy. The manipulation substrate should also be considered: the adhesion of the components to the substrate will have a considerable influence on the success rate of picking up. This can in some cases require the use of a special substrate with low adhesion.

A final important issue is the component surface properties. Whereas some structures are inert and retain their surface properties under ambient conditions, others react for example by forming a native oxide layer. This would require either a controlled atmosphere or vacuum during manipulation or additional processing after manipulation to remove such a layer.

3.3.2 Tool Selection

Attention should be given to finding an appropriate manipulation tool. The important requirement put on the tool - apart from the end-effector(s) having a size comparable to the object - is that it must be able to apply a sufficiently large force to the object to lift it off the sample substrate. In addition, for pick-and-place operations it must also be possible to release the object at the target substrate. The applicability of a specific tool is much dependent on the properties of the particular type of components and

[3]An object smaller than the diffraction limit still scatters light and is visible but its size and details cannot be resolved, e.g. if there are two nanocomponents.

their arrangement. In order to make a foundation for a proper tool selection, different types of tools will be evaluated on the basis of some generic component sample geometries.

As described previously, the forces acting at the micro- and nanoscale are primarily attractive surface forces. Microscopic manipulation tools often rely on this and can therefore have rather different operating principles and shapes than macroscopic tools. Here, three different types of tools are considered, all of which have been used in this work: 1) a sharp needle fabricated by electrochemical etching of a piece of tungsten wire, similar to the method used for fabricating STM tips. Two types of more advanced tools have been fabricated by microfabrication methods and tested: 2) a cantilever-based tool with one or several static glass microcantilevers, and 3) microgrippers with two arms that can be actuated by either thermal or electrostatic actuation or some combination[126]. Conceptual drawings of these three types of tools are shown in fig. 3.3

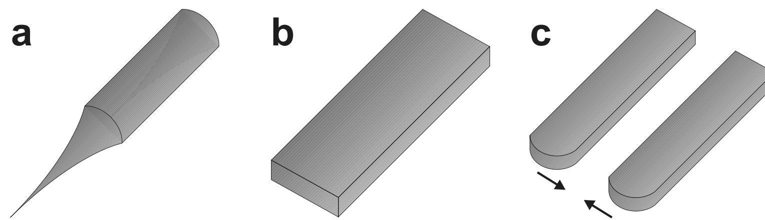

Figure 3.3: (a) Manipulation tool 1: An etched tungsten wire. (b) Manipulation tool 2: A simple glass cantilever. (c) Manipulation tool 3: A microgripper.

Other manipulation tools have been proposed such as the different types of grippers discussed by [124]. In the following, the operating principles of the tools used in this work are described.

1 Etched tungsten wire The use of an etched tungsten wire as the manipulation tool relies on exploiting the adhesive forces between the tool and the object to pick up the object from the sample substrate and stabilize it on the tool. The tool must therefore be approached to the object in such a manner that the applied force is increased up to a level where it exceeds the force that keeps the object in its initial position. This can be done either by manoeuvering the tool into a position where the contact area with the object is maximized for increased adhesion and then drag out the object, or by pushing/lifting the object off the substrate using contact forces (if the sample geometry allows). The release requires the object to be brought to the target substrate and that the adhesive force towards the target substrate is increased above the force towards the tool.

2 **Glass cantilever** The static glass cantilever tool works in a similar manner to the tungsten wire tool. The main difference is the shape. Its planar surface can allow a larger contact area to a cylindrical object thus providing larger adhesive forces. However, it is somewhat more bulky than the sharp tungsten tip, which can be a hindrance with some sample and substrate geometries and sizes.

3 **Microgripper** The microgripper has a considerably different working principle, which more resembles that of a macroscale gripper. It relies on actively applying a gripping force that due to friction will enable the object to be picked up from the surface - in combination with the always present adhesion. Still, this method also relies on using the adhesive surface forces for placing/releasing the object, since opening the gripper will not cause the object to be released. Therefore, the object must be placed in contact with the target substrate for successful placement, and in some cases gluing or soldering must be applied[127].

One advantage of the etched wire tool is its ease of fabrication. It only requires a piece of tungsten wire and a fairly simple set-up for electrochemical etching. In addition, it is possible to fabricate a very sharp tip, which can be advantageous for some applications. However, a sharp tungsten tip deforms plastically at even small impacts, which are unavoidable in a practical manipulation situation where the tool will come in contact with the substrate. This will wear down the wire tip rather fast. Also, it can be problematic to realize a large contact area and thereby a large adhesion force between a conically shaped tip and a cylindrical component. Both the simple cantilever and the microgripper suffer from a relatively complex and time consuming microfabrication process, although, since typically several hundred tools will be fabricated per batch, the fabrication processes will yield enough tools for a large number of manipulation sequences. The planarity of the cantilever makes it easier to obtain a significant contact area with a cylindrical component than when using a conical wire tip. Also, a glass cantilever is (semi-)transparent, which makes it possible to use both sides for manipulation since it will not block the field of view. Finally, the flexible nature of a glass cantilever enables it to bend elastically, which can help in particular in the placement procedure, where the object for instance can be pressed down towards the target substrate and rolled off. The flexibility of the cantilever also makes it comparably more durable since it will not deform plastically at moderate impacts. The gripper tool has the significant advantage of providing an additional gripping force that can aid in picking up objects, which is some cases adhere strongly to the surface[110]. However, in the case of randomly dispersed components, the advantage gained from this additional gripping force does not outweigh the significantly more complicated tool handling that involves actuating the gripper arms. Also, the release from the gripper can limited compared to the cantilever. With

the cantilever, it is possible to rotate the component on the tool by pushing it against a hard surface, before it is released. This is not possible with the gripper, which can only release the component with the same orientation as when it was picked up.

Depending on how the sample is prepared, the components can be located on the sample substrate in a number of different ways. In order to evaluate the three types of tools, some typical sample geometries are considered as shown in fig. 3.4.

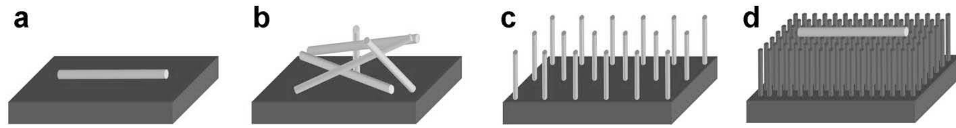

Figure 3.4: Conceptual drawings of different component sample geometries. (a) The component is lying flat on the sample substrate. (b) The components are positioned randomly in a 'haystack' geometry. (c) The components are standing vertically up from the sample substrate in a predefined pattern. (d) The component is supported by a number of vertical columns.

A typical way of preparing a sample is to have the components dispersed in a liquid, apply a small volume of the dispersion to a planar surface, and let the liquid evaporate. This would typically leave the components lying flat on the sample surface as shown in fig. 3.4(a). A second possibility is to have the components entangled in one another as shown in fig. 3.4(b). This could for example be the case for carbon nanotubes in powder form. A particular case, considered in the next section, is silicon wires made by anodic etching[128]. These straight, rigid wires can also form a sample geometry very similar to fig. 3.4(b). In some cases, it can be useful or even necessary to prepare a component substrate specifically suited for manipulation. One possibility is a component substrate prepared in such a way that the components are free-standing vertical structures as shown in fig. 3.4(c). Such a geometry can for instance be made by growing carbon nanotubes or III-V nanowires from an array of pre-patterned catalyst particles[76]. As a final geometry, one can prepare a substrate with a high density of vertical columns[129] as shown in fig. 3.4(d). Here, the components can dispersed in a similar way as in (a) to yield a significantly reduced effective contact area. This particular type of substrate is especially useful for manipulation of fragile components such as organic nanofibers and will be described in more detail in a later section.

In the simple sample geometry in fig. 3.4(a) there is a significant contact area between the component and the substrate. As in the example considered in section 3.1, this can be modelled as a cylinder on a planar surface. Assuming similar cross sectional dimensions, a length of 10 μm, and that the primary contributions originate from the van der Waals forces and the

pull-off forces, the adhesive force is estimated to of the order of $1 \cdot 10^2$ μN. Picking up in such a geometry is inherently difficult. Simply touching the upper side of the component with the tool will not create sufficient adhesion to the tool since the tool-component contact area will be smaller than the substrate-component contact area. A second option, as recently discussed by Mølhave and co-workers[110], is to use a microgripper to apply a larger force. However, the required force in this case is quite high compared to what has been realized with microgrippers[110, 124]. In addition, gripping is significantly hindered by the difficulty in achieving a gripper with very sharp end-effectors necessary to grip a flat-lying component. A possible route could be to coat the substrate with a low-adhesion coating prior to dispersing the components as described in section 3.5.1. In some cases, a teflon-like coating can even cause a repulsive vdW interaction[130]. This could enable strategies relying only on the adhesive forces between the tool and the component, and cantilever could then be used to pick up by simply touching the component.

The entangled components in fig. 3.4(b) have a significantly smaller contact area with their surroundings and should therefore by easier to pick up. Providing a force estimate is difficult since this is very dependent on the particular sample as well as the shape, size, and mechanical properties of the components: rigid, straight Si wires can form a sample geometry quite similar to fig. 3.4(b) (as also seen in fig. 3.5(a)), whereas carbon nanotubes in a powder form can be curled up and entangled in one another. Different tools can be used in this case. One option is to use the simple etched wire or cantilever to touch and pull out a component using only the adhesive forces. Here, the planar surface of the cantilever eases the task, since this can form a larger contact area with a cylindrical object than a conical wire tip can. Another option is to use the gripper to provide a larger force than just the adhesion. However, the usefulness of the additional gripping force is limited with this sample geometry, and the extra circuitry and wiring needed for gripper actuation only makes the manipulation more complex. This makes the more simple cantilever tool the favored choice here.

The third geometry shown in fig. 3.4(c) requires a sample preparation method capable of producing the vertical, well-spaced components. In this case, a force large enough to break the component off the substrate must be applied, the magnitude of which will depend on the mechanical properties of the particular component and the binding to the substrate. Here, the gripper is much better suited than the simpler tip and cantilever tools. In particular, the ability of the gripper to apply a shear force is important in this scenario[110]. This particular geometry is of interest due to the more well-defined position and direction of each component, which would be necessary if an automated manipulation procedure was to be established.

The final geometry shown of fig. 3.4(d) resembles the first with the main difference that the contact area between the substrate and the component is

significantly smaller. Also, as is demonstrated in section 3.5.2, if the vertical posts supporting the component are mechanically compliant and can bend, it is possible to make the tool penetrate in to the 'forest' and go below the component to lift it up from below. In this geometry, the sharp wire tip is well-suited, whereas the more blunt cantilever and gripper are of less use.

3.3.3 3-D Manipulation Example

The requirements for the tool are thus seen to depend on the particular component sample, and the choice of tool must therefore be made on a case-by-case basis. As an example of particular manipulation task, fig. 3.5 shows a silicon wire 'haystack' from which a single wire should be picked up and placed on the target structure: an elevated silicon dioxide platform. This task is of particular interest in relation to a shadow mask method for fabricating electrodes on nanocomponents as described in the end of this chapter.

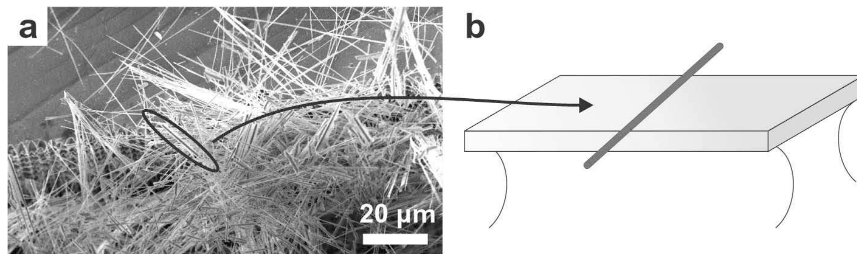

Figure 3.5: (a) SEM image of silicon wire 'haystack'. The wires typically have a diameter between 200 and 1000 nm. The manipulation task consists of picking up an individual wire from the 'haystack' and positioning it on top of an elevated silicon dioxide structure as illustrated in (b).

This task is most easily accomplished with a cantilever tool. Since the wires are not adhering strongly to the substrate, it is sufficient to bring in a planar tool and make a comparably larger contact area with the desired wire. This will cause the wire to adhere to the tool and it can be picked up. Release can be accomplished by bringing the wire to the target structure and placing it in a position with an even larger contact area. Fig. 3.6 shows a tool consisting of 4 glass cantilevers being used to first pick up a silicon wire, then transfer it to the target structure, and finally release it.

Apart from pick-and-place operations, a second useful function is to be able to fasten the object at the target structure. This can for example be done by dissociating organometallic gas molecules with a focused electron beam to form conductive deposits, which has been used to solder nanotubes to microelectrodes[127]. Whereas such soldering requires a SEM, a 'gluing' method has been developed here, which can be performed in the optical

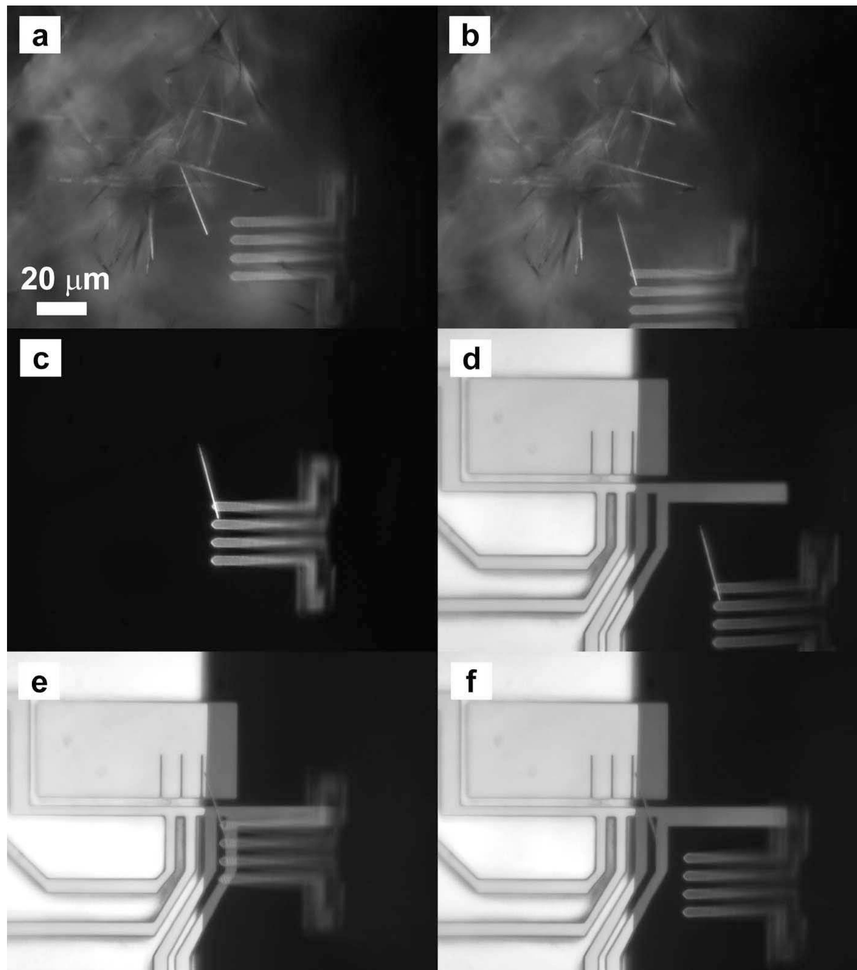

Figure 3.6: (a) The cantilever manipulation tool is approached to the silicon wire 'haystack', and (b) is positioned such that a significant part of the desired silicon wire touches the tool topside. Moving the tool southwards draws out the silicon wire, which can then be transferred (c). (d) The silicon wire is approached to the target structure, where it is placed at the desired position by maximizing its contact area with the target structure (e). (f) Lifting the tool leaves the silicon wire at the desired position.

manipulation set-up. This method relies on using small polystyrene (latex) beads as glue. It exploits the ability of electrothermal grippers[124] to heat objects locally to melt a latex bead, which has been transported to the desired position. This is demonstrated in fig. 3.7 where a silicon wire is glued to a microcantilever. First, the silicon wire is placed on the cantilever as described previously. A 5 μm diameter latex bead is then picked up

with the electrothermal gripper using only adhesive forces (i.e. without heating the gripper). The latex bead is then transported to the silicon wire resting on the microcantilever (fig. 3.7(b)). A brief heating of the gripper by the application of current of a few mA is used to melt the latex bead and deposit the material at the base of the wire as seen in fig. 3.7(c). Fig. 3.7(d) demonstrates that the deposited material fix the wire to the cantilever as lateral pushing does not release the wire.

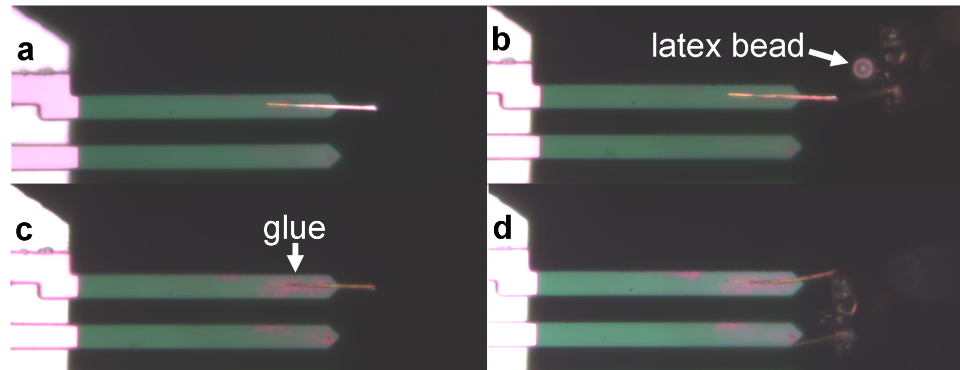

Figure 3.7: Latex bead gluing. (a) A silicon wire placed on a microcantilever extending from its tip. (b) A latex bead is transferred to the cantilever and while the bead is held directly above the base of the silicon wire the latex bead is melted by heating the gripper. (c) The melted latex bead is deposited on the cantilever and silicon wire. (d) The gripper is used to displace the silicon wire tip, while its base is seen to remain fixed to the cantilever.

3.4 Manipulation of Carbon Nanotubes

Several AFM based nanomanipulation studies have focused on exploring mechanical properties of carbon nanotubes and on their interaction with a substrate. 3-D manipulation has also been reported such as the attachment of a MWCNT to an AFM probe tip[131]. Although 2-D manipulation of CNTs was not performed in this project, a brief summary will be given for the sake of comparison with the organic nanofibers, followed by a description of the 3-D manipulation experiments performed here.

3.4.1 2-D Manipulation of Carbon Nanotubes

The AFM based nanomanipulation system introduced earlier has been used by Falvo *et al.* to investigate the mechanical properties of MWCNTs[132] and their interaction with an underlying mica or graphite substrate[133]. The bending of MWCNTs under large strain was investigated on mica, where

the tube/substrate friction can be sufficiently large to pin the tube in the bent configuration. These studies showed that it is possible to induce a very high, local strain of up to $\sim 16\ \%$ without rupture. Supported MWCNTs can also slide in response to lateral pushing in cases where the tube-substrate friction is not sufficient to pin the tube. Based on quantitative lateral force data the sliding shear force was estimated at $2 \cdot 10^6$ Pa. On graphite, however, a rolling behavior was observed in certain cases with a friction suddenly much higher. This occurs when a particular threefold, in-plane orientation on the nanotube was obtained, which was suggested to be due to lattice registry with the graphite substrate caused by their geometric similarities as discussed in section 2.1.1, thus preventing sliding. Similar techniques were used by Lieber and co-workers to deflect a MWCNT, which was pinned in one end, to determine its elastic properties yielding a Young's modulus of ~ 1.3 TPa[134]. By rupturing suspended SWCNT ropes, a yield strength of ~ 45 GPa was found by the Smalley group[135].

3.4.2 3-D Manipulation of Carbon Nanotubes

As shown in fig. 3.6, 3-D manipulation of silicon wires can be accomplished fairly easily with the constructed set-up. This manipulation technique has been extended beyond the silicon wires to include manipulation of a variety of nanocomponents including MWCNTs to facilitate precise positioning in a microsystem. Here, the high mechanical strength of MWCNT makes these very robust, which eases manipulation significantly. Different MWCNT samples have been investigated including both CVD grown and arc-discharge fabricated MWCNTs. The nanotubes were all available in the form of a powder from which the sample was prepared by simply dispersing MWCNT grains on a piece of adhesive tape. This would generate a sample geometry somewhat similar to fig. 3.4(b) (although with the nanotubes being more entangled). All three types of tools were tested with this type of sample. Here, the cantilever turned out to be the best suited tool. In some cases a nanotube would adhere only slightly to the substrate and could be picked up simply by touching it with the cantilever and pulling it out. In other cases, it would adhere more strongly and it would be necessary to try to pull in different directions to release it. Finally, some nanotubes adhered too much to be released and had to be abandoned. The microgripper was also used with some success. However, the increased complexity involved in actuating the gripper did not significantly ease the process of picking up MWCNTs in this sample geometry since neither the sample nor the tool can be rotated with the present set-up for optimal tool-component alignment. Fig. 3.8(a) shows a microscope image recorded in the manipulation set-up of a cantilever tool approaching a MWCNT. The smaller size of the nanotube compared to the silicon wires in fig. 3.6 causes a more blurred appearance, however, observation and manipulation is nonetheless possible.

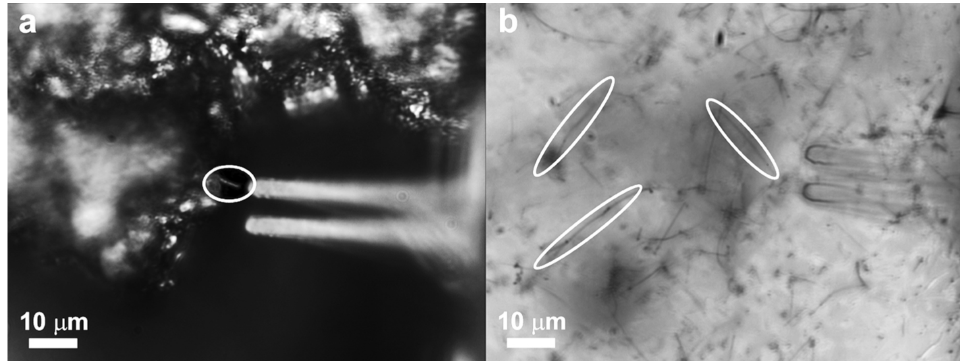

Figure 3.8: The static cantilever tool used for picking up (a) a single MWCNT produced by the arc-discharge method and (b) a single indium phosphide nanowire produced by the laser-assisted vapor-liquid-solid method.

In addition to MWCNT manipulation, a variety of other nanocomponents have been tested to verify that this set-up can be used also with other nanocomponent types and geometries. These include indium phosphide nanowires grown by the laser-assisted vapor-liquid-solid method[136] as shown in fig. 3.8(b) and indium arsenide nanowires grown by an oxide-assisted metalorganic vapor phase epitaxy method[137]. Also in this case, such nanowires can be picked up by touching the nanowire with the tool and gently pull it off the substrate. Also bismuth nanowires produced by electrodeposition in etched ion-track membranes[138] were manipulated. Here the size-defining membrane was first dissolved and the nanowires dispersed on a substrate, from which they were subsequently picked up and positioned on the target structure. Also in these cases the simple static cantilever tool turned out to perform best. Finally, attempts were made to pick up a p6P nanofiber from a planar substrate. In these initial attempts, the fragility of the nanofibers would cause these to break during manipulation. A special manipulation substrate, similar to that in fig. 3.4(d), later enabled such manipulation as described in section 3.5.2.

3.5 Manipulation of Organic Nanofibers

Due to the weak intermolecular interaction, p6P nanofibers are rather soft and fragile. This will impede manipulation significantly in comparison with more robust structures such as carbon nanotubes. The preliminary manipulation experiments with p6P nanofibers supported on a silicon dioxide substrate showed that the nanofibers would break easily when the manipulation tool was brought into contact with these. To study this in more detail,

the mechanical properties of individual p6P nanofibers were investigated by 2-D manipulation experiments using the nanomanipulation equipment described in section 3.2.1. This section will present the results of these studies, followed by a description of 3-D pick-and-place experiments enabled by a special nanotube-coated manipulation substrate.

3.5.1 2-D Manipulation of Organic Nanofibers

AFM based manipulation experiments were performed on p6P nanofibers either supported by a planar substrate or suspended between two supporting structures. The experiments on supported nanofibers were made on substrates with different hydrophobic properties. On silicon dioxide the nanofibers adhere strongly and tend to rupture during manipulation. This system was used to investigate rupture properties of the fibers. By coating a silicon substrate with (tridecafluoro-1,1,2,2-tetrahydrooctyl)trichlorosilane a hydrophobic surface with a contact of angle 104° was obtained. On this low-adhesive surface, the friction was significantly lower and it was possible to slide pieces of nanofibers along the surface. Rupture experiments, similar to those on supported nanofibers, were also performed on suspended nanofibers, and finally, the elastic properties were probed by deflecting a suspended nanofiber. In these experiments, the nanofibers were transferred by drop-casting a small amount of water with dispersed nanofibers onto the desired substrate, which was then left to dry.

Intrinsic Mechanical Properties

The rupture properties of individual nanofibers were investigated by slicing through these with an AFM tip. Fig. 3.9 depicts the starting point and result of two subsequent pushing cycles on a nanofiber on silicon dioxide. As evident from fig. 3.9(b) the pushing caused rupture of the nanofiber, which was a general trend observed when laterally pushing nanofibers supported on silicon dioxide except in the case of very short nanofiber pieces (< 0.5 μm). The lateral force data in fig. 3.9(c) exhibit a sudden increase in lateral pushing force of approximately 0.5 μN at the position where the tip first touches the nanofiber, followed by a decline of the lateral force almost back to zero. The similarity of the two data sets indicates the homogeneity of the nanofiber along its axis. A blind tip reconstruction method[139] allows an estimation of the effective tip radius which can be used for deconvolution of the image data. This gives an actual nanofiber width of $\sim$ 220 nm.

The lateral force data for the two pushing cycles shown in fig. 3.9(c) have peak values of $\sim$ 440 nN (I) and $\sim$ 510 nN (II), respectively. The peak value must correspond to the sum of the force necessary to rupture the nanofiber and the static friction force, which must be overcome in order to begin sliding a small section of the nanofiber along with the tip. The dy-

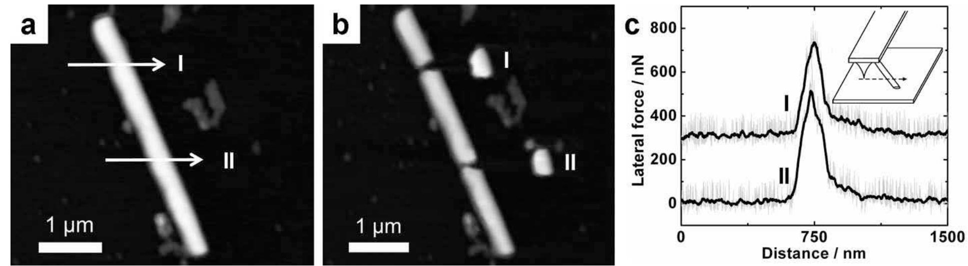

Figure 3.9: (a) AFM image of a 50 nm tall p6P nanofiber on a silicon dioxide substrate before manipulation. The arrows indicate the trajectories of the AFM tip during manipulation. (b) Same nanofiber after two subsequent manipulations along the arrows shown in (a). Note the pieces, which have been cut out. (c) The grey and black curves display the measured and averaged lateral forces, respectively, for positions (I) and (II). Curve I has been shifted for clarity. The normal force during the pushing cycles was 150 nN. The inset shows a schematic drawing of the AFM tip in contact mode being used to manipulate a nanofiber. The force values have been obtained by a calibration procedure that uses measured values of cantilever and tip dimensions, which gives an estimated uncertainty of 30 %[133].

namic friction can be estimated by comparing the value of the lateral forces before and after the tip touched the nanofiber, giving a value of less than 5 nN, however, the static friction can be somewhat higher. Also, there can be a difference between the static friction experienced in the first pushing cycle and in subsequent cycles[129]. This additional friction could be caused by agglomeration of residues around the nanofiber during the evaporation of the water, in which the nanofibers were dispersed. Cutting out a small piece of nanofiber of similar size by performing a pushing cycle on either side, and then performing a pushing cycle on this remaining piece allows an estimate of the initial static friction to be made, which is of the order of 60 nN. This suggests that the primary contribution to the lateral force data is from rupturing of the nanofiber. Assuming a static friction of 60 nN, the rupture force is 380 nN and 450 nN, respectively. The difference between these two values can be partly attributed to the fact that the nanofiber does not have a completely uniform width along its length. The rupture shear stress can be estimated from the values of rupture force and cross sectional dimensions yielding values of $1.7 \cdot 10^7$ Pa and $2.0 \cdot 10^7$ Pa for the stress necessary to rupture a nanofiber. This is approximately one order of magnitude lower than the rupture stress of a similar-sized fibrin fiber as investigated by Guthold and co-workers using a similar method[140]. Given that fibrin fibers are biological structures with a mechanical task, this comparably high p6P fiber strength is rather remarkable.

After the rupture of the nanofiber the lateral forces curves decay back to a value close to zero. The decay rate is approximately constant for the first 0.1 μm of tip travel after rupture during which the force drops to one fifth the rupture value. This is attributed to a continued interaction between the cut-out piece of nanofiber and the remaining sidewalls since the magnitude of this interaction must be assumed to scale with contact area.

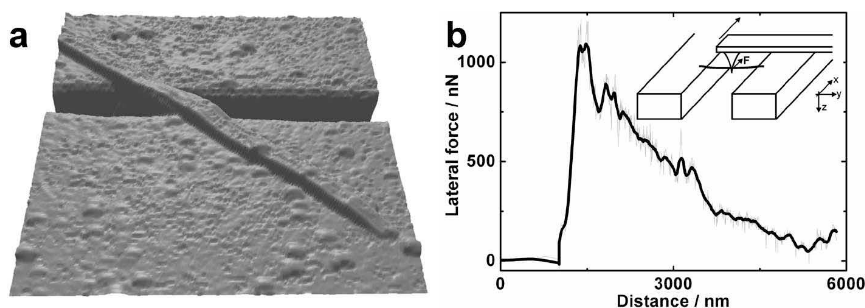

Figure 3.10: (a) 12.6 μm by 12.6 μm AFM image of a 0.9 μm wide and 80 nm tall p6P nanofiber suspended across a 1 μm wide trench (obtained before manipulation). (b) Measured (grey) and averaged (black) lateral force values during manipulation. Inset shows a schematic drawing of the manipulation experiment, where the AFM tip is first lowered next to the suspended nanofiber and then moved horizontally.

Suspending a nanofiber between two supporting structures allows rupture experiments, in which the contribution from friction is eliminated. Fig. 3.10(a) shows a doubly-clamped p6P fiber, on which the rupture properties were probed by slicing through the free-standing part of the fiber with the AFM tip as shown schematically in the inset of fig. 3.10(b). This resulted in the lateral force values displayed in fig. 3.10(b). The rupture force of 1.1 μN of this 900 nm wide and 80 nm high fiber corresponds to a shear stress of $1.5 \cdot 10^7$ Pa. The nanofiber breaks in just one position and not two as the supported nanofibers do. The shear stress value corresponds reasonably well with the result obtained from a supported nanofiber. The very long decay length seen in fig. 3.10(b) is presumed to be due to the subsequent pushing of the broken nanofiber against the trench wall.

A suspended nanofiber also facilitates investigation of its elastic properties. Deflecting the nanofiber with the AFM tip as depicted in the inset of fig. 3.11(b) caused a mechanical response as shown in fig. 3.11(b).

When deflecting a suspended nanofiber the force scales nearly proportionally with the deflection. Starting from a position above the nanofiber bridge and lowering the AFM tip causes a distinct increase in the force when the AFM tip touches the nanofiber. This onset occurs at almost the same position in both cycles, which indicates a nearly reversible deflection of the

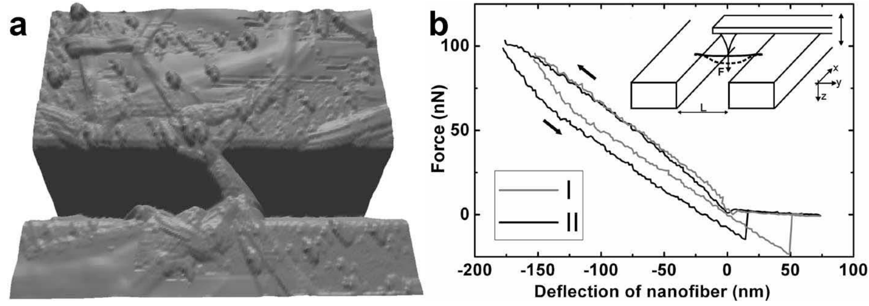

Figure 3.11: (a) 14.4 μm by 14.4 μm AFM image of a 0.5 μm wide and 100 nm tall p6P nanofiber suspended across a 3 μm wide and several μm deep channel. (b) The force F applied to the nanofiber versus deflection of the nanofiber u during two pushing and retraction cycles. The arrows indicate which curve is pushing and which is retraction. Note that the deflection of the AFM cantilever has been subtracted; these deflection values are from the suspended nanofiber only. Inset shows a schematic drawing of the pushing experiment where the AFM tip is used to deflect the suspended nanofiber.

nanofiber bridge with little permanent plastic deformation. This suggests that the deflection is not causing severe changes to the internal structure. A hysteresis effect between pushing and retraction can be observed. This can be attributed to the tip sliding on the nanofiber during the deflection experiment.

When modelling the force response of a suspended rod, one can either consider a stiff rod where the force is used to overcome the bending rigidity, an elastic string where the force causes stretching, or some combination of these two. Whether bending or stretching dominates is primarily determined by the thickness of the rod compared to the deflection: at small deflections the bending part contributes the most, whereas for larger deflections the stretching contribution becomes dominant[141]. In this case, the p6P nanofiber is deflected up to less than twice its height, and the bending rigidity is therefore assumed to contribute the most. This assumption is also justified by the appearance of the force-distance curves, since a stretching contribution to the force would scale with the cube of the deflection[141]. In these measurements very little third order dependence can be seen.

However, the applied force is not necessarily the only factor determining the deflection. If there is a built-in tension T_0 in the nanofiber produced during the formation of the nanofiber bridge, this must be included as well. Assuming only small deflections, the deflection u of the suspended rod must satisfy[142]

$$EI\frac{d^3u}{dy^3} - T\frac{du}{dy} = -\frac{F}{2}. \tag{3.5}$$

Here E is Young's modulus, I is the plane moment of inertia, and T is the overall tension equal to the sum of the built-in tension and the extra tension caused by the deflection. Solving eq. 3.5 at constant T with the appropriate boundary conditions and fitting with the measured force vs. deflection data provides an empirical expression for Young's modulus in terms of the initial, unknown built-in tension T_0

$$E = -1.6 \cdot 10^{15}\mathrm{m}^{-2} \cdot T_0 + 6.5 \cdot 10^8 \text{ Pa}. \tag{3.6}$$

Assuming negligible built-in stress, eq. 3.6 predicts a Young's modulus of the nanofiber of 0.65 GPa. However, since it is not possible to deduce the exact value of built-in stress, the quoted value of 0.65 GPa constitutes an upper bound. For comparison, low density polyethylene has a Young's modulus of 0.2 GPa[143].

Sliding Properties

Sliding experiments were performed on p6P nanofibers supported by the hydrophobic surface in order to minimize the friction between the nanofiber and the surface. Similar to the experiments described previously, an individual nanofiber was located by AFM and lateral manipulation was attempted. Fig. 3.12 shows several nanofibers during the manipulation experiment along with the measured values of lateral force.

In the microscopic regime, friction normally scales with interface area[116] in contrast to macroscopic systems. Fig. 3.12(f) shows the lateral force (i.e. the friction) necessary to manipulate a nanofiber vs. interface area, which is estimated from cross-sectional profiles of deconvoluted data. The observed behavior more resembles what is seen for macroscopic systems.

For off-center manipulation the nanofiber tended to rotate around an axis perpendicular to the surface and only occasionally experienced pure translation. Fig. 3.13 shows a series of AFM images of a nanofiber being manipulated. Similar behavior has been observed in 2-D manipulation of a carbon nanotube[133], in which case, however, the friction scales with interface area. The in-plane rotation occurs around a pivot point, the position of which depends on the tip-nanotube contact point. If the AFM tip pushes side-on near the nanotube center, the pivot point will be close to the nanotube end. Pushing at a position closer to one of the nanotube ends will cause it to rotate around a point closer to its center. Similar features can be observed in fig. 3.12, where pushing near the end (first push) causes rotation about a pivot point located approximately one fourth up the nanofiber whereas pushing near the center (second push) causes the pivot point to be at the end of the nanofiber. This indicates a uniform friction along the length.

As seen from the AFM images in fig. 3.12, lateral manipulation of a piece of a nanofiber on the low-friction surface is possible without rupture.

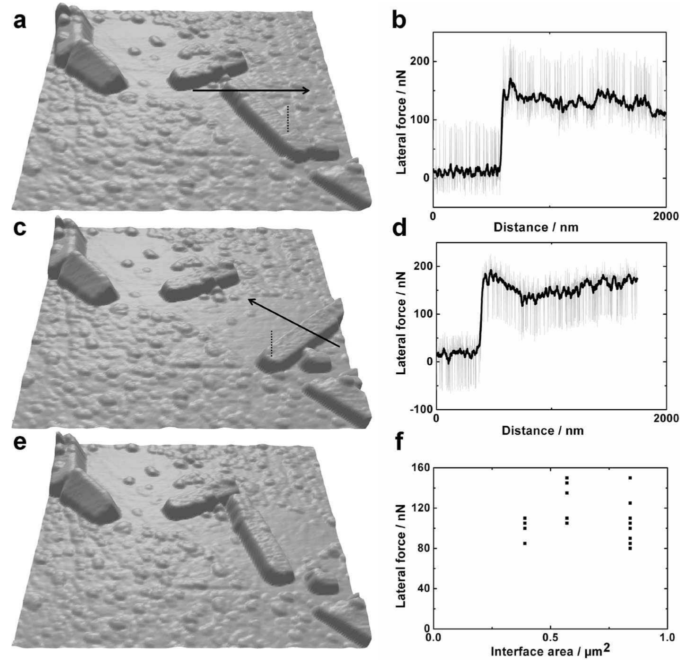

Figure 3.12: (a) 5.1 μm by 5.1 μm AFM image of several p6P nanofibers on a silicon substrate with the low-adhesion coating before manipulation. The arrow indicates the trajectory of the AFM tip during manipulation while the dotted line indicates the pivot point, around which the nanofiber rotates. (b) The grey and black curves are the measured and averaged lateral force, respectively, during the first manipulation. (c) AFM image of the same area after the first manipulation. The arrow indicates the trajectory of the AFM tip during the second manipulation while the dotted line indicates the pivot point. (d) The grey and black curves are the measured and averaged lateral force, respectively, during the second manipulation. (e) AFM image of the same area after the second manipulation. (f) Lateral force necessary to manipulate p6P nanofibers does not change significantly as a function of interface area. The interface area is estimated from the full-width at half-maximum cross sectional profiles of deconvoluted data.

However, as seen in the last image in fig. 3.13 the nanofiber eventually breaks. Manipulation experiments were performed on three different nanofibers with lateral forces corresponding to shear stresses between $3 \cdot 10^6$ Pa and $6 \cdot 10^6$ Pa, which is approximately three to seven times smaller than the rupture shear stress. Whether the nanofiber moves or breaks is determined by how the shear stress in the nanofiber compares to the friction between the nanofiber and the substrate: if the shear stress rises above the rupture value before the friction is overcome, the nanofiber will break.

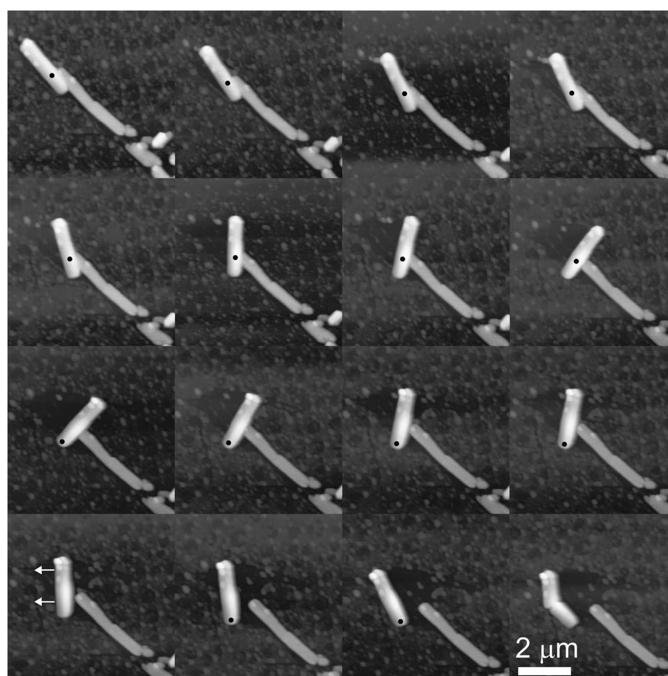

Figure 3.13: Sequence of AFM images (left to right) of several p6P nanofibers on a silicon substrate coated with (tridecafluoro-1,1,2,2-tetrahydrooctyl)trichlorosilane. Between each frame the AFM tip is used as a manipulation tool to move one of the nanofibers. Black dots indicate the pivot points around which the nanofiber rotates while white arrows indicate translation. The height scale is from 0 nm (dark) to 85 nm (bright).

The above experiments demonstrate that although difficult, it is possible to slide nanofibers via AFM based manipulation. The AFM has the advantage of providing quantitative data of the exerted force and useful information of the mechanical properties. However, it is less practical in the assembly of nanofiber structures, both due to the fact that it is rather time consuming, it does not allow observation during manipulation, and that the point-like nature of the applied force makes it difficult to control whether the nanofiber rotates or translates. This can be overcome by using the 3-D manipulation system described in section 3.2.2 for 2-D manipulation. Here, a cantilever is used as the manipulation tool to slide nanofibers along the surface with a better control of the direction. This has allowed the fabrication of simple nanofiber structures as seen in fig. 3.14, which shows the letter 'T' constructed from several nanofibers. Although the assembly method does seem to partly disrupt the nanofiber morphology as seen from the AFM image in fig. 3.14(c), the polarization properties of the luminescence are intact.

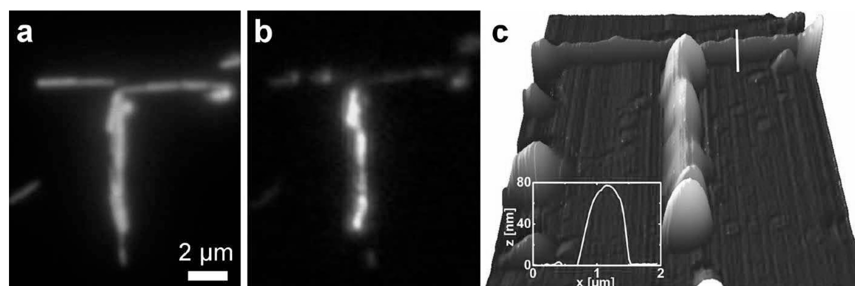

Figure 3.14: An artificial 'T' constructed from p6P nanofibers. (a) Fluorescence microscope image excited with light of 365 nm wave length and observed unpolarized. (b) Similar to (a) but observed with horizontal polarization c) AFM image of the 'T'. Inset shows cross sectional profile along the indicated line. The assembly of this 'T' structure was performed by M.Sc. student Jeanette Hvam.

The 2-D manipulation studies have demonstrated that the p6P fibers are fragile structures and that 2-D manipulation is limited to nanofibers on a low-adhesive surface. However, although the nanofibers are indeed much more fragile than for example carbon nanotubes, they can be self-supporting and can be deflected elastically without breaking as shown in fig. 3.11. This suggests that a gentle manipulation technique, which does not cause a large nanofiber deformation, could enable pick-and-place operations.

3.5.2 3-D Manipulation of Organic Nanofibers

The problem of picking up a fragile nanofiber is that the adhesion forces to the substrate are so strong that in order to lift up the nanofiber, a large force must be applied that will cause the nanofiber to break before it is released. A possible solution is to minimize the contact area towards the substrate and thus the adhesion forces. Since the morphology of the nanofiber is given, the solution must be a substrate that has as small a contact area to the nanofiber as possible. This could be a structure consisting of a lot of microscopic, vertical columns to support the nanofiber in only a number of discrete points as depicted earlier in fig. 3.4(d). In collaboration with Kjetil Gjerde, a surface coated with vertically aligned carbon nanotubes - a nanotube forest - was made, which acts as a non-stick workbench for the manipulation of nanocomponents[129]. Such a nanotube forest not only exhibits very low adhesion, it also acts as a mechanically compliant substrate that the tool can penetrate into thus lifting up the nanofiber from below.

This nanotube forest was used for 3-D manipulation experiments on p6P nanofibers, which had been transferred here from a aqueous dispersion. As described in section 3.3, the tool has to be selected for the particular

application. Here, the most efficient tool was the sharp wire tip, which could penetrate the nanotube forest next to the nanofiber, move in below, and lift it off. This type of manipulation was tested both in the experimental set-up with the optical microscope described earlier and by using a commercial robot system mounted inside the vacuum chamber of a SEM. Fig. 3.15 shows the SEM experiment where a tungsten wire tool is used to pick up a p6P nanofiber from a nanotube forest and place it on a target substrate.

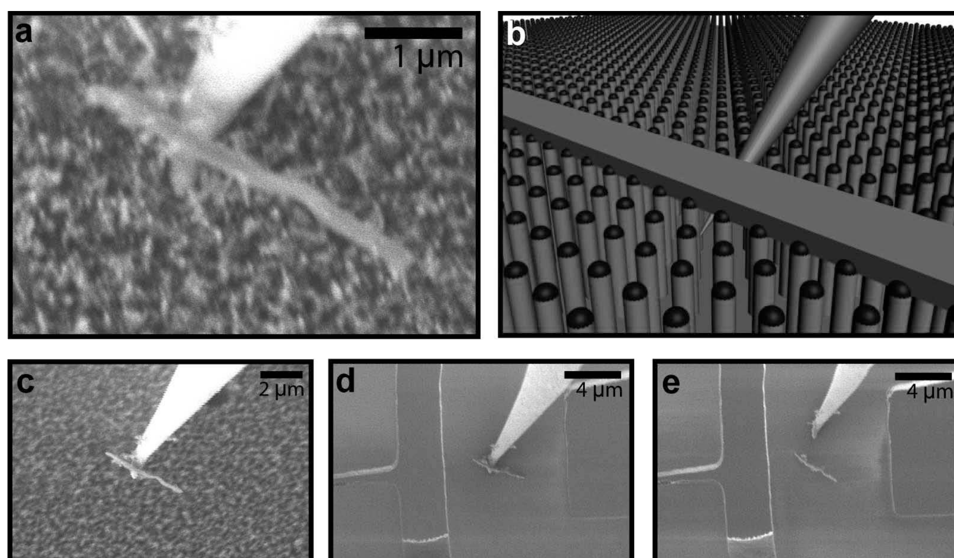

Figure 3.15: (a) The sharp tip of a tungsten wire is approached to a p6P nanofiber resting on top of a nanotube forest and moved underneath the fiber. (b) Illustration of the manipulation technique: The tip is moved beneath the nanofiber slightly into the mechanically compliant nanotube forest. The nanofiber may then be lifted by pulling the tip vertically up. (c) The nanofiber is lifted off the nanotube forest by pulling the tip up. (d) The nanofiber is then placed onto the target structure. (e) By pulling the tip away, the nanofiber remains on the target structure, as it has been moved from a surface with low adhesion to a surface with higher adhesion.

Fig. 3.15 demonstrates how the combination of the compliant nanotube forest and the sharp tool can allow release of the fragile nanofibers as observed with the high resolution capabilities of a SEM. However, despite the poorer resolution, the optical microscope based system equally well facilitated manipulation of the organic nanofibers.

A faster and simpler method of nanofiber transfer has also been used, which however, provides less control over the exact number and position of the transferred nanofibers. This method uses a micropipette with a tip diameter of $\sim 10\ \mu$m mounted in a small set-up that fits on a 3-axis trans-

lation stage under an optical microscope as shown in fig. 3.16(a). First, a small amount of water is ejected onto the nanofiber growth substrate. This releases some of the nanofibers into the water. A syringe connected to the micropipette is used to draw the nanofiber dispersion back into the micropipette. The target substrate is then approached to the micropipette and a droplet of the nanofiber dispersion is ejected here. After the water has dried, a number of nanofibers remain on the target substrate.

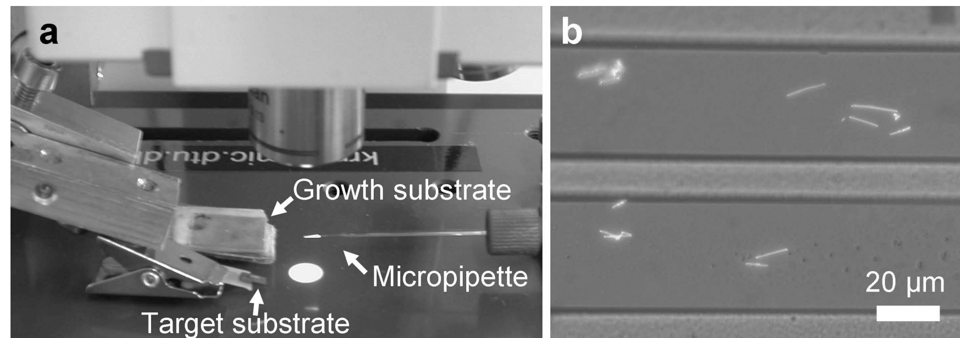

Figure 3.16: (a) The micropipette set-up for nanofiber transfer. The set-up is mounted on a translation stage beneath an optical microscope to facilitate observation during transfer. (b) Combined fluorescence and white light microscope image showing two elevated silicon dioxide supports (similar to the illustration in fig. 3.5(b)), each with a few p6P nanofibers transferred with a micropipette.

The number of transferred nanofibers cannot be controlled exactly. Typically it is of the order of 10 to 20. Using a target substrate consisting of an elevated silicon dioxide platform allows some control over the deposition area. Fig. 3.16(b) shows two such 35 μm wide platforms, each on which a small amount of nanofiber dispersion has been placed. The surface tension of the water prevents it from flowing off the elevated structure thus confining the nanofibers here. Although this method does not provide the same accuracy as pick-and-place of individual nanofibers, it has sufficient accuracy to facilitate electrical characterization of individual nanofibers through the shadow mask technique described next.

3.6 Integration by Shadow Masking

By combining the 3-D manipulation techniques described in the previous sections with metal evaporation, an efficient method of fabricating a significant number of prototype devices based on nanocomponents has been developed and tested. This method is inspired by the work of de Pablo and co-workers[144]: A tungsten wire was placed across a nanotube lying

on a glass substrate and then glued at the edges of the substrate, upon which a second, larger mechanical mask was placed to cover the glue. The tungsten wire acted as a shadow mask during metal deposition and left a $\sim$ 4 μm gap in the deposited metal, corresponding to the width of the wire. Where the tungsten wire crossed the nanotube, the gap in the metal electrode was bridged only by the nanotube. This method was adapted to work on a smaller scale using thin Si wires as shadow masks by Søren Dohn[145]. Using a microfabricated silicon dioxide structure as shown in fig. 3.5(b) as target structure, electrical contact to individual manipulated nanostructures can be made, while a more complicated microcantilever platform allows the piezoresistive properties of the nanocomponent to be characterized.

The method relies on using a silicon wire as a shadow mask during deposition of metal electrodes by thermal evaporation. The shadow mask is kept in place on the target structure by surface adhesion. Avoiding fixation by glue permits integration of a nanocomponent on a free-hanging cantilever structure similar to a piezoresistive strain sensor integrated in cantilevers for force or biochemical sensing[146]. By 3-D manipulation, a nanocomponent is picked up and transferred to the target structure, either the simple oxide structure or the cantilever, where it is placed and aligned along the long axis. Next, a silicon wire is picked up and positioned across the nanocomponent, perpendicular to the long axis of the target structure and extending across the edges. After metallization of the structure, removal of the shadow mask leaves two metal electrodes only connected through the nanocomponent, spanning a $\sim$0.2-1 μm gap as shown in fig. 3.17.

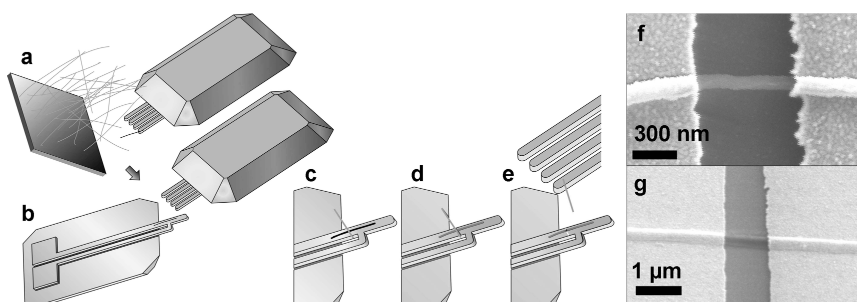

Figure 3.17: (a) The manipulation tool is used first to pick up a single nanocomponent and (b) then to position it along a silicon oxide cantilever. (c) A $\sim$ 0.5 μm wide shadow mask wire is positioned across the cantilever. (d) An appropriate metal is deposited onto the structure by thermal evaporation. (e) Removal of the shadow mask results in two metallic electrodes interconnected by the nanocomponent. The SEM images show (f) a MWCNT and (g) a p6P nanofiber (that had been deposited on the target substrate with a micropipette.) contacted with the shadow masking technique.

For certain applications it may prove advantageous to be able to use contacts of different materials. One example is light emission from electroluminescent materials such as p6P. Different anode and cathode materials make it possible to optimize for injection of electrons and holes, respectively, as described in chapter 6. To investigate the possibility of creating such hetero-contacts, the shadow mask method has been extended to allow deposition of different contact materials. Two shadow masks are used in these preliminary experiments: a silicon wire and a flake of silicon with side lengths of a few μm. Again the silicon wire shadow mask is placed across the nanocomponent on the oxide structure. Next, a second shadow mask is picked up and placed adjacent to the first, partly covering the nanocomponent. After evaporation of the first metal layer the silicon flake is removed and the second, different metal layer is deposited. The final removal of the silicon wire shadow mask results in the desired configuration as illustrated in fig. 3.18.

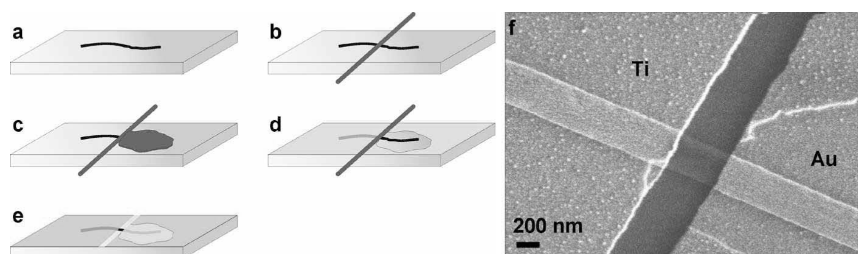

Figure 3.18: (a) A nanocomponent is positioned on the oxide structure and (b) a silicon wire shadow mask is positioned across. (c) A flake of silicon is positioned to cover part of the nanocomponent. Evaporation of the anode metal and removal of the flake of silicon (d) is followed by evaporation of the cathode metal and finally removal of the silicon wire shadow mask, which gives the desired configuration (e). Choosing the appropriate contact metals allows modification/lowering of the barriers at the two interfaces and thereby the tuning of the electrical properties. (f) SEM image of a p6P fiber contacted with the hetero-contact shadow masking method.

The shadow mask method was used for further investigations of both MWCNTs and p6P nanofibers, which are the topics of chapter 5 and 6. Here, some of the general issues of the shadow mask method are discussed, whereas the specific details regarding the investigated structures will be treated in the later chapters.

The shadow mask method provides electrical contact to a nanocomponent, which can then be electrically characterized by connecting the two metal electrodes to external circuitry. During this project, a LabVIEW based measurement system was made in combination with the manipula-

tion set-up. It consists of a LabVIEW controlled, 16 bit data acquisition (DAQ) card and a Stanford Research SR-570 current preamplifier. The DAQ card supplies a DC voltage or sweeps the voltage within a predefined range. Simultaneously it reads the resulting current through the current preamplifier, which can measure current levels down to the sub-picoampere range - particularly suited for structures with a low conductance such as the p6P fibers. Alternatively, a more simple set-up consisting of a Keithley 2400 voltage source and current meter was used for characterizing structures with a higher conductance. The shadow mask method was tested with different nanocomponent devices, which were then electrically characterized with fig. 3.19 showing typical examples of current-voltage characteristics.

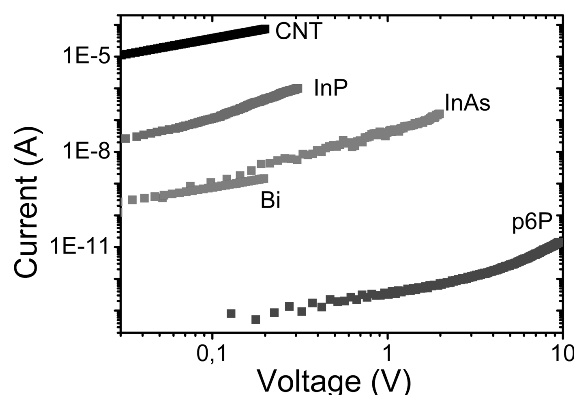

Figure 3.19: Current-voltage characteristics of a multiwalled carbon nanotube (CNT), an indium phosphide nanowire (InP), an indium arsenide nanowire (InAs), a bismuth nanowire (Bi) and a para-hexaphenylene nanofiber (p6P).

In its present form, this method is best suited for nanocomponents on which a native oxide layer does not form, since the removal of such a layer prior to metal deposition will be difficult. The electrical characteristics of for example bismuth nanowires as shown in fig. 3.19 show a conductance significantly below what should be expected for pristine bismuth, which presumably is due to a native oxide layer.

The yield of the shadow mask method is dependent on a number factors. In general, using this method requires some practice and the yield will therefore to some extent depend on the operator. However, there are some inherent issues, which will lower the yield. Since the shadow mask wire is only fixed by the adhesive surface forces, it can move during handling. It has occasionally been observed that the shadow mask had moved before metal deposition and had therefore not shadowed at the intended position. This problem can minimized by careful handling, although it was not completely

eliminated. Occasionally, the removal of the shadow mask turned out to be hindered by the metal layer. If the shadow mask wire was too thin compared to the metal layer, it would break and removal would be impossible. Depending on wire diameter, this would typically happen when the metal layer thickness was above $\sim$ 200 nm suggesting an upper limit for the layer thickness. However, the metal layer must be sufficiently thick to clamp the nanocomponent, as it in some cases was observed that mechanical influences during the removal of the shadow mask could cause the nanocomponent to move. An additional problem was electrostatic discharge. After metal deposition, the electrodes are connected to macroscopic contacts on a handling substrate through ultrasonic wire bonding. After wire bonding, the devices became quite susceptible to outside disturbances. Despite great care in the handling of devices including electrical grounding of all measuring equipment that came in contact with the devices, a number of devices were lost due to an electric discharge, unfortunately often seen with nanodevices.

3.7 Summary

Manipulating matter at the micro- and nanoscale requires overcoming the adhesive forces that dominates at these length scales. AFM based 2-D manipulation enables the probing of intrinsic properties of nanostructures and their interaction strength with a substrate. Pick-and-place operations with the objective of fabricating prototype devices based on nanocomponents are feasible, but requires a careful consideration of the component properties and initial arrangement - in particular with respect to choice of manipulation tool. A 3-D manipulation set-up, based on an optical microscope, has been constructed and has enabled pick-and-place operations with a number of nanostructures ranging from robust carbon nanotubes to very fragile organic nanofibers. Whereas the manipulation of robust structures is relatively straight-forward, fragile components require a special manipulation substrate with a small interaction strength. Based on 3-D manipulation, a resist-free shadow mask method has been developed, which allows contacts to be made to individual nanocomponents.

Chapter 4

In-situ Growth of Carbon Nanotubes

Integration by manipulation as described in the previous chapter has the advantage of providing a reasonably flexible and straight-forward route for fabricating a moderate number of prototype devices suitable for a systematic optimization. However, technological use requires the ability to fabricate a larger number of devices with a much higher throughput. One of the most promising techniques for parallel integration of carbon nanotubes is in-situ growth, where a suitable catalyst material facilitates the fabrication of carbon nanotubes through chemical vapor deposition. This chapter will investigate the possibilities of integrating MWCNTs on cantilevers by in-situ growth in order to evaluate the potential of using this as an integration method. Here, the task of precisely positioning individual MWCNTs in a microsystem is changed to accurately positioning catalyst particles from which the nanotubes will grow. This positioning is possible by cleanroom fabrication techniques and thus has the potential of high-volume fabrication.

A MWCNT integrated on a cantilever can have several applications. For example it can be used as an AFM tip for imaging high aspect ratio structures[131]. Another application could be as tips on microscale four-point probes for local surface conductance measurements[147]. Here, short nanotube tips would provide durable and reproducible electrical contact due to the mechanical strength of nanotubes. In such applications the nanotube(s) would typically be perpendicular to the cantilever surface and either no or just one electrical connection to each nanotube would be necessary. Thirdly, nanotubes on cantilevers can be used as sensors[148], however, for such applications two electrical connections are necessary to monitor the nanotube resistance. This requires the nanotube to span a gap between two electrodes, for instance accomplished by growing the nanotube from one electrode to another. Several methods can be considered for achieving lateral growth. As described in chapter 2, an electric field can be applied to

align the growth direction with the electric field[73]. However, other options have been suggested. One possibility is to deposit a growth barrier layer on top of the catalyst leaving only the sidewall exposed to the carbon feedstock during growth thereby causing the MWCNT to grow along the substrate surface[149, 150]. A third method, demonstrated for SWCNTs, is to use the direction of a streaming gas to guide the growth direction[151]. Here, the method of electric field guided growth has been chosen, which requires the accurate prepositioning of catalyst particles on top of electrodes defined on a cantilever structure.

The first part of this chapter will therefore deal with the development and testing of process recipes for realizing an appropriate microsystem for nanotube growth including accurately positioned catalyst particles and electrodes for setting up an electric field during growth. This part will specifically deal with lateral nanotube growth although a successful process recipe can also produce microsystems for vertical growth. This work was made in a collaboration with Kjetil Gjerde. The second part will focus on the experimental set-up for nanotube growth. Here, the constructed set-up and its initial optimization will be outlined followed by a description of the experiments performed on in-situ growth of MWCNTs.

4.1 Microsystem Design and Fabrication

The aim of the microfabrication process is to produce a cantilever chip with an appropriate electrode pattern on the cantilever. On top of the electrodes, suitable-sized catalyst particle(s) must be placed at selected positions. Fig. 4.1 shows a conceptual drawing of a cantilever with electrodes and a CNT bridging the electrodes.

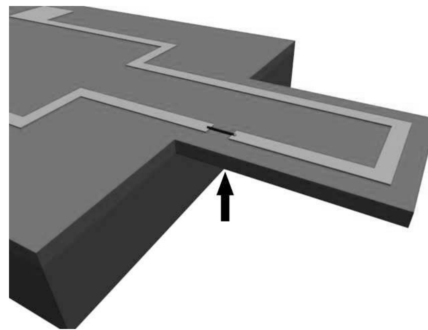

Figure 4.1: Conceptual drawing of a cantilever for in-situ growth of MWCNTs between opposing electrodes. The cantilever extends from a chip base on which the electrodes end up in large contact pads. A CNT bridging the two electrodes is indicated with the arrow.

A central point to be addressed before the development of a suitable process recipe is the choice of materials. A silicon wafer will be used as the starting point. The cantilever itself will be made from silicon dioxide. This has the required properties of being electrically insulating, it has suitable mechanical properties, and it is easily fabricated on the Si wafer. In addition, a process recipe for realizing silicon dioxide cantilever structures exists[152]. This can serve as a starting point for the development of a new process recipe. The electrode material must satisfy several requirements. It must be electrically conducting to set up the required field during growth and to provide electrical contact to the nanotube after growth. In addition, it must act as a barrier towards the catalyst material to avoid mixing when heated to high temperatures since this will inhibit nanotube growth[153]. Molybdenum has been shown to be a suitable electrode material for nanotube growth[13]. A second candidate is titanium nitride[154]. The similar characteristics of titanium tungsten makes this a third, promising alternative[155]. In these experiments, Mo has been chosen since this initially was the only available material of these three. At a later stage TiW became accessible and could also be tested. Finally, the catalyst material must be chosen. Several materials have been reported such as Fe, Co and Ni[68]. Here, Ni was chosen as the catalyst material since its use is well established and widespread for MWCNT growth[156].

A second crucial point is the available microfabrication equipment. The preprocessing of the microsystem for MWCNT growth was performed in the DANCHIP cleanroom at the Technical University of Denmark. The process recipes were therefore developed to be compatible with the equipment of this cleanroom. Most structures including the cantilever and the electrode patterns can be made by microfabrication techniques using conventional photolithography for pattern definition. A lithography technique capable of defining sub-100 nm structures is required to fabricate catalyst particles with a size small enough to ensure that only one MWCNT will grow from each particle[76]. For this purpose, electron beam lithography has been chosen.

For the realization of the cantilever microsystem, three photolithography masks are necessary: one for defining the cantilever geometry, one for the electrodes, and one for the entire chip, which is etched out in KOH from the wafer backside. The masks have been designed in a hierarchical way so that all 84 chips on a 4" wafer are electrically connected to two large contact pads to allow the parallel application of an electric field to all chips simultaneously. The individual chips were also grouped in clusters of six connected to two smaller contact pads to facilitate parallel growth on a smaller number of chips. Finally, individual chips can be taken out for single-chip test runs.

4.1.1 Process Recipe Development

Integrating the Ni catalyst in the microsystem processing poses a significant challenge. Preferably, the electron beam lithography (EBL) step for defining the Ni catalyst should be performed at an early stage of the processing on a nearly planar wafer. This would ease the deposition of thin, homogenous layer of EBL resist. However, the microsystem fabrication requires the deposition of a silicon nitride film on the cantilever structure at a later processing step. If this process is performed with any Ni exposed, the chemical vapor deposition equipment will become contaminated with Ni. This can have a negative impact on other microsystems that are made with this equipment and is therefore unwanted. Therefore, the strategy of fabricating the Ni particles early in the process cannot be used directly. To solve this problem, several process recipes have been developed that would circumvent the problem of the Ni catalyst contaminating the equipment.

Electron Beam Lithography on Released Cantilevers

An apparently simple way of avoiding the problem of Ni contamination is to postpone the deposition of Ni until the very end of the processing. This would involve realizing the cantilever structure first by conventional microfabrication techniques. The basis for this is the process recipe developed and optimized by Christian Leth Petersen[167] and Torben Mikael Hansen[152] for the fabrication of micro four-point probes. These consist of four free-hanging silicon dioxide micro cantilevers extending from a silicon support chip. By extending the process recipe to include extra steps to define and fabricate the electrode pattern, this could provide the desired structure.

The process starts with two photolithography steps for defining the electrode and cantilever structures with appropriate intermediate steps of electrode material deposition, lift-off, and etching. Next the backside is processed by a further photolithography step and subsequent etching in KOH to etch out the chips and release the cantilevers. At this point, the EBL resist is applied. Depositing a resist layer with a uniform thickness on top of the released cantilevers can be difficult. Applying the resist by spin coating will result in a very inhomogeneous layer thickness due to the surface topography that would interrupt the resist flow during spinning. An alternative method is to apply the resist by spray coating, which can provide a better coverage on 3-D structures. Following resist deposition, the exposure and development is performed. Finally, the Ni particles are fabricated by electron beam evaporation and lift-off.

In-situ Mask

The second strategy also avoids the contamination issue by postponing the Ni deposition until all microfabrication steps have been completed. Rather

than performing EBL on free-hanging structures, the pattern for the Ni catalyst is made early in the process when the wafer has only sub-100 nm high surface corrugations caused by the electrode structure. The catalyst pattern is then transferred to a sacrificial mask layer on top of the electrode structure. After performing all microfabrication steps for realizing the cantilever and chip structure, the Ni can finally be deposited and the sacrificial in-situ mask layer can be dissolved in a special lift-off process to produce the desired Ni pattern.

The material for the sacrificial layer must fulfill several requirements. Since it should be deposited at an early stage in the process, it will be present during most microfabrication steps and it must therefore not give rise to any contamination. It must also be sufficiently stable to endure the processing without the pattern for the Ni particles degrading significantly. Finally, it must be possible to dissolve the mask material in a final lift-off process to realize the Ni pattern. A possible material is polycrystalline silicon (p-Si), which can be applied by sputtering. By taking its properties into account during process recipe development it can endure the microfabrication processes, it does not pose any contamination risk, and it can be dissolved in KOH, which does not etch Ni.

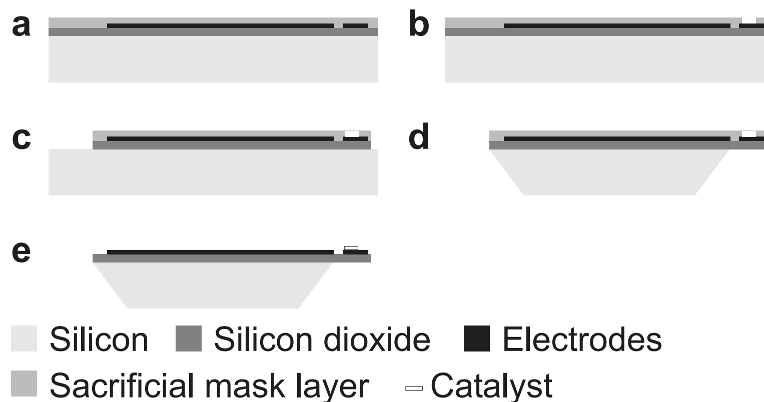

Figure 4.2: Cross-sectional drawings of a single cantilever chip made with the in-situ mask recipe at various stages during fabrication (excluding possible additional layers on the backside). (a) Using photolithography, the electrode material is patterned on a silicon dioxide layer. On top of this, a sacrificial mask layer is deposited. (b) By electron beam lithography and anisotropic etching the catalyst pattern is realized in the sacrificial mask layer. (c) The cantilever structure is defined by photolithography and is etched out. (d) A third photolithography step defines the chip outline on the backside and the chip is etched out in KOH, which releases the cantilever while the frontside is protected (frontside protection not shown). (e) The catalyst material is deposited and a special lift-off of the sacrificial mask layer is made in KOH.

The starting point is a double polished Si(100) wafer. By thermal oxidation a silicon dioxide layer is grown. The cantilever will later be realized in this layer so its thickness should be determined by the requirements for the mechanical properties of the cantilever. A photolithography step to define the electrode pattern is followed by deposition of the electrode material (Mo or alternatively TiN or TiW) and lift-off. The sacrificial mask layer is then deposited on the frontside, here p-Si by Ar sputtering. The wafer frontside now appears as seen in fig. 4.2(a). This surface will only have small corrugations (not shown) caused by the electrode pattern beneath the sacrificial mask layer. Next, an EBL step is made to define the catalyst pattern followed by an anisotropic etch that transfers the pattern to the sacrificial layer as shown in fig. 4.2(b). The cantilever and chip frontside pattern is then defined by photolithography and etched out leaving the frontside as depicted in fig. 4.2(c). Next, the attention is turned to the backside, where the chip outline is defined and the chips are etched out from the backside in KOH with appropriate protection of the wafer frontside; see fig. 4.2(d). The cantilevers have now been released, and the final steps consist of Ni deposition and lift-off to fabricate the catalyst particles.

Encapsulating Layer

The third and final strategy relies on fabricating the Ni catalyst particles at an early stage and then covering these with an encapsulating layer that prevents the Ni from contaminating the process equipment during the remaining processing. First, the Ni pattern is made on top of the electrodes. After deposition of the encapsulating layer over the Ni particles, the remaining front and backside processing can be performed. Finally, the encapsulation can be removed to yield the desired structure.

For this recipe the choice of encapsulating material is important. The material must enclose the Ni particles sufficiently well to avoid any Ni to penetrate and possibly cause contamination. In addition, it must be possible to remove this layer without harming the Ni particles, which will become exposed during encapsulation removal. Also, the remaining structure should not be degraded. Due to equipment restrictions, no chemical vapor deposition techniques could be used for deposition on exposed Ni. Therefore, the encapsulating layer must be deposited by some physical vapor deposition technique. Here, Al is chosen since it does not contaminate the processing equipment and a sufficiently thick layer will provide adequate encapsulation of the Ni. Also, Al can supposedly be removed selectively over Ni with a suitable etchant. The Aluminum Etchant Type D from the company Transene has a selectivity to Al over Ni by more than 100. Also, it does not etch the other used materials and was therefore considered a suitable etchant.

The process recipes starts out in a similar fashion to the previous one with silicon oxidation and electrode pattern fabrication. Next, the catalyst

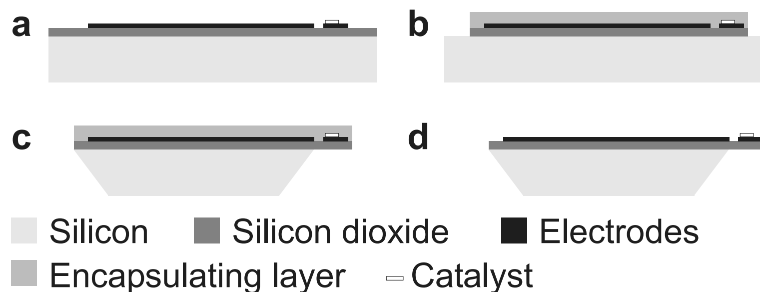

Figure 4.3: Cross-sectional drawings of a single cantilever chip made with the encapsulating layer recipe at various stages during fabrication (excluding possible additional layers on the backside). (a) Photolithography is used first to pattern the electrode material on a silicon dioxide layer. Then, EBL is used to fabricate the pattern for the catalyst particles and Ni is deposited and lifted off. (b) The Ni particles are covered by an encapsulating layer of Al that is structured by photolithography to also serve as an an etch mask for the cantilever realization. (c) The backside is processed similar to the in-situ mask recipe, and finally (d) the encapsulating layer is removed selectively from the Ni particles.

pattern is defined by EBL on top of the electrodes and Ni is deposited and lifted off. This leaves the frontside as depicted in fig. 4.3(a). The encapsulating layer of Al should now be deposited. However, the Al deposition is preceded by a photolithography step to pattern the Al layer. In this way, the Al layer serves an additional purpose as an etch mask for the cantilever realization; see fig. 4.3(b). Then, the backside is processed like in the previous case, while the frontside is protected, resulting in the structure shown in fig. 4.3(c). The final step is the removal of the Al encapsulation which leaves the desired structure as fig. 4.3(d) shows.

Recipe Comparison

The strong points of the first strategy are its simplicity and the late introduction of the catalyst material. It avoids any additional layers for realizing the in-situ mask or the encapsulation. Also, this process facilitates a possible change of catalyst material without any changes to the recipe. This could be beneficial if for example Fe or Co should be tested. The late introduction of the catalyst material also precludes the possibility of the catalyst being affected during microsystem processing. Its main weakness is the difficulty in achieving a suitable, uniform layer of EBL resist on released structures.

The in-situ mask approach has the same advantage of allowing most catalyst materials. In addition, it avoids the problem of applying EBL resist on a wafer where the individual chips have already been etched out.

A potential problematic issue can be that of realizing and maintaining the desired dimensions of the holes in the in-situ mask. The mask will be covered with different materials that are later etched away during processing of the cantilever and the chip backside. This could possibly degrade the mask pattern which could enlarge the catalyst particles or hinder the final lift-off. A second issue is whether it is possible to fully remove these different materials, or if some residues could remain and contaminate the catalyst.

The encapsulating layer strategy avoids these problems. This method relies on the etch selectivity between Al and Ni, which makes the process recipe specific to Ni in contrast to the above. However, if required it could presumably be converted to work with another catalyst material if a suitable etchant is available. A possible problem could be that of removing the encapsulation without harming the Ni particles. A comparably thick (300 nm) Al encapsulation must be deposited on a fairly thin ($\sim$ 5 nm) Ni pattern. One can speculate that Al and Ni could mix slightly in their interface region - either during Al deposition or during subsequent processes where the temperature is raised. Removal of the thick Al layer including a small extra etching time to ensure complete removal could then be expected to lead to some etching of the Ni pattern also. Insufficient etching would result in some remaining Al, which could affect the catalytic activity of the Ni.

4.1.2 Process Recipe Tests

In order to evaluate the proposed process recipes, a number of experimental investigations have been made. These should test critical points in each of the recipes in order to find a suited recipe for realizing the desired structure.

Electron Beam Lithography on Released Cantilevers

The challenge of performing EBL on released cantilevers is that of applying a layer of resist with a homogenous thickness. Equipment for spray coating was not available, and it was therefore decided to focus on spin coating. First, the entire cantilever and chip structure was fabricated including the release of the cantilevers[152]. Then, the resist was applied to the wafer by spin coating, the catalyst pattern was exposed (see step 31 in appendix B for details), and 5 nm Ni was deposited by thermal evaporation followed by a lift-off step. This final step turned out to be difficult. Significant amounts of Ni remained in particular near the rim of the cantilever as seen in fig. 4.4(a). This is presumably due to the inhomogeneous resist layer thickness. In the central part of the cantilever there is sufficient resist to facilitate a successful lift-off but near the edges the resist is thinner causing the lift-off to fail.

As seen in fig. 4.4(b) the EBL-defined catalyst pattern on the central part of the cantilever has generated the desired nanotube pattern, but the Ni, that remained near the cantilever edge, has caused some unwanted na-

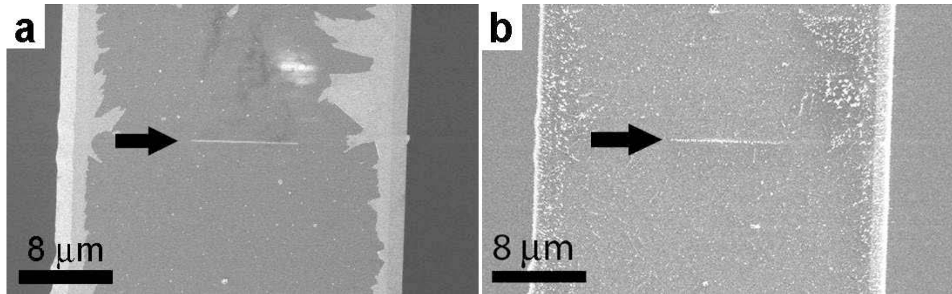

Figure 4.4: (a) SEM image of a cantilever after EBL, Ni deposition, and lift-off. The desired pattern is seen as the horizontal line indicated by the arrow. In addition, some unwanted Ni near the cantilever edge is seen where the lift-off was unsuccessful. (b) The same cantilever after nanotube growth[156]. Courtesy of Kjetil Gjerde and Lauge Gammelgaard.

notubes. Thus, the method of direct resist application by spin coating on released cantilevers can result in the desired structures but will also generate additional unwanted nanotube growth with the suggested process recipe.

In-situ Mask

Both the in-situ mask and the encapsulating layer process recipes were developed in a collaboration with Kjetil Gjerde who also conducted some of the experimental tests. The processing was performed as described in the previous section and only a short explanation will be provided here. The full recipes including all processing details can be found in the Ph.D. thesis of Kjetil Gjerde[155].

The initial tests of the in-situ mask strategy were carried out on a p-Si layer sputtered on top of a thermally grown silicon dioxide layer. This corresponds to fig. 4.2(a) excluding the electrodes. After resist deposition and EBL exposure and development, SF_6-based reactive ion etching (RIE) was used to transfer the pattern to the p-Si layer. Next, the cantilever pattern was defined by photolithography and transferred to the silicon dioxide layer by RIE. Before processing the backside, it is necessary to apply a protective layer to the frontside to ensure that it will not be destroyed in the KOH. This was done by plasma enhanced CVD of silicon nitride. Photolithography was used to define the chip pattern on the backside and RIE was used to etch through the layers on the backside. KOH was used to etch out the chips from the backside and release the cantilevers. Inspection under an optical microscope showed that a number of cantilevers appeared to have survived the KOH etching with the p-Si layer left unharmed as shown in fig. 4.5(a). However, on some cantilevers the KOH had penetrated to the p-Si once it had etched through as seen in fig. 4.5(b).

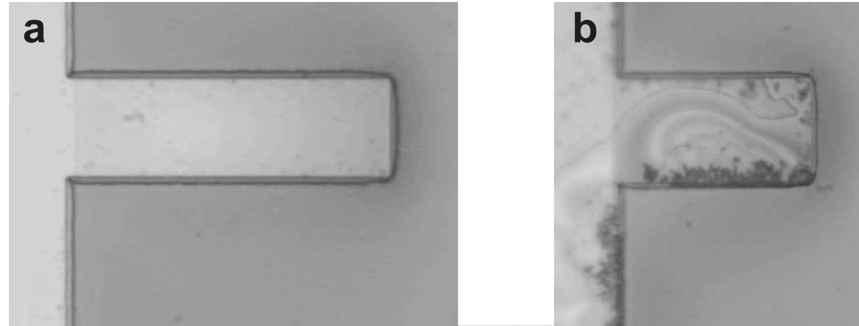

Figure 4.5: Optical microscope images of two different cantilevers after KOH etching from the backside. The silicon nitride frontside protection is still on. (a) Cantilever where the p-Si sacrificial layer is still present. (b) Cantilever where the p-Si sacrificial layer has been attacked by KOH.

As apparent from fig. 4.5, the KOH etching step will reduce the yield of functional chips. Following inspection, the silicon nitride protective layer is removed by etching in phosphoric acid. Here, a second problem was observed. It proved difficult to remove all of the silicon nitride even after prolonging the etching time significantly. To test the influence from this, 5 nm Ni was deposited and a lift-off step was made by etching the p-Si mask layer in KOH. The lift-off worked on some cantilevers resulting in the desired structure as seen in fig. 4.6.

However, in some cases the silicon nitride remains would hinder the lift-off. In these cases the cantilever surface was covered with some silicon nitride residues after lift-off that made the cantilever unusable. Another issue with this method is that Ni particles become larger than designed for. When the catalyst pattern is transferred to the p-Si layer by RIE, any isotropic etching will widen the holes. A further study[155] showed that this causes an increased size of $\sim$ 50 nm of the Ni particles.

The in-situ mask strategy is thus seen to be useful for obtaining a Ni catalyst pattern on a cantilever, although some of the processing steps causes a significant reduction in yield and the pattern features become larger than designed for.

Encapsulating Layer

The initial tests of the encapsulating layer process recipe were carried out by performing EBL on the silicon dioxide layer (i.e. again excluding the electrodes). After EBL exposure and development, 10 nm Ni was deposited and a lift-off step was made to fabricate the catalyst pattern. The pattern was inspected in SEM to confirm that it had the desired position and size. 300 nm of Al was deposited on top of the catalyst pattern to encapsulate

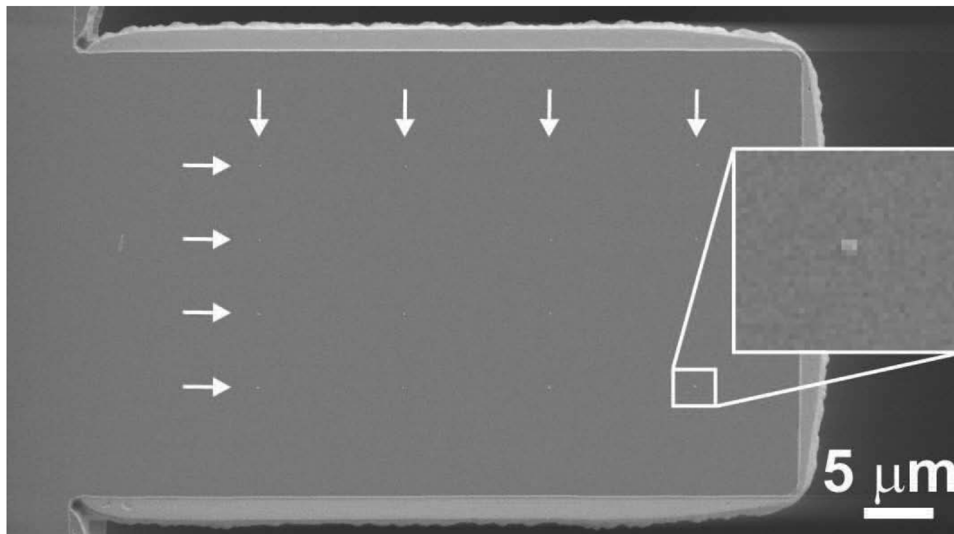

Figure 4.6: SEM image of a cantilever after Ni deposition and lift-off. An almost successful lift-off has produced 14 of the desired 16 Ni particles in a 4 by 4 test array (marked by the arrows).

it. This structure was used to test how well Al could be removed without causing damage to the Ni particles. In order to simulate the heat load caused by the later processing, the wafer was annealed at 300°C for 35 min. It was then etched in the Transene Aluminum Etchant, which removed the Al in $\sim$ 20 min. Afterwards, the Ni pattern was inspected with the SEM.

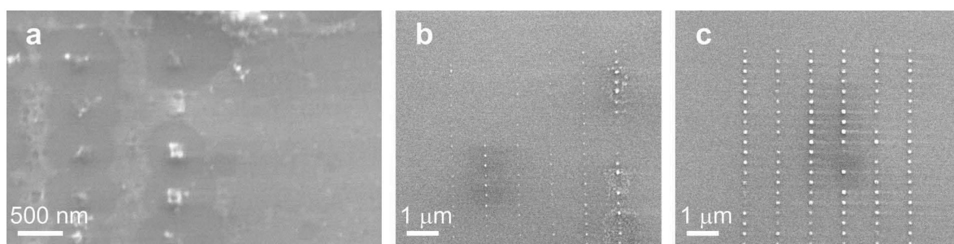

Figure 4.7: SEM images of the Ni pattern after removal of the Al layer. (a) The test array of Ni particles is still discernible but some particles are missing and the remaining appear significantly damaged. (b) Similar array at a lower magnification. (c) More successful catalyst array where almost all Ni particles are still present although some appear slightly damaged.

As seen in fig. 4.7, the Ni structures are still discernible although they in some cases appear rather damaged. A similar test was performed, however, with the Ni particles positioned on top of TiW to investigate how the intro-

duction of an electrode material would change the situation. In this case, all Ni particles were lost after Al removal presumably due to poor adhesion.

Unless the process of removing of the encapsulating layer is improved, the encapsulating layer strategy seems less promising. One possibility could be to deposit a thicker Ni layer and accept a partly removal during Al etching. However, this strategy would provide very little control over the resulting layer thickness, which eventually will influence the nanotube diameter.

4.1.3 Improving the Recipe

The experimental investigations showed that all three methods were to some extent useful although none of these gave the desired outcome with a high yield. The straight-forward method of spin coating EBL resist on released structures can produce the desired catalyst pattern. However, it is problematic to achieve a sufficient EBL resist layer thickness over the entire cantilever and this causes some catalyst deposition in unwanted regions. The in-situ mask also works in the present form, but the KOH etch and the problem of efficient etching of silicon nitride cause a rather low yield. The method of encapsulating the Ni particles also appears possible, but it is problematic to etch away the encapsulating Al layer without destroying the Ni pattern.

Window Mask

Based on the experimental tests, a new process recipe has been developed which combines some of the strengths of the initial recipes and avoids the problematic issues. The simplicity of the method of directly applying the EBL resist on the released cantilevers makes this the favored choice. This requires that the problem of the Ni remains near the cantilever edge is solved. A solution could be to introduce a sacrificial layer beneath the Ni. This sacrificial layer should be dissolved when the Ni lift-off process is made thereby removing any unwanted Ni near the cantilever edge. Based on the tests on the in-situ mask, p-Si appears to be a suitable choice for the sacrificial layer. By postponing the deposition of the p-Si layer until after the KOH etch has been made, the problem of the p-Si layer being attacked by KOH is avoided.

The first part of the process recipe is identical to the description presented in the section on EBL on a released cantilever, i.e. the entire microfabrication is made first resulting in released cantilevers with the appropriate electrode structure. Photo resist is then applied on the wafer by spin coating and a pattern is exposed that defines a set of ”windows”. These windows are situated over the areas where EBL is later performed. Next, p-Si is deposited and a lift-off process is made to produce the structure shown in fig. 4.8(a). Here, the entire chip and cantilever are covered in p-Si, except

for small windows located on the electrodes. An important point is that the p-Si is deposited by a vapor deposition method which is conformal. This avoids the coverage problems near the edges observed when applying a film onto released cantilevers by spin coating. Next, EBL is performed by applying the resist via spin coating, exposing the catalyst pattern, and depositing Ni. Finally, a lift-off step is made first with EBL resist remover and then KOH. Alternatively, lift-off can be made with KOH only as it will dissolve both the resist and the p-Si. Again the resist coverage near the cantilever edge will probably be poor but this should not cause problems since the p-Si layer will function as sacrificial layer in these areas. The resulting structure is seen in fig. 4.8(b). The entire process recipe can be found in appendix B.

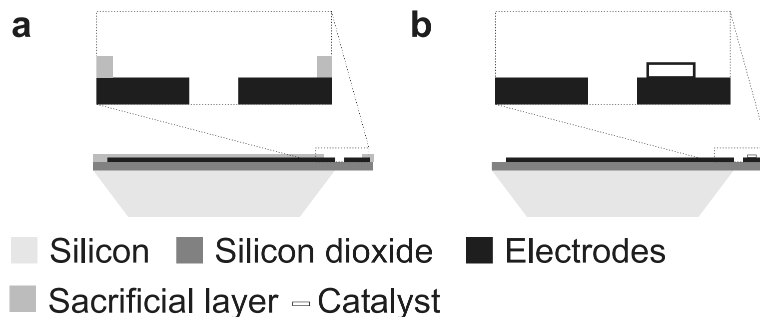

Figure 4.8: Cross-sectional drawings of a single cantilever chip made with the window mask recipe towards the end of the fabrication (excluding possible additional layers on the backside). The top figures are magnified views of the top of the electrode structure. (a) Using photolithography, the pattern for the windows in the sacrificial p-Si layer is defined. p-Si is deposited and a lift-off process is used to realize the windows in the p-Si layer. (b) EBL resist is applied by spin coating, exposure and development are made, and Ni is deposited. Making a lift-off step in KOH causes both the resist and the underlying p-Si layer to dissolve thus yielding the desired structure. Note that this is not drawn to scale.

To verify that the p-Si sacrificial layer could function as intended some experimental tests of the window mask process recipe were made by fabricating wafers with the developed recipe. To save processing time it was decided to skip the backside processing for this test (thus excluding steps 15-23 of app. B) since it could still show if the idea of using a p-Si sacrificial layer with a window for EBL definition of catalyst particles would work at all.

After fabricating the electrode and cantilever structures, a photolithography step was made to fabricate the pattern for the windows. p-Si was deposited by sputtering and lift-off was made. EBL resist was deposited by spin coating, the catalyst pattern was written, and the resist was developed.

Finally, 5 nm Ni was deposited and lifted off first in EBL resist remover and then in KOH. As seen in fig. 4.9(a) the chip and cantilever topside does not have any Ni remains. However, the Ni lift-off in the windows was not perfect and a continuous film was observed in some places. Fig. 4.9(b) shows a magnified view of the electrode gap.

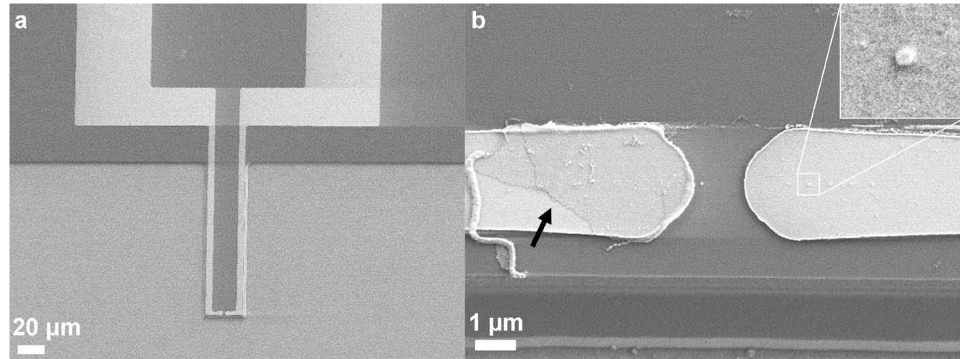

Figure 4.9: SEM images of the outcome of the window mask approach after EBL, Ni deposition, and lift-off. (a) The cantilever and electrode structures look as desired and no remaining Ni is seen on the chip. (b) The lift-off inside the window has not been perfect. Some Ni remains in parts of the window (indicated by the arrow) whereas other areas appear as desired.

Fig. 4.9(b) shows that some Ni particles have been realized at the desired position, however, some Ni also remains as a continuous film in some locations within the window area. This was not intended and a further analysis was made to determine the probable cause. Presumably the problem was caused at an earlier stage by a poor photolithography exposure of the window pattern. This caused the p-Si layer to bulge slightly up at the window edge and caused a remaining rim as also visible in the left part of fig. 4.9(b). Since the Ni film could later have adhered to this, it could have hindered the Ni lift-off. A work-around, later discovered by Kjetil Gjerde, consists of skipping the lift-off step in EBL resist remover and only use KOH to lift off both the EBL resist and p-Si at once.

A second problem concerning the Mo electrodes was also noted. Their adhesion to the underlying silicon dioxide substrate was insufficient and some were observed to have been dislodged. It is expected that an increased adhesion can be realized by depositing Mo through sputtering rather than thermal evaporation[157], however, this has not been tested. TiW, on the other hand, adheres strongly to silicon dioxide[158].

Even though the Ni lift-off was not 100 % successful these chips can still function as test substrates in the initial test and optimization procedures of the CVD set-up. In these experiments the purpose will be to establish

suitable processing parameters and the extraneous Ni is therefore of less significance.

4.2 Nanotube Growth

As described in chapter 2, carbon nanotubes can be grown by a chemical vapor deposition process. Apart from a suitable growth substrate with catalyst material, nanotube growth requires a CVD system for supplying an appropriate carbon feedstock gas and sufficient energy to dissociate the hydrocarbon molecules. Some initial growth tests were carried out in collaboration with the Milne group at the University of Cambridge. It was later decided to design and construct a nanotube CVD system in order to have easy and convenient access to a set-up that could be adapted to the present specific needs. The greater part of this system has been constructed by Kjetil Gjerde who built the vacuum and gas supply system, whereas this author primarily was involved in the design and fabrication of the heating system, the software for gas flow control and temperature read-out, as well as the electrical system that enables the application of an electric field to direct the nanotube growth. Here, the lay-out of the system will be introduced, followed by a description of its initial optimization and finally of the growth experiments aimed at growing individual nanotubes on electrodes.

When growing carbon nanostructures by CVD it can result in different morphologies depending on the process conditions. The graphene layers can stack in various ways which apart from the tubular form also include for example a herringbone structure[68]. Also, the density of defects can vary significantly. A general naming convention for such carbon filaments does not exist. For example, some authors use the word "nanofiber" to describe nanotube structures with a high degree of defects and reserve the word "nanotube" for only nearly-perfect tubular structures. Others use "nanotube" for all tubular structures regardless of the defect density. In this section, the resulting carbon structures will be designated "nanotubes", although it must be stressed that their internal structure is not known and that "nanofiber" could be more appropriate for some of the observed structures. Here, SEM has been used to inspect the results. A deeper insight into the internal structure would require transmission electron microscopy.

4.2.1 Construction of Chemical Vapor Deposition System

The constructed CVD system consists of a growth chamber with an attached vacuum pump to enable operation at low pressure. A heating system delivers the energy necessary to dissociate the carbon feedstock molecules for nanotube growth, while a gas supply system facilitates control of the necessary gas flows. Finally, an electrical system makes it possible to apply an electric field between two electrodes for electric field guided growth.

Vacuum system

The vacuum system consists of a growth chamber made in stainless steel with a glass lid for observation and sample transfer. It is connected to a rotary vane pump through a vacuum tube system which includes valves and a pressure gauge. The exhaust from the pump is led to an external ventilation system to avoid any residual gases escaping to the laboratory. Fig. 4.10 schematically shows the layout of the CVD system, which is also seen on the photograph in fig. 4.11(a).

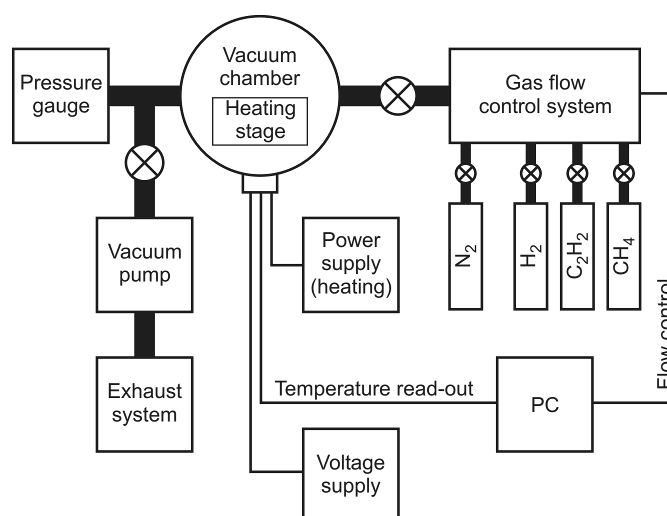

Figure 4.10: Schematic drawing of the CVD system for nanotube growth.

Gas supply system

Two different carbon feedstock gases are connected to the CVD system: acetylene (C_2H_2) and methane (CH_4). Only one will be used at a time but having access to both can allow for experiments on how the feedstock gas affects the growth and nanotube properties. In addition, another gas must be supplied to dilute the carbon gas and inhibit the formation of amorphous carbon. In this system, hydrogen (H_2) is used for this purpose. All three gases are connected through identical gas supply systems controlled by mass flow controllers (MFCs). The MFCs are controlled via a custom-made LabVIEW program that allows the user to set a desired flow rate and continuously monitor the actual, obtained flow rate. The final gas is nitrogen (N_2) which is used to flush the chamber and the other gas lines after use. Since the exact flow rate of nitrogen is not important, this is just controlled by a manual valve. The gas supply system is conceptually shown in fig. 4.10, whereas fig. 4.11(b) shows a photograph.

Heating system

Several designs of the heating system were constructed and tested. The optimum and thus implemented design is a 5 cm long by 4 cm wide by 2 cm high graphite block heated by two 400 W halogen light bulbs that are placed inside cavities in the graphite block. The power dissipated by the light bulbs is transferred to the graphite block, which then heats up. The bulbs are supplied from an external power supply that allows the input power and thereby the temperature to be adjusted. A thermocouple placed inside the graphite block close to its surface is used to monitor the temperature. At a pressure of a few mbar and heating with $\sim$ 600 W, the temperature reaches 900°C within a few minutes. Reaching even higher temperatures is presumably straight-forward since this only corresponds to only 3/4 of the full power, however, this has not been necessary for these growth experiments. Fig. 4.11(c) shows the graphite heating stage in the growth chamber with the sample holder for electrical contact placed on top.

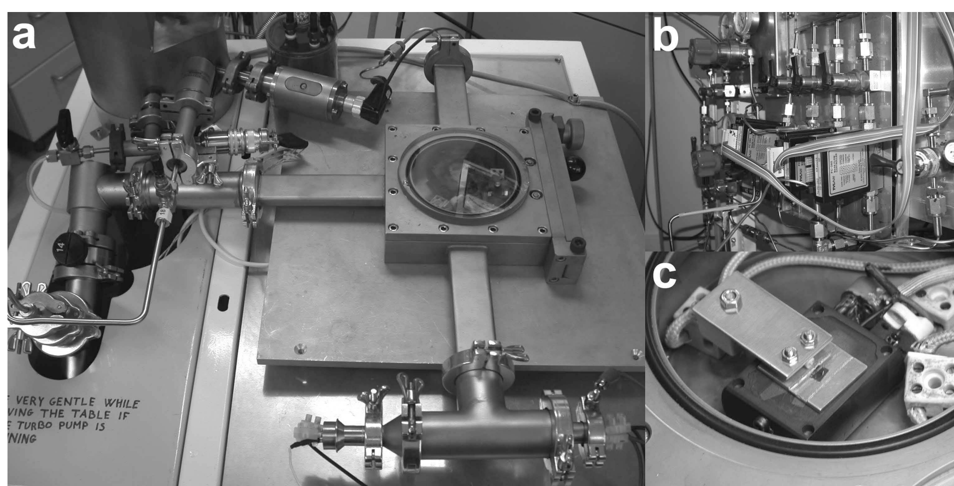

Figure 4.11: CVD system for nanotube growth. (a) The vacuum chamber with three connections: one for gas supply, one for the vacuum system, and one for the electrical feed-throughs. (b) The gas supply system. In front is seen the MFCs, while the knobs in the background are at the pressure reduction valves leading from the gas cylinders. (c) The system for applying an electric field is constructed from two W springs that clamp and connect to the sample, which is placed on a Cu holder. Here, the Cu holder is placed on the graphite block in the growth chamber.

Electrical system

A system for applying an electric field between the electrodes on the chip to guide the growth direction has also been constructed. It consists of two Cu plates: a base plate and a top plate. The sample is resting on the base plate. An electrically insulating aluminum oxide tube, sandwiched between the Cu plates, holds two W wires in position. These W wires connect electrically to the sample, clamp it to the base plate, and are connected to the outside through larger leads taken to an electrical feed-through. Fig. 4.11(c) shows a photograph of the system, where the end of the aluminum oxide tube carrying the W wires is visible between the two Cu plates.

4.2.2 Growth Process

A large span of processing conditions have been used for the growth of MWCNTs[68]. Some of the variable parameters are: type and structure of catalyst material, type and flow rate of both carbon feedstock gas and dilution gas, substrate temperature, pressure, and processing time. As described earlier, the catalyst consists of a Ni pattern defined by EBL. As carbon feedstock gas, acetylene was chosen, with hydrogen as the diluting gas, since acetylene is known to favor the growth of MWCNTs over SWCNTs[68]. The combination of acetylene and hydrogen has previously been used for the growth of MWCNT bridges[149].

Still, a rather large parameter space exists to explore by varying the acetylene/hydrogen flow, temperature, pressure and duration. In order to characterize the growth performance, three of these parameters are held fixed and the fourth is varied to study its influence. For these experiments, that are performed to establish suitable parameters for nanotube growth, it was decided to omit the electric field and focus on optimizing the morphology of the resulting structures. The temperature was fixed at a 'mid-range' value of 700°C similar to previous studies[149, 159]. Initial experiments indicated that a pressure of 25 mbar was suitable, so the pressure was fixed to this value. The growth duration mostly influences the nanotube length and should for the growth between electrodes thus be chosen in order to achieve a bridging structure. Here, it was arbitrarily set at 20 minutes. Several growth experiments were then performed, each with a total gas flow of 10 sccm but with different ratios between acetylene and hydrogen. The recipe used for the CVD growth is:

1. Place the sample on the heating stage and purge the chamber with nitrogen.

2. Apply 50 V to the heating stage. Slightly before the desired temperature (700°C) is reached, adjust the voltage to obtain a stable temperature.

3. Open the acetylene and hydrogen MFCs to the desired flow and regulate the pump line valve on the chamber until the desired pressure (25 mbar) is reached.

4. Manually regulate the temperature by adjusting the input power. The flow is regulated automatically through the LabVIEW program.

5. After 20 minutes, turn off the power to the heating stage, close the flow controllers and flush with nitrogen.

Following these first experiments, which were meant to establish a suitable set starting point, further trials were conducted with the best parameters found. These further experiments were performed on substrates where the Ni lift-off process had been more successful thus potentially allowing the growth of nanotubes from individual catalyst particles. Finally, growth experiments were carried out with an applied electric field between the electrodes. In these experiments, a voltage of 6 V was applied over a series connection of the electrodes and a 40 kΩ resistor[14]. The exact electrode separation distance varies between different substrates but is typically a few μm. This will cause an electric field strength of the order of a few V/μm, similar to what has previously been used to direct MWCNT growth[74].

4.2.3 Results and Discussion

The growth experiments were performed according to the recipe given above. For each subsequent experiment, the ratio between acetylene and hydrogen was changed starting at 3 % acetylene and increasing to a maximum of 17 %. The experiments were performed on substrates similar to the one shown in fig. 4.9. On these substrates the Ni lift-off had not been perfect and there were therefore some Ni remains inside the "window", however, the remaining substrate area appeared free of Ni. Fig. 4.12 shows SEM images of the resulting structures from five different experiments.

Several important observations can be made from fig. 4.12. The substrates used for these experiments had significant amounts of Ni left within the window. As expected this has caused the deposition of carbon over a larger area and not just at the intended positions. However, on the remaining part of the substrate almost no carbon deposits can be observed.

As the acetylene to hydrogen ratio is varied, a significant change is observed. At a low acetylene ratio of just 3 % the resulting carbon deposits appear in the form of a carbonaceous film. At higher acetylene ratios some elongated structures are formed. In particular at a acetylene content of 13 % (fig. 4.12(g-h)) the resulting nanotube-like structures, although curly, appear to have a well defined diameter both along the length of each individual nanotube and between different nanotubes.

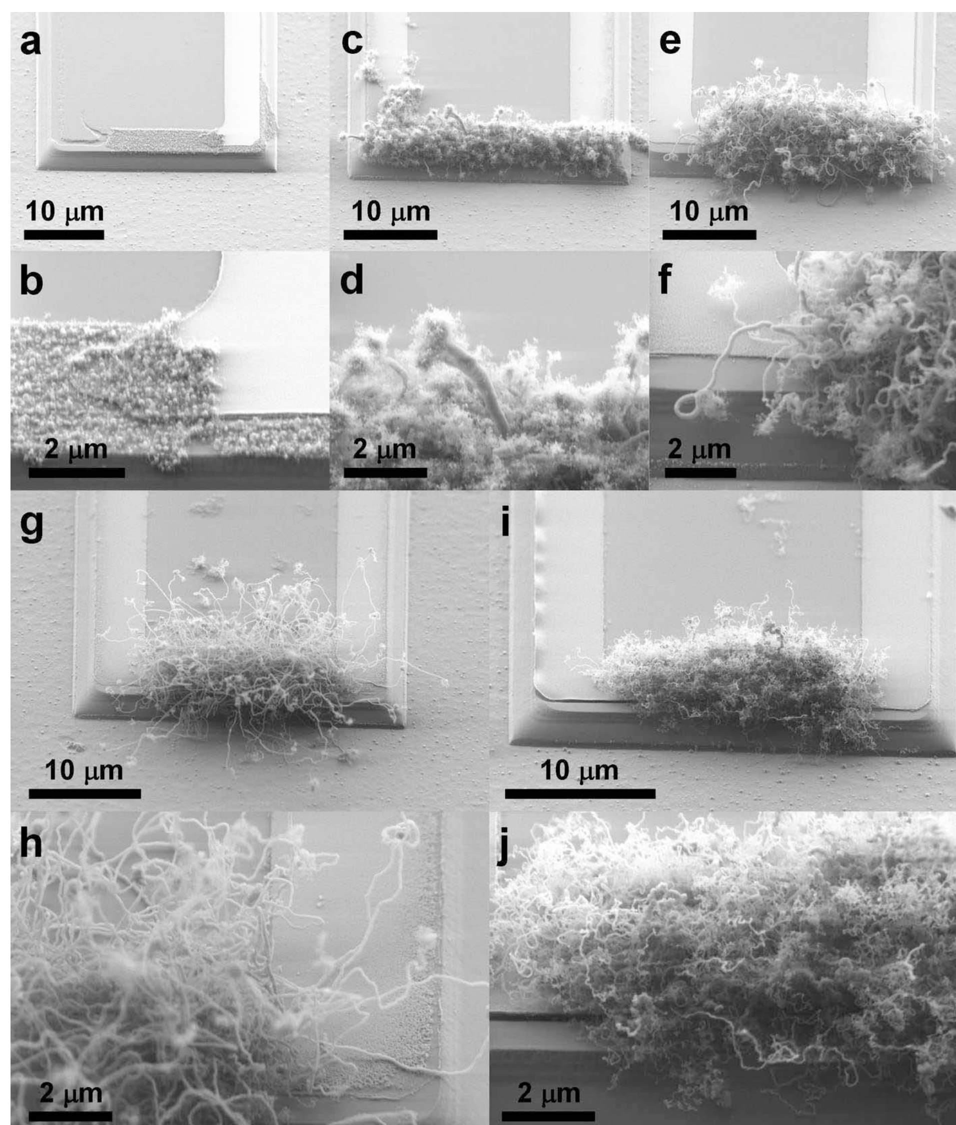

Figure 4.12: SEM images showing the outcome of different growth processes. (a-b) 3 % acetylene. (c-d) 6 % acetylene. (e-f) 10 % acetylene. (g-h) 13 % acetylene. (i-j) 17 % acetylene. The other growth parameters are given in the text. These SEM images have all been recorded with the substrate surface tilted to an angle of 45°.

A further observation is that in most experiments the end of the nanotube structures appear fluffy as if the catalyst particle has broken up into many smaller pieces, which each has catalyzed a continued growth. Similar observations have been reported previously[159], where it was attributed

to the sudden stop of the growth process. In the present experiments, the growth process is ended by opening the throttle valve completely to remove the remaining carbon feedstock. This causes a sudden drop in pressure and temperature that possibly could be responsible for the catalyst particle breaking up thus leading to the observed structures.

With the constructed CVD system and the aforementioned growth parameters it is thus possible to achieve growth of nanotube-like structures. After establishing these appropriate growth parameters, experiments with more a well-defined catalyst pattern were carried out to investigate the possibility of growing nanotubes from individual catalyst particles and of achieving field guided growth. However, it should be pointed out that a further investigation and optimization of the other growth parameters can presumably facilitate growth of nanotubes with a higher quality.

Using the established parameters, growth was attempted on substrates with more a well-defined catalyst pattern. Fig. 4.13(a) shows an example of such a substrate prior to nanotube growth. Here, the Ni catalyst particles have the desired form, although they are slightly misaligned. In addition some residue can be observed near the circumference of the electrode.

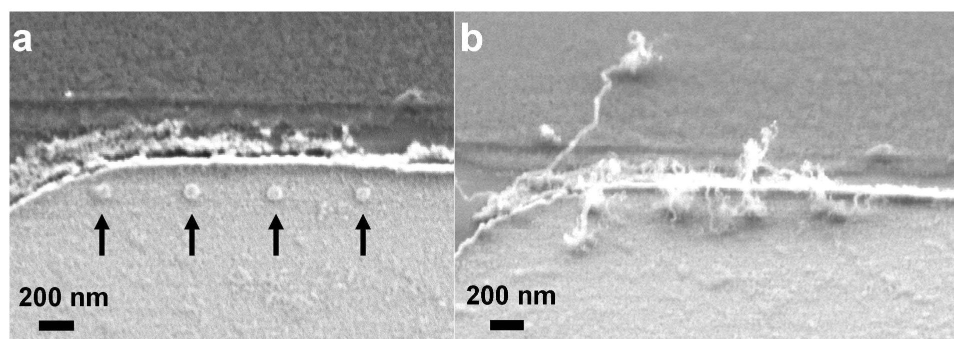

Figure 4.13: SEM images of the substrate with electrodes and Ni particles (marked by arrows) before (a) and after (b) CVD growth with the parameters described in the text. (b) has been recorded with the substrate surface tilted to an angle of 45°.

The result seen in fig. 4.13(b) shows that each of the catalyst particles has nucleated growth. Some elongated structures have been grown from some catalyst particles, however, with rather short lengths despite the processing time being the same as in the optimization runs. Also, some smaller feather-like structures can be observed. It is not clear what caused the rather short length, however, the results do demonstrate the ability to achieve growth from individual catalyst particles.

The final experiments were made to test the possibility of guiding the nanotube growth direction by applying an electric field. In these experiments, a

single chip was mounted in the holder and connected to the external voltage supply. After heating to the desired temperature, the MFCs were opened, the pressure was adjusted, and a voltage of 6 V was applied between the electrodes. After growth, the chips were inspected in SEM. Fig. 4.14 shows one of the resulting chips.

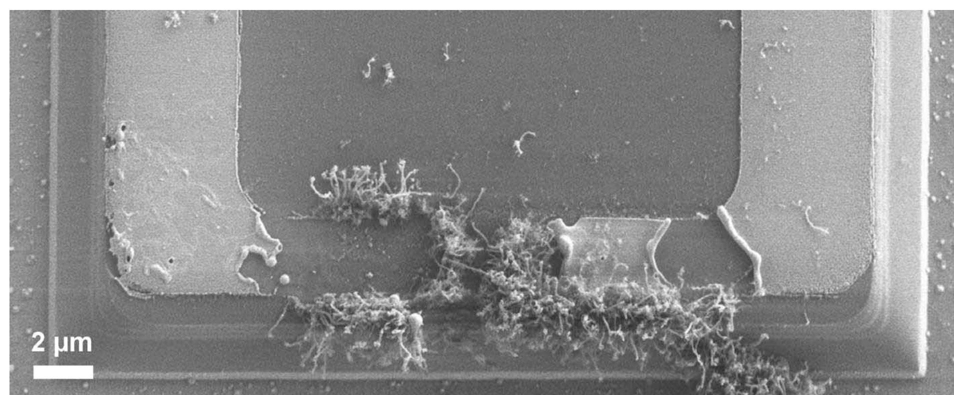

Figure 4.14: SEM image showing the outcome of a growth process where an electric field had been applied.

As fig. 4.14 demonstrates the electrodes in all cases were destroyed, presumably due to an electrical discharge. This could be caused by external electrical disturbances picked up by the connecting W wires. However, even after connecting both W wires to ground during chip mounting and trying to minimize the susceptibility to external disturbances, the problem persisted. This suggests that the present system for applying an electric field needs optimization to circumvent this problem. As the first batch of chips did not have a high yield, the number of useful chips was unfortunately quite limited. A further study of this problem could well be done on a simpler test structure.

4.3 Summary and Outlook

In-situ growth of carbon nanotubes requires the design and fabrication of a suitable microsystem with catalyst particles of appropriate size and position. One difficulty is posed by the Ni catalyst, which can potentially contaminate some of the processing equipment required for the microsystem fabrication leading to unwanted contamination of wafers processed at later times. This problem can be solved in two ways: either by postponing Ni deposition until all microfabrication has finished, or by depositing Ni at an early stage and encapsulate it to prevent contamination.

Due to the different length scales involved, the use of two different litho-

graphy techniques is preferable. Conventional photolithography can create the microscale pattern of the microsystem, while a nanoscale lithography technique such as EBL is necessary for defining the sub-100 nm catalyst pattern. Three different process recipes, which use both these techniques and which avoid the Ni contamination problem, were developed and tested in collaboration with Kjetil Gjerde. All three were to some extent functional, however, some problematic issues were observed during the experimental investigations. Based on these observations, a new process recipe was suggested and additional fabrication tests were made. The fabrication of a suitable microsystem within the given process limitations appears possible, however, additional optimization is required to fabricate the desired microsystems with a high yield.

The second requirement for carbon nanotube in-situ growth is a CVD system. Such a system, consisting of a vacuum chamber, a gas supply system, and a heating stage, was constructed and tested. A number of optimization experiments were performed to find appropriate processing conditions. Under these conditions, some elongated carbon structures resembling nanotubes were formed. SEM imaging showed that these nanostructures are quite straight and have a uniform diameter, however, they exhibit some kinks that must indicate a rather defective internal structure. Further insight in this could be obtained by the use of a microscope technique with a higher resolution such as for example TEM.

Initial tests of individual nanotube growth from EBL defined catalyst particles were partly successful, although the resulting structures did not have precisely the desired morphology. The experiments made in an attempt to guide the growth direction by an applied electric field were not successful, as difficulties with electrical discharge caused the destruction of the electrode structure. To realize in-situ growth requires a solution to this problem, which would involve an optimization of the system for applying the necessary electric field.

Chapter 5

Cantilever Sensor with Carbon Nanotube Piezoresistor?

Microcantilevers have important applications in several fields. One of the most significant is within atomic force microscopy (AFM), where the deflection of a cantilever is used to map out the topography of a surface[160]. A second important area is chemical[161] and biochemical[162] sensing, where stress induced in a chemically functionalized cantilever by molecular binding causes a static bending, and mass sensing, where a small adsorbed mass changes the dynamic properties of a resonating cantilever[163]. Also, microcantilever tools can be used for manipulation of micro- and nanostructures as described in Chapter 3. Advanced microcantilever tools can provide a force-feedback signal that can be used to measure the forces applied to the object[124]. This also requires that the cantilever deflection can be read out.

Different schemes of read-out of cantilever deflection have been realized, depending on the application. Both for AFM[164] and chemical/biochemical sensing[161, 162], an optical detection scheme is often used, in which laser light is reflected from the backside of the cantilever. The cantilever deflection is read out by projecting the reflected light onto a position sensitive photo detector. This technique is widely employed due to its high sensitivity. In situations where a laser detection setup is impractical, schemes such as piezoresistive read-out are preferred. Here, a piezoresistor is integrated in the cantilever[165]. When the cantilever is deflected, the piezoresistor is stretched, which can be read out for example through a Wheatstone bridge arrangement[146]. This scheme is beneficial for AFM or sensing in liquid where optical methods are less suitable. Also in the case of the advanced manipulation tools, where the cantilever deflection can be used to measure the magnitude of the applied forces, piezoresistive read-out is preferred since the tools are being moved during use impeding optical detection.

Typically, piezoresistors can be fabricated in doped Si by conventional microfabrication techniques[165]. However, more compact and sensitive sensors based on carbon nanotube strain gauges have been suggested[64]. Whether or not this is feasible depends on several aspects such as the possibility for efficient integration and on the performance. This chapter will try to answer the question whether MWCNTs can be used as an alternative to Si piezoresistors in a compact cantilever force sensor by comparing the two. First, the theory of piezoresistive cantilever sensors is briefly reviewed. This is followed by a section on the fabrication aspects of both Si and CNT based piezoresistive sensors. Next, the performance of the two types of sensors will be compared on different parameters such as sensitivity and noise, based both on theoretical considerations and experimental investigations. Finally, the prospect of an using a MWCNT in a cantilever sensor is discussed.

5.1 Theory of Piezoresistive Cantilever Sensors

The basic theory for describing a cantilever is continuum solid mechanics (CM), which allows the mechanical response of simple cantilever geometries to be found. This is particularly valuable in design situations where the influence of the different parameters such as cantilever dimensions is easily determined. However, for more complex geometries such calculations become too complicated and numerical methods such as the finite element method must be used. Here, a simple geometry is used to derive design equations, and a more complicated design is investigated through finite element analysis.

Applying a point force F to the free end of a cantilever of length L as shown in fig. 5.1 will cause a bending moment M given by

$$M(x) = -F(L - x). \tag{5.1}$$

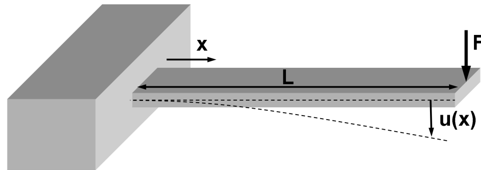

Figure 5.1: Cantilever with applied force F. Dashed line is the neutral axis.

This causes the cantilever to bend with a radius of curvature inversely proportional to the bending moment. Assuming small deflections the radius

of curvature $\rho(x)$ can be related to the deflection $u(x)$ through

$$\frac{1}{\rho(x)} \simeq \frac{d^2u}{dx^2}, \tag{5.2}$$

which leads to the following differential equation governing the deflection[141]

$$\frac{d^2u}{dx^2} = -\frac{M}{EI}. \tag{5.3}$$

E is Young's modulus and I is the plane moment of inertia of the cantilever cross section. For a rectangular cantilever: $I = wh^3/12$ where w and h are the cantilever width and height, respectively. Inserting eq. 5.1 in 5.3 and using the boundary conditions at the clamped end where both the deflection u and slope u' must equal zero, the deflection as a function of x can be determined. The maximum deflection occurs at the free end of the cantilever

$$u(L) = \left(\frac{L^3}{3EI}\right)F \tag{5.4}$$

and thus the cantilever has a spring constant $k = 3EI/L^3$.

The dashed line in fig. 5.1 is the neutral axis whose length remains unchanged during bending. The part of the cantilever below this line is compressed whereas the part above experiences a tensile stress. The longitudinal strain scales with the distance z from the neutral axis and is therefore maximum at the cantilever surface. The strain $\epsilon(x)$ of the surface of a homogenous cantilever is[141]

$$\epsilon(x) = -\frac{z}{\rho(x)} = \frac{h}{2\rho(x)}. \tag{5.5}$$

The maximum strain occurs where the inverse radius of curvature is maximum. This is at the support (i.e. at $x = 0$) where the strain becomes

$$\epsilon = \frac{hL}{2EI}F. \tag{5.6}$$

A thin (piezo-)resistor, positioned and fastened on top of the cantilever, will experience the same strain. This will change its resistance, which at small values of strain can be assumed to scale with strain as quantified through the gauge factor g

$$\frac{\Delta R}{R} = g\epsilon \tag{5.7}$$

where $\Delta R/R$ is the relative change of resistance. In order to determine the resistance change due to cantilever bending, the average strain along the length of the piezoresistor should be used. This is typically the case for a Si piezoresistor. If a short piezoresistor positioned at or near the clamped

end of the cantilever is considered, as the case when using a MWCNT, the approximate strain can be estimated from eq. 5.6 which can then give the force sensitivity

$$\frac{\Delta R}{R}\frac{1}{F} = g\frac{hL}{2EI} = g\frac{6L}{Ewh^2}. \tag{5.8}$$

Through eq. 5.4 the deflection sensitivity can be found as

$$\frac{\Delta R}{R}\frac{1}{u(L)} = g\frac{hL}{2EI}\frac{3EI}{L^3} = g\frac{3h}{2L^2}. \tag{5.9}$$

If the gauge factor of the piezoresistor is known, it is now possible to design for a particular sensitivity. In the work by Thaysen *et al.*[146] an AFM cantilever with integrated Si piezoresistor was designed, fabricated, and characterized. Here, a similar cantilever structure is used to investigate individual MWCNTs by integrating and using these as the piezoresistors to compare to the Si piezoresistor device. The MWCNT integration is performed with the shadow mask method described in chapter 3. This requires a slightly more complicated cantilever geometry in order to be able to monitor the MWCNT resistance. A conceptual drawing of a suitable cantilever geometry is shown in fig. 5.2.

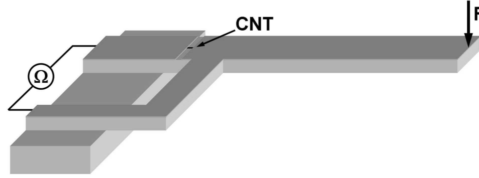

Figure 5.2: Conceptual drawing of cantilever with integrated carbon nanotube.

The extra electrode support structure will change the mechanical properties of the cantilever compared to the simple case i.e. increase the spring constant. In order to estimate the impact of this, the mechanical properties of a cantilever structure including the extra electrode support were investigated with the CoventorWare© software. The meander structure seen in fig. 5.3(a) is used for the extra electrode support structure in order to minimize its mechanical influence. The white lines in fig. 5.3(a) represent the mesh used for the finite element analysis.

Upon defining the appropriate boundary conditions and applying a force to the free end of the cantilever, the mechanical response can be found. Fig. 5.3(b) shows the result of a simulation where a force of 1 μN is applied. The color coding represents the stress where blue corresponds to 0 and red to 136 MPa. By applying different values of force it is possible to compare to the predictions of eq. 5.4 and 5.6 that describe the simple cantilever without the extra electrode support structure, see fig. 5.4.

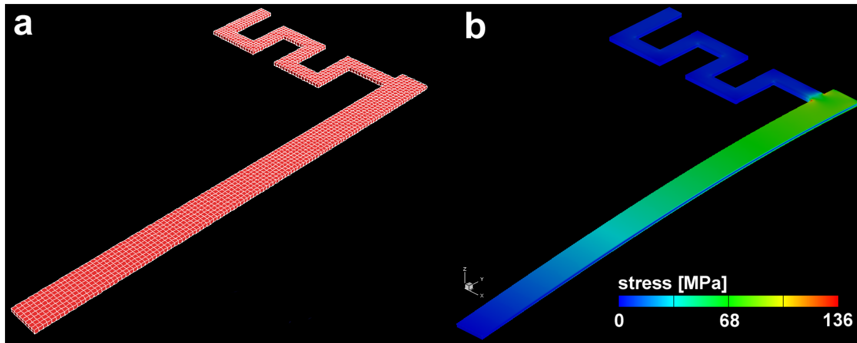

Figure 5.3: (a) 3-D model of a cantilever structure constructed in the CoventorWare© software. The silicon dioxide cantilever has a length of 120 μm, a width of 8 μm, and a height of 1 μm. (b) The mechanical response upon application of a force of 1 μN to the cantilever tip.

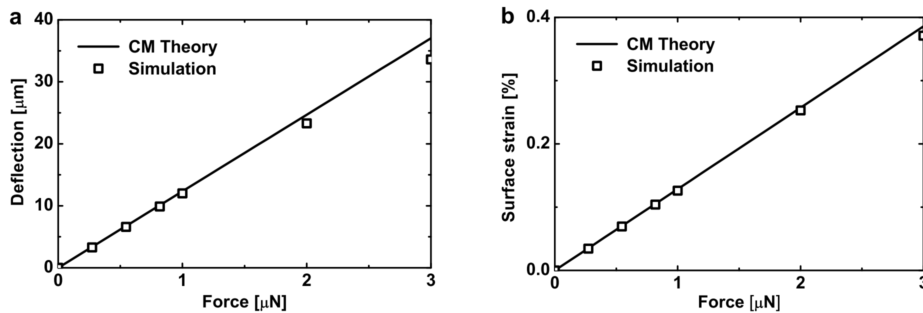

Figure 5.4: (a) Deflection versus applied force. (b) Surface strain at the clamping point ($x = 0$) versus applied force.

At low force values the simulated deflection values agree very well with the theoretical. Above 2 μN a deviation is observed. This corresponds to a deflection of $\sim$ 25 μm or one fifth the cantilever length and the assumption of small deflections used in the derivation of eq. 5.4 is no longer fulfilled. Thus, a deviation from the theoretical values must be anticipated. The cantilever surface strain at the clamping point corresponds well to the value predicted from eq. 5.6 even at an applied force of several μN. In conclusion, the continuum model describing the simple cantilever is suitable for the more complicated cantilever structure for low and moderate values of force.

5.2 Fabrication and Integration

The fabrication of cantilevers with integrated Si piezoresistors is often done by conventional microfabrication techniques. In contrast, a cantilever structure with an integrated carbon nanotube must be made in two separate processes: first the cantilever structure must be fabricated, and second the nanotube must be integrated using another technique such as those discussed in chapters 3 and 4. In this section the fabrication of cantilevers with integrated Si piezoresistors by Thaysen and co-workers[146, 166] is briefly reviewed. This part is followed by a more in-depth description of the realization of a cantilever structure for nanotube integration and a discussion of several important issues related to nanotube integration.

5.2.1 Integration of Si Piezoresistors by Microfabrication

Cantilever sensors with integrated Si piezoresistors can be fabricated from a silicon-on-insulator wafer. Here, a buried etch-stop layer, integrated in the device layer facing the oxide, is used to define the piezoresistor thickness. UV photolithography and different etch processes are used to define the piezoresistors, followed by implantation of a controlled amount of boron in the resistors to control their doping level. Next, the cantilever structure is defined by RIE and the electrical wiring to the resistors is realized by metal deposition. Finally, the cantilevers are released by KOH backside etching. Fig. 5.5 shows an optical microscope image of a finished cantilever chip.

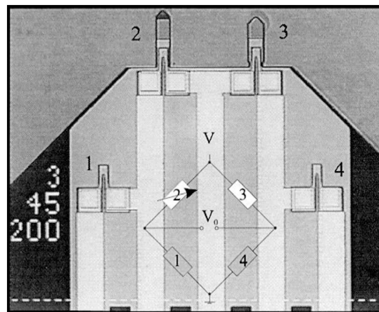

Figure 5.5: Optical microscope image of the AFM cantilever chip. Reproduced from [146]. The design includes a reference cantilever and an integrated Wheatstone bridge to minimize vibrational noise.

The design shown in fig. 5.5 incorporates two cantilevers: the left cantilever is the actual measurement probe, whereas the right cantilever is used as a reference probe to balance out noise and drift in the signal V_0. Two additional resistors are placed on the chip, marked 1 and 4 in fig. 5.5. Together with the two cantilever piezoresistors they make up a symmetrical Wheat-

stone bridge that increases the sensitivity of the device. The resistance of each resistor is approximately 6 kΩ and the resistors values typical vary 0.2 % within one Wheatstone bridge[146].

5.2.2 Fabrication of Cantilevers and Integration of CNTs

The proposed cantilever structure in fig. 5.3 was fabricated by conventional microfabrication techniques. The process recipe is based on one developed for micro four-point probes by C. L. Petersen[167] and T. M. Hansen[152], and only a brief review is given here.

A new photolithography mask, that incorporates different cantilever structures, some of them including the meander structure shown in fig. 5.3, has been designed. The silicon dioxide structures end up in large contact pads on the chip body to facilitate wire bonding after metallization. In addition there are some extra structures to ease placement of the silicon wire shadow mask and some further electrode support structures to test the possibility of making multi-point measurements. The processing is performed as described in fig. 5.6.

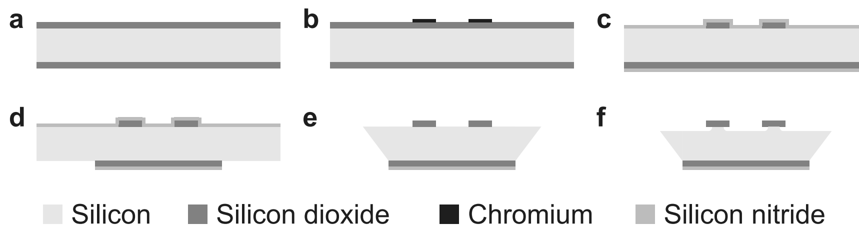

Figure 5.6: Schematic drawings of the cross section of a single cantilever chip at various stages during fabrication seen from the end. (a) A 1 μm thick silicon dioxide layer is grown on both sides of a double-polished Si(100) wafer. The cantilever structure will later be realized in this layer. (b) By a negative photolithography step, e-beam evaporation, and lift-off a chromium etch mask is made to pattern the cantilever and the electrode support structures. (c) After transferring the cantilever pattern to the silicon dioxide layer by a fluorine based RIE step, a conformal, low-stress silicon nitride layer is deposited by low-pressure CVD. This layer protects the frontside of the wafer during the etch releasing the cantilever. (d) A second photolithography step defines the chip outline on the wafer backside and the pattern is transferred first to the silicon nitride by RIE and second to the silicon dioxide layer by etching in buffered hydrofluoric acid. (e) The chips are etched out by KOH which releases the cantilevers. The silicon nitride layer is then removed by RIE. (f) A final shallow, isotropic RIE step in silicon undercuts the cantilever structures. This ensures that no short circuits to the chip surface are formed when metal electrodes are deposited at a later step.

Both during and after fabrication, the chips are inspected by optical microscopy and SEM. Fig. 5.7 shows SEM images of the final chip.

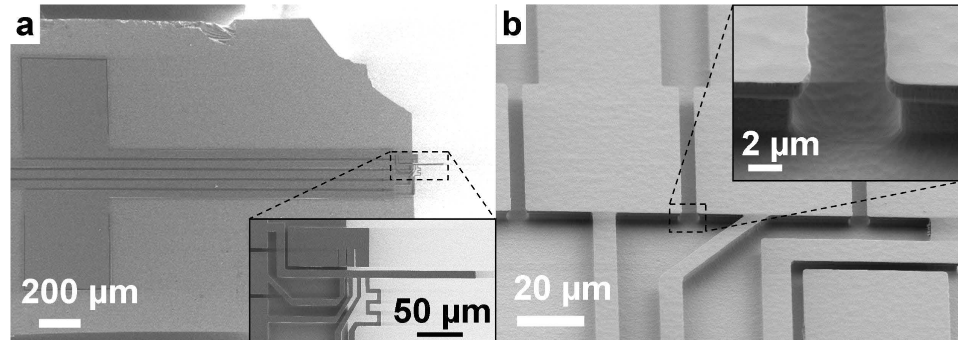

Figure 5.7: SEM images of a finished cantilever chip. (a) Silicon chip with silicon dioxide cantilever structure including electrode supports that end up in bonding pads. Inset shows close-up of the cantilever extending from the chip edge. (b) Electrode supports seen at an angle of 45° with respect to the surface. Inset shows close-up of the undercut beneath the silicon dioxide.

After processing and inspection, individual chips are released from the wafer and glued to a carrier substrate for easier handling and interfacing with measurement electronics. Next, the integration of nanotubes is performed using the shadow mask method described in chapter 3, and after the final metal deposition, the device is wire bonded to metal electrodes on the carrier substrate and is ready for test.

Two different MWCNT samples were used, fabricated a) by CVD and b) by arc-discharge as described in chapter 2. Both types of nanotube samples exhibit similar diameters of some tens of nanometers typically around 50 nm. The CVD grown MWCNTs contain many defects as evident from the TEM image in fig. 5.8. This will presumably influence the nanotube properties and cause a deviation from theory that is based on a 'perfect' structure. The MWCNTs produced with the arc-discharge method are presumed to have a lower defect density.

The metallic layer, which partially covers the nanotube, must fulfill two requirements: 1) it must provide good electrical contact to the nanotube, and 2) it must mechanically clamp the nanotube to the surface so that it does not slide during cantilever bending which is critical due to the inertness and smoothness of the nanotube[168].

A possible contact resistance will occur as a series resistance with the intrinsic nanotube resistance as described by eq. 2.5. In order to achieve a high sensitivity it is important to minimize this contact resistance. One option is to use four-point measurements to eliminate the contact resistance as demonstrated by Bourlon and co-workers[60] who used electron beam lithography

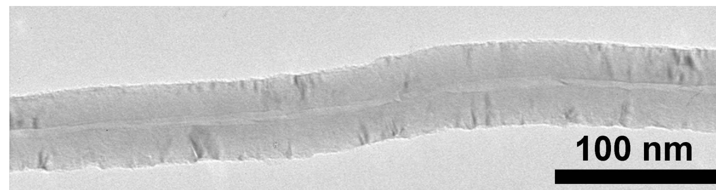

Figure 5.8: TEM image of a CVD grown MWCNT from the sample used in this study. The MWCNT is not structurally perfect, however, the shell structure can be observed. Courtesy of Kristian Mølhave.

to produce closely spaced electrodes on a single MWCNT. This scheme is problematic to realize on a cantilever with the shadow mask method. It requires the accurate placement of three silicon wire shadow masks close to each other to create the four electrodes. This has been attempted but proved to be very difficult. This problem is caused by the adhesive surface forces. Positioning the first wire is relatively straight-forward. But if the second mask should happen to touch the first wire briefly during positioning (which is almost unavoidable if they are to be closely spaced) the two wires will stick to each other, and the first will be displaced.

An alternative method is two-point measurements with low-resistance ohmic contacts. The first electrical transport measurements, where the nanotubes were dispersed on top of prefabricated Pt electrodes, showed large tunnel barriers at the contacts[6]. It was later shown that ohmic contacts to SWCNTs could be realized by evaporating 15 nm Ti followed by 60 nm Au on top of the nanotubes[169]. Alternatively SWCNTs were dispersed on prefabricated Au electrodes followed by a quick annealing[54] to provide a low contact resistance. For MWCNTs a low contact resistance of the order of just a few kΩ has been realized both with Au bottom contacts [170], where the device was annealed shortly after nanotube deposition and with Au top contacts fabricated by evaporation[171]. Another study compared the contact formed between MWCNTs and either Ti or Pt/Au electrodes[172]. This found that Ti contacted MWCNTs exhibited a significantly higher resistance than those contacted with Pt/Au.

During this project a total of 104 MWCNT devices were fabricated using the shadow mask method and electrically characterized. 26 of these devices had a low-bias resistance between a few and some tens of kΩ which was interpreted as current flow through the MWCNT with a low contact resistance. Fig. 5.9(a) shows typical low-bias current-voltage characteristics of a MWCNT contacted with Ti/Au electrodes. The average initial resistance of the 26 devices was 23 kΩ with the distribution shown in fig. 5.9(b). This corresponds quite well to previously reported values of MWCNT resistance[172].

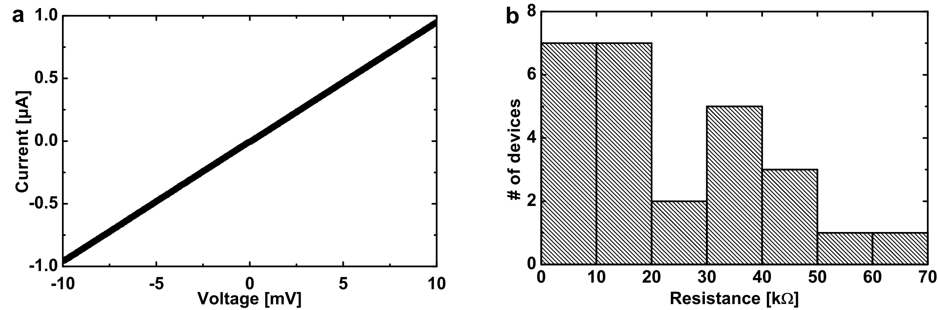

Figure 5.9: (a) Low-bias current-voltage characteristics of a MWCNT with Ti/Au contacts. (b) Histogram of the measured values of resistance.

Only one fourth of the fabricated devices showed a resistance that could be interpreted as current flow through the nanotube with a low contact resistance. Occasionally a high resistance of several 100 kΩ or even MΩ was observed. This was typically accompanied by a non-linear current-voltage relationship and is attributed to poor electrical contacts. Several other devices were lost due to problems with the shadow mask as discussed in chapter 3. In particular with the nanotubes, quite a few were lost due to an electric discharge through the nanotube which caused it to burn away. Other devices displayed open-circuit characteristics despite their visual appearance suggesting otherwise.

Different contact metal combinations were tested: Ti, Au, and Ti/Au. With Ti contacts it proved difficult to obtain a low contact resistance. Au contacts provide a low contact resistance, but its properties made it less suitable for the present application: When the cantilever was deflected the metal layer would sometimes peel off. A sandwich structure consisting of a thin layer of Ti followed by a thicker Au layer turned out to be the best choice. No systematic investigation of optimum layer thickness was performed, but a general observation is that the higher mechanical rigidity of a thicker metal layer is beneficial for clamping the nanotube. However, a maximum layer thickness exists beyond which the removal of the shadow mask is hindered.

5.3 Performance Comparison

Crucial for the estimation of the possibility of using MWCNTs as compact piezoresistors is how they perform in comparison with conventional components. In this section a comparison of two areas is made: sensitivity and noise.

5.3.1 Sensitivity

The intrinsic sensitivity of a piezoresistive material can be quantified through its gauge factor g (see eq. 5.7). For Si, the gauge factor depends on both crystal direction and doping level. The crystalline Si resistors fabricated by Thaysen in ref.[146] have a theoretical gauge factor of 120. However, experiments show a gauge factor of 50. The difference is attributed to Si lattice damage caused during processing. In the same work, polycrystalline Si resistors were experimentally shown to have a gauge factor of 20.

Theoretical gauge factor lowering in MWCNTs

The theoretical investigations of the strain response of carbon nanotubes have focused on SWCNTs and in particular on the change of the electronic bandgap. Experimental evidence suggests that when a MWCNT is stretched, the mechanical load is carried mainly by the outermost shell[173, 63]. This indicates that a possible change in electronic bandgap will occur only in the outermost shell whereas the remaining shells will retain their electronic properties. In a MWCNT, the majority of the current is carried by the outermost shell[60]. However, since a fraction of the current enters the deeper-lying shells also, this will alter the electromechanical response when compared to the simpler case of just one current-carrying shell.

As described in chapter 2, the transport mechanism in a MWCNT is assumed to be diffusive rather than ballistic thus the intrinsic resistance is dependent on length. In the simple case, where it is assumed that the current flows in the outermost shell only, the resistance R may then be expressed by a resistivity ρ_1 of the outermost shell through $R = \rho_1 l$ where l is the nanotube length. This corresponds to the assumption of zero intershell conductance. It is now possible to find an expression for the gauge factor $g = (1/R)(dR/d\epsilon)$ in the single shell case

$$
\begin{aligned}
g_{ss} &= \frac{1}{R}\left(\frac{dR}{d\rho_1}\frac{d\rho_1}{d\epsilon} + \frac{dR}{dl}\frac{dl}{d\epsilon}\right) \\
&= \frac{1}{R}\left(\frac{dR}{d\rho_1}\frac{d\rho_1}{dE_g}\frac{dE_g}{d\epsilon} + \rho_1 l\right) \\
&= \frac{1}{R}\frac{dR}{d\rho_1}\frac{d\rho_1}{dE_g}\frac{dE_g}{d\epsilon} + 1 \\
&\simeq \frac{1}{\rho_1}\frac{d\rho_1}{dE_g}\frac{dE_g}{d\epsilon},
\end{aligned} \tag{5.10}
$$

where in the last line it is assumed that the influence from the electronic bandgap change on the resistivity is the most significant contributor to the gauge factor. When an intershell conductance different from zero is introduced, the gauge factor will be different. Here, the model by Bourlon *et*

al.[60] introduced in chapter 2 and shown in fig. 2.5(b) is used to describe the situation. The four-point resistance R_{4P} in this model is

$$R_{4P} = \sigma\rho_1 L_a^3 \left(\frac{\rho_2 l}{L_a} + 2\rho_1 \sinh\left(\frac{l}{2L_a}\right) \exp\left(\frac{-L}{2L_a}\right) \right), \tag{5.11}$$

where $\sigma\delta x$ is the intershell conductance over a length δx, while $\rho_1\delta x$ and $\rho_2\delta x$ are the intrashell resistances of shell 1 and 2, respectively (see fig. 2.5(b)). L_a is a characteristic length, over which the current enters the deeper-lying shells, given by $L_a^{-1} = \sqrt{\sigma(\rho_1 + \rho_2)}$. l and L are the separations of the voltage probes and the current probes, respectively. In a two-point configuration $l = L$. Thus, the two-point resistance R_{2P} can be found by simplifying eq. 5.11 (and neglecting the contact resistance)

$$R_{2P} = \sigma\rho_1 L_a^3 \left(\frac{\rho_2 l}{L_a} + \rho_1 \left(1 - \exp\left(\frac{-l}{L_a}\right)\right) \right). \tag{5.12}$$

When the MWCNT is stretched the resistivity and thus the intrashell resistance of shell 1 will change i.e. $\rho_1 = \rho_1(\epsilon)$. One can speculate that the intershell conductance σ could be affected also. Theoretical studies show that the intershell conductance between two telescoping nanotube shells can show a periodic behavior as a function of overlap length[174], however, only in the case of either armchair/armchair or zig-zag/zig-zag configurations. Other combinations show significantly smaller intershell conductance and no periodic behavior is reported. Since the geometric structure of neighboring shells in a MWCNTs in general are independent, it will here be assumed that σ remains constant during stretching. Also, since deeper-lying shells are not affected by stretching, ρ_2 will remain constant. Thus, the resistance depends on several variables: $R = R(\rho_1, \rho_2, \sigma, l)$ given by eq. 5.12. The gauge factor, when the current is carried by multiple shells, g_{ms} can be determined from

$$\begin{aligned} g_{ms} &= \frac{1}{R_{2P}} \frac{dR_{2P}}{d\rho_1} \frac{d\rho_1}{dE_g} \frac{dE_g}{d\epsilon} + 1 \\ &\simeq \frac{1}{R_{2P}} \frac{dR_{2P}}{d\rho_1} \frac{d\rho_1}{dE_g} \frac{dE_g}{d\epsilon}. \end{aligned} \tag{5.13}$$

By comparing eq. 5.10 and 5.13 it is seen that

$$g_{ms} = \frac{\rho_1}{R_{2P}} \frac{dR_{2P}}{d\rho_1} g_{ss} = g_{rel} g_{ss}, \tag{5.14}$$

where g_{rel} can be used to examine the influence from the deeper-lying shells. The factor g_{rel} is less than one since some of the current flows in the deeper-lying shells, which are unaffected by the stretching. Therefore, the overall gauge factor for the MWCNT will be smaller than the estimate from the change of electronic bandgap of the outermost shell. By differentiating eq. 5.12 with respect to ρ_1, an expression for g_{rel} is found, whose value depends

on σ, ρ_1, ρ_2, and l. An estimate of its value can be made based on the values obtained by Bourlon *et al.*[60] on one particular MWCNT ($\sigma \sim (20$ k$\Omega)^{-1}/\mu$m, $\rho_1 \sim 22$ kΩ/μm, and $\rho_2 \sim 1$ kΩ/μm). In addition, g_{rel} depends on nanotube length l, which is equal to the separation distance between the two electrodes. Fig. 5.10 shows the intrinsic nanotube resistance and the value of g_{rel} versus electrode separation.

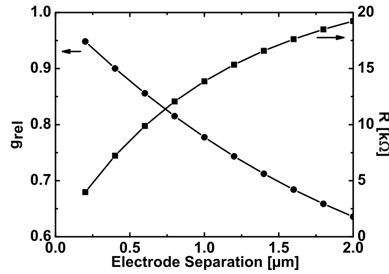

Figure 5.10: g_{rel} and MWCNT resistance vs. electrode separation.

As seen from fig. 5.10 the value of g_{rel} has a noticeable dependence on electrode separation. At 0.2 μm it has a value of ~ 0.95, however, at 2 μm it has dropped to ~ 0.64. This can be understood from the model since the coupling between shells corresponds to an intershell conductance per length: the longer the device, the more coupling. Thus, the device length should be kept short in order to maximize the gauge factor. The shadow mask method used here is well suited for this since it will typically provide electrode separations of a few hundred nanometers. A second observation from fig. 5.10 is that the nanotube resistance increases with increasing electrode separation as expected, although not in a linear fashion due to the larger fraction of the current flowing in the deeper-lying shells at larger separations. It should be stressed that the value of g_{rel} shown here depends on the values of σ, ρ_1, and ρ_2 used in the calculation and can therefore only be interpreted as an approximation. A significant sample-to-sample deviation must be anticipated and was also observed in the study of Bourlon[60]. For example, a higher intershell conductance σ will lead to even smaller values of g_{rel}.

The exact value of g_{ss} can be investigated within the electronic bandgap picture as with the SWCNT case described in chapter 2. This suggests a maximum value of g_{ss} of ~ 190. It can be argued that in the case of a diffusive conductor the Drude model provides a more accurate description. However, no theoretical investigations of the electromechanical properties have been made within this framework. The best estimate can probably be made by considering the experimental investigations[24, 63, 64] that suggest a value of the gauge factor of up to 1000.

Experimental Results

The piezoresistive response of the MWCNT devices was measured using a custom-built set-up similar to the optical manipulation set-up described in chapter 3 (see fig. 3.2). Instead of the manual xyz stage, a Newport MM4005 motorized motion system with a resolution of 50 nm was used for deflecting the cantilever tip in small steps while monitoring the MWCNT resistance. The deflection was performed against a second cantilever as shown schematically in fig. 5.11(a). Fig. 5.11(d) shows an optical microscope image obtained from the measurement set-up where the cantilever is deflected.

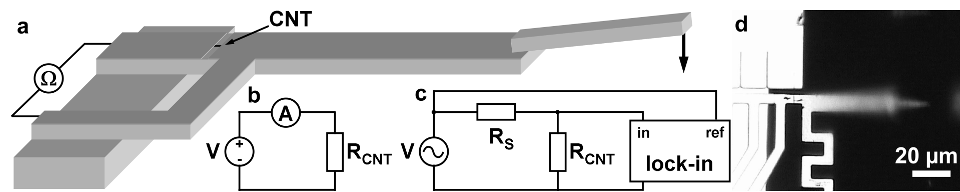

Figure 5.11: (a) Illustration of the deflection principle using a second cantilever. The nanotube resistance R_{CNT} was determined either (b) by measuring the low-bias DC characteristics or (c) by lock-in amplifier measurements. (d) Optical microscope image of a deflected cantilever. The cantilever has a blurred appearance since it has been deflected out of the focal plane of the microscope.

The electrical measurements were performed in one of two different approaches. In the manual approach, a particular cantilever deflection was set and the low-bias current-voltage characteristics were measured with a Keithley 2400 source meter. Next, the deflection was increased and a new $I - V$ curve was measured etc. In the second, automated approach the resistance was monitored using a Stanford Research SR-830 lock-in amplifier. The MWCNT was biased as shown in fig. 5.11(c) and the corresponding voltage drop was monitored as a function of deflection. In this approach, the deflection was controlled by a custom-made LabVIEW program that also read the lock-in amplifier output to correlate the mechanical and electrical data. This approach was used to investigate the durability by performing repeated deflection cycles.

Fig. 5.12(a) shows measurements of the relative change in resistance vs. strain for three different MWCNT devices along with linear fits. The gauge factors derived from these fits are $\sim$ 40, 80, and 180, respectively.

Out of the 26 devices that were assumed to exhibit a low-resistance contact to a MWCNT (17 made by CVD and 9 by arc-discharge), only 3 devices (all made by CVD) showed a gauge factor larger than 40, comparable to or larger than the Si gauge factor of 50 found in [146]. Out of the remaining 23 devices, 10 showed none or very little response with gauge factors below

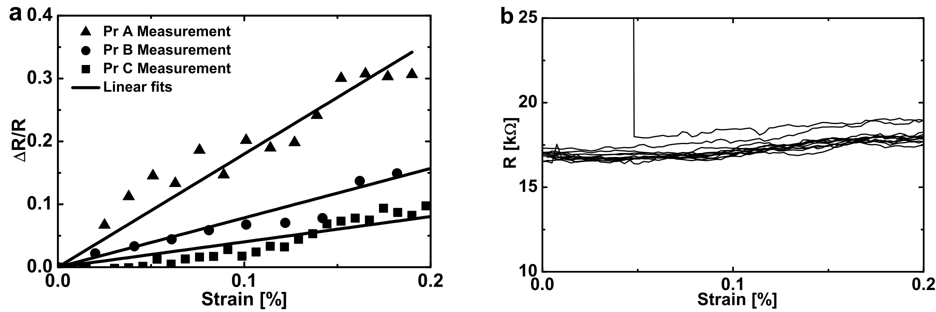

Figure 5.12: (a) Low-bias measurements of the relative change in resistance vs. strain of three MWCNT devices. Pr A and B were characterized with the manual approach, whereas the measurement on Pr C was performed with the automated approach. Also shown are linear fits to the measured data points. (b) Strain response of MWCNT device C that was characterized with the automated approach. The graph shows cycles 15 through 21.

10. Two of these even showed a slight decrease in resistance corresponding to a small negative gauge factor. 10 devices were lost either due to electrical discharges that caused the destruction of the nanotube or because the cantilever had fractured. With the last 3 devices, the nanotube was insufficiently clamped to the cantilever and contact was lost as soon as it was deflected.

An important issue is the reversibility of the resistance when the strain is released. When deflecting the cantilever to only moderate values of nanotube strain (~ 0.2 %) the resistance would typically recover to its original value upon the release of strain. However, eventually contact would be lost irreversibly after continued cycling. Fig. 5.12(b) shows cycle 15 through 21 of a measurement where the contact is ultimately lost. When a large value of nanotube strain (~ 0.5 %) was applied the resistance would typically not recover to its original value upon the release of strain but rather have risen to a higher value. This indicates that at such values of strain the metal contact is not sufficiently rigid to keep the MWCNT clamped.

Some MWCNT devices exhibited a gauge factor similar to or larger than the Si gauge factor, but the majority of the investigated devices showed a much smaller response. Even the most responsive MWCNT device exhibited a gauge factor significantly below the reported values for SWCNTs[24, 63, 64]. As described in the theoretical section, it must be anticipated that the gauge factor of a MWCNT is below that of a SWCNT, however, this cannot fully account for the present observations. Another explanation could be that the MWCNTs used here contain defects, which could make them

less responsive and make the model less applicable. In particular, if the outermost shell has been damaged this could alter the intershell coupling causing a larger fraction of the current to flow in the inner shells. If several shells are carrying the current and some are not stretched or less responsive this could potentially short-circuit the response from a more sensitive outer shell. It can be noted that the 3 devices with significant gauge factors all were made from CVD grown MWCNTs. However, the statistical basis is too limited to make any firm conclusions on the basis of this.

5.3.2 Noise

An important parameter in the comparison between MWCNTs and Si piezoresistors is the obtainable signal to noise ratio. Previous experimental findings suggest a large intrinsic noise in nanotubes[80], which could have a significant, negative impact on the MWCNT sensor performance. Here, the noise level in a MWCNT is compared to the noise in Si piezoresistors.

Two different Si piezoresistors are considered: a relatively large resistor such as the one used in [146] and a small resistor with dimensions similar to those of a MWCNT. Three types of noise are considered: the intrinsic thermal electrical noise and the $1/f$ noise presented in chapter 2, and the noise originating from thermally excited vibrations of the cantilever.

Since the spectral noise power density $S_v(f)$ introduced in chapter 2 corresponds to the noise power in a small frequency interval δf, the average voltage noise power can found by integration of $S_v(f)$ over the measurement bandwidth

$$\langle V_x^2 \rangle = \int_{f_{min}}^{f_{max}} S_{v,x}(f) df, \qquad (5.15)$$

where f_{min} and f_{max} are the low and high cut-off frequencies of the measurement bandwidth, respectively. If the different noise sources are not correlated, the total noise power can be found as the sum of the individual noise power contributions

$$\langle V_{tot}^2 \rangle = \langle V_1^2 \rangle + \langle V_2^2 \rangle + ... \qquad (5.16)$$

From eq. 2.8 and 2.10 the noise power from the thermal noise and $1/f$ noise can be determined

$$\langle V_T^2 \rangle = 4 k_B T R \Delta f \qquad (5.17)$$

$$\langle V_{1/f}^2 \rangle = \frac{\alpha_H}{N} V^2 \ln\left(\frac{f_{max}}{f_{min}}\right), \qquad (5.18)$$

where Δf is the difference between f_{max} and f_{min}. Neither Si resistors nor MWCNTs are expected to exhibit any shot noise as discussed in chapter 2. Therefore shot noise is excluded from the present noise estimation.

Thermal mechanical vibrations of the cantilever will give an additional contribution to the voltage noise power since they appear on top of the desired deflection. These vibrations can be described as an infinite sum of modes ideally each with the same kinetic energy[175]. The amplitude of the noise vibrations decreases rapidly with mode number. Here it is assumed that the measurement is performed in a frequency interval well below the first resonance frequency of the cantilever. Therefore only the contribution of the first mode will be considered. In the off-resonance case, the deflection noise is[176]

$$\langle u(L)^2_{vib}\rangle = \frac{2k_BT}{\pi}\frac{1}{Qk}\frac{\Delta f}{f_{res}}, \tag{5.19}$$

where Q is the cantilever quality factor and f_{res} the resonance frequency of the first mode. f_{res} is given by[175]

$$f_{res} = \frac{1}{2\pi}\sqrt{\frac{k}{m_{eff}}} = \frac{1}{2\pi}\sqrt{\frac{1.875^4}{3}\frac{k}{m}} \simeq \frac{1}{\pi}\sqrt{\frac{k}{m}}, \tag{5.20}$$

where the effective mass m_{eff} has been expressed in terms of the true cantilever mass m. This considers the case of a free cantilever tip, however, in a deflection experiment, the cantilever tip is not freely vibrating but is pressed against an object. This calculation is more extensive, however, since the first mode of a supported tip has an even higher resonance frequency[175], the present, simple calculation will provide a worst-case estimate. By writing the mass in terms of density ρ_m and cantilever volume and by introducing the cantilever spring constant from eq. 5.4, the deflection noise can be written as

$$\langle u(L)^2_{vib}\rangle = 16k_bT\frac{l^5}{QEwh^4}\sqrt{\frac{\rho_m}{E}}\Delta f. \tag{5.21}$$

These deflection fluctuations causes the piezoresistor to experience a fluctuating strain that gives rise to a voltage noise in the output signal. How these fluctuations are reflected in the output signal depends on the read-out method. In the Si piezoresistor study of Thaysen[146], a Wheatstone bridge is used. In a balanced configuration the output voltage V_{out} is

$$V_{out} = \frac{V_{sup}}{4}\frac{\Delta R}{R} = \frac{V_{sup}}{4}g\epsilon, \tag{5.22}$$

where V_{sup} is the supply voltage to the bridge and where eq. 5.7 has been used in the last step. By expressing the strain in terms of deflection, such as through eq. 5.9 in the case of a short piezoresistor, the vibration noise found from eq. 5.21 can be converted into a corresponding voltage noise power $\langle V^2_{vib}\rangle$. Eq. 5.22 will also be used for estimating the vibrational noise in the MWCNT case for comparison with the Si resistor case.

In order to make a quantitative comparison of the noise levels, estimates of the characteristics of the MWCNT, the Si piezoresistors, and the cantilever are made. For the large Si resistor and the cantilever, the values

from [146] are used. Here, the Si resistor has a length of 65 μm, a width of 50 μm and was doped with an implantation dose of $5 \cdot 10^{13}$ cm^{-2} leading to a resistance of 6 kΩ and a gauge factor of 50. For the estimation of the $1/f$ noise, the number of free carriers N is needed. This is found as the product of the implantation dose and resistor width and length: $N = 1.6 \cdot 10^9$.

The cantilever has a length of 200 μm, a width of 50 μm, and a height of 1.3 μm. The cantilever has a multi-layer structure of silicon dioxide, silicon and silicon nitride. Since the greater part of its thickness is made from silicon dioxide, it will for simplicity be assumed that the mechanical properties of silicon dioxide are representative for the entire structure. Thus, density ρ_m=2300 kg/m^3 and Youngs modulus E=75 GPa. The quality factor Q for a similar $\sim$ 200 μm long glass cantilever at atmospheric pressure has been found to be $\sim$ 30[177].

The estimated characteristics of the small Si resistor are based on some recent experimental work that reports nanoscale Si piezoresistors integrated in cantilevers[178]. The investigated device in that study features a Si piezoresistor with a length of 5 μm and a width of 2 μm but it is reported that much smaller resistors have been patterned at the sub-100 nm scale. In order to make a comparison between a Si piezoresistor and a MWCNT of similar dimensions, the dimensions of the small Si resistor will be a length of 300 nm and a width of 100 nm. Together with the doping level used in [178], this causes a resistance of 3.8 kΩ, a number of free carriers of $N = 36 \cdot 10^3$ and a gauge factor of 47.

The MWCNT is assumed to have a resistance of 10 kΩ and a gauge factor of 50. The estimate of the number of free carriers is rather crude since a wide range of quoted values can be found in the literature. Using the empiric relation found by Collins *et al.*[80] $A = \alpha_H/N$=$1.0 \cdot 10^{-11}\Omega^{-1}R$ suggests a value of $A = 10^{-7}$. The Avouris group found a value of $A = 4 \cdot 10^{-6}$ for a 500 nm long SWCNT with a resistance of 10 kΩ[82]. A recent investigation of MWCNT noise reports values of A between $3 \cdot 10^{-7}$ and 10^{-5}[179]. For the present estimation, a value of $A = 10^{-6}$ will be used corresponding to $N = 2 \cdot 10^3$.

The contributions from both $1/f$ noise and the vibrational noise to the total voltage noise will depend on the bias voltage. Thaysen investigated the influence of the Wheatstone bridge supply voltage on the signal to noise ratio[166] and suggests to use a 2 V supply voltage. (Note that in the bridge configuration only half the supply voltage is dropped across the piezoresistor). For the Si piezoresistors a bias voltage of 1 V is therefore used in the noise estimation. It is not clear what the optimum MWCNT bias voltage is. A high bias voltage will cause the current to penetrate more into the deeper-lying shells thus lowering the gauge factor. However, a low bias voltage will reduce the output signal (cf. eq. 5.22) and thereby have a negative impact on the noise properties. To make a direct comparison with the Si resistors, a bias voltage of 1 V is also assumed for the MWCNT, however,

it should be noted that the optimum bias voltage might be lower.

Finally the measurement bandwidth must be found. Along the line of Thaysen[166], a 'DC' measurement bandwidth of 50 Hz is used (from 1 Hz to 51 Hz). At this low frequency, the $1/f$ noise is significant. In addition, a comparison is made at a higher frequency where the $1/f$ noise contribution is less important. By equating the thermal noise and the $1/f$ noise, a characteristic frequency f_c can be found, above which the thermal noise is dominating. For the MWCNT with a 1 V bias voltage, f_c=6 GHz. From a practical point of view, measuring at in the GHz range can pose some difficulties. One (trivial) problem is that very few (if any) commercial lock-in amplifiers are equipped to measure at such high frequencies, although specialized equipment does exist for high-frequency measurements at several hundred MHz. However, at such frequencies the measurement is significantly more susceptible to the influence of extrinsic noise through stray capacitances. These can of course be minimized by careful design of the experimental set-up. However, given the present scope of evaluating the technological relevance of MWCNTs, such measurements using highly specialized equipment and a fine-tuned, delicate measurement set-up does not provide a very useful assessment anyway. Instead the high-frequency range is chosen at 50 kHz still with a bandwidth of 50 Hz.

In order to make a quantitative evaluation, the noise power values are scaled to eliminate the influence from the difference in bias voltages. Here the noise power values are scaled by the output signal corresponding to a 10 nm deflection of the cantilever tip. Thus, the noise values presented in table 5.1 are determined as $\langle V_x^2\rangle/V_{out}^2(u(L)\text{=}10\text{ nm})$.

	f: 1 - 51 Hz			f: 50.00 - 50.05 kHz		
	Si$_{\text{lar.}}$	Si$_{\text{sm.}}$	MWCNT	Si$_{\text{lar.}}$	Si$_{\text{sm.}}$	MWCNT
$\langle V_T^2\rangle/V_{out}^2$	$3\cdot10^{-5}$	$2\cdot10^{-5}$	$6\cdot10^{-5}$	$3\cdot10^{-5}$	$2\cdot10^{-5}$	$6\cdot10^{-5}$
$\langle V_{1/f}^2\rangle/V_{out}^2$	$3\cdot10^{-2}$	$2\cdot10^{3}$	$3\cdot10^{4}$	$9\cdot10^{-6}$	0.4	7
$\langle V_{vib}^2\rangle/V_{out}^2$	$6\cdot10^{-9}$	$6\cdot10^{-9}$	$6\cdot10^{-9}$	-	-	-
$\langle V_{tot}^2\rangle/V_{out}^2$	$3\cdot10^{-2}$	$2\cdot10^{3}$	$3\cdot10^{4}$	$4\cdot10^{-5}$	0.4	7

Table 5.1: The different contributions to the total voltage noise power normalized to the output signal from a 10 nm deflection of the cantilever tip.

In table 5.1 no values are provided for the contribution from the thermal vibrations of the cantilever in the high frequency bandwidth. Eq. 5.19 is only valid when the measurement bandwidth is far from the resonance frequency of the cantilever. Since the resonance frequency of the considered cantilever is some ten kHz, using eq. 5.19 can no longer be justified. The noise in the on-resonance case is Q^2 times higher than the prediction from eq. 5.19[176]. A worst-case estimate of the noise in the high-frequency case is thus 10^3

times the values given in the low-frequency range. Still, its contribution to the total noise is insignificant.

Several observation can be made from table 5.1. In the low-frequency interval, by far the most significant noise source is the $1/f$ noise. As anticipated[80] the $1/f$ noise in the MWCNT is quite high, however, the noise in the small Si resistor is seen to be comparable, given the uncertainty on the numbers used for the calculations. The large noise is thus simply due to the low number of carriers caused by the small dimensions. In the high-frequency interval, the $1/f$ noise is reduced but it still rather high both for the small Si resistor and the MWCNT. The thermal electrical noise is similar in all three components. However, if the bias voltage of the MWCNT must be reduced below 1 V as discussed previously, this will have a negative effect on the thermal electrical noise contribution. In addition it is seen that the mechanical noise is negligible. However, it should be pointed out that this comparison is made with a relatively large cantilever. An accurate comparison of the small Si resistor and the MWCNT in a compact cantilever structure would require a new set of computations. Even though this could change the relative importance of the mechanical noise, it would still have approximately the same magnitude for the Si resistor and the MWCNT.

5.4 Discussion and Outlook

Despite some appealing experimental demonstrations of high gauge factors in carbon nanotubes, several significant obstacles against their technological use exist. Due to the comparably easier handling of MWCNTs than of SWCNTs, this study focused on examining MWCNTs. The results show that MWCNTs appear less responsive than SWCNTs. The highest gauge factor observed here was ~ 180, however, in a similar study by Søren Dohn a single MWCNT device was found to exhibit a gauge factor of ~ 500[145]. Still these values are lower than what has been found in SWCNTs[24, 63, 64]. A limited proportion of the investigated devices did have a gauge factor comparable to or larger than a silicon piezoresistor, but also showed notable non-linear deviations that would limit their applicability as strain sensors. A large part of the devices showed no appreciable response to strain. It must be expected that MWCNTs are less responsive than SWCNTs as more shells are carrying the current, some of which may not be subjected to strain. However, this can not fully explain the observations, as this should theoretically not cause such large reductions in gauge factor. A second possibility could be that defects are causing a larger portion of the current to be flowing in the innermost shells or that the shell structure is not maintained and the notion of semiconducting shells is less relevant. If a significant number of shells are carrying the current, the resulting gauge factor must be the average response of these shells. This would mean that less responsive shells could short-

circuit the response from more sensitive shells thus causing a low average gauge factor. In that case, a possible remedy could be to use less defective MWCNTs such as those produced with the arc-discharge method. The results obtained here do not indicate that arc-discharge nanotubes have higher gauge factors, however, since TEM images of these MWCNTs have not been obtained, it can only be assumed that these indeed have fewer defects. Also, from a technological point of view, the use of arc-discharge MWCNTs is not favored since these cannot be fabricated in-situ and are therefore less suited for high-volume device fabrication. Assuming that near-perfect MWCNTs could be fabricated by CVD, a remaining problem would be the inability to synthesize nanotubes with a predetermined geometry. This makes it impossible to design for a particular gauge factor. If fabricating nanotube based strain sensors, one must therefore in any case anticipate that a significant number of devices will exhibit a poor sensitivity due to a low intrinsic gauge factor.

Another issue is that of reversibility. The MWCNT devices fabricated here can only tolerate a rather limited amount of strain before the resistance increases irreversibly, presumably due to degradation of the contact. However, even with a limited level of strain, continued cycling of the load eventually caused breakdown. Assuming that the cause of this problem is insufficient mechanical rigidity of the contacts, a possible remedy could be to clamp the nanotube to the cantilever surface by electron beam induced deposition of 'soldering' material[127]. This has been shown to effectively pin a MWCNT to a cantilever[180]. This was tried but no firm conclusions could be drawn from these studies since only a very limited number of devices could be fabricated, none of which showed any electrical connection.

A further problem with the inherent unpredictability of even high quality SWCNTs is the difficulty in fabricating an on-chip balanced Wheatstone bridge as with Si resistors. The MWCNT devices exhibited dissimilar resistances as expected, ranging between a few and some tens of kΩ. Thus, fabricating four MWCNT resistors with equal resistance is not realistic and the bridge will not be balanced. In order to obtain more similar resistance values, the four resistors could be imagined as being fabricated using different segments of the same nanotube. However, with the present methods, this is not feasible. Another option could be to fabricate three on-chip Si resistors and then use a MWCNT as the fourth resistor in a Wheatstone bridge. However, the MWCNT resistance is unknown during the microfabrication process, and it is thus not possible to design the Si resistors to a value that can be expected balance the bridge precisely. A balanced circuit would then require trimming the Si resistors after integration of the MWCNT. Alternatively the bridge could be realized with external adjustable resistors. This would be easy to realize, however, it would be more susceptible to extrinsic noise since longer wires would be necessary. Also the point of using the bridge circuit to compensate for unwanted thermal and/or mechanical influ-

ences is lost. Thus, using a balanced Wheatstone bridge for signal read-out from a nanotube device is problematic.

Another challenge is that of integrating such small structures with a suitable microsystem. For high-volume fabrication, the most promising integration method for nanotubes is in-situ growth, however, some unsolved problems still remain with this method as discussed in chapter 4.

In terms of realizing a compact sensor, very small Si piezoresistors fabricated with a top-down approach requires the use of a nanolithography technique for defining the resistors. As demonstrated recently, electron beam lithography is one option[178]. Although industrial grade electron beam writers are fast, this is a serial process and therefore not optimal for fabricating a very large number of devices. However, since a similar technique is necessary for realizing the catalyst particles for nanotube in-situ growth, this argument also applies to nanotubes. In the question of down-scaling of the sensor, the apparent advantage of the inherently small cross section of nanotubes is thus not of much significance.

Noise is an additional point to consider. As discussed in the earlier section, the intrinsic $1/f$ noise is not significantly higher in a nanotube than in a Si resistor of similar dimensions. However, this comparison only applies to the case of a very small cantilever based sensor where the piezoresistor width must be in the sub-100 nm range. If a width of for example 1 μm is acceptable, then the Si resistor would be the better choice since it can be made larger thus reducing the noise.

Another aspect is the influence of external environmental factors. Si resistors are typically encapsulated to avoid the influence of external factors. This could for example be water that condenses from the surroundings. A nanotube could also be affected by such external factors and encapsulation would also in this case be necessary.

In the beginning of this investigation it was decided to focus on MWCNTs rather than SWCNTs. However, most arguments presented here similarly applies to SWCNTs and it is therefore also possible to assess their applicability as strain sensors. Analogous to the MWCNTs, it is difficult to realize an on-chip balanced bridge and it is not possible to predict their gauge factor. Since high gauge factors of up to $\sim$ 1000 have been found experimentally, it would be possible to fabricate a significant number of SWCNT based devices and just use those with high gauge factors if a particular application requires a very sensitive system and optical detection is impossible. However, for most applications this is not a viable route. Also, the high $1/f$ noise exhibited by small conductors will be even more pronounced in a SWCNT.

Chapter 6

Electrical Properties of p6P Nanofibers

Organic semiconductors are of technological interest due to their electrical, optical, and electro-optical properties. The first organic field-effect transistor (OFET), based on an organic thin film, was demonstrated in 1986[181] with a rather low carrier mobility of $\sim 10^{-5}$ cm^2/Vs. More recent studies have demonstrated a rubrene single-crystal FET with a mobility of up to $\sim$ 15 cm^2/Vs[182]. Equally appealing are the electro-optical properties, which allowed Tang and VanSlyke to demonstrate an organic light-emitting device (OLED) - also based on a thin-film sandwich structure[183]. Later OLED research has focused on optimizing different parameters such as efficiency and brightness[184], tuning the color, or controlling the molecular order to obtain polarized light[185]. Using both the electrical and electro-optical properties, organic light-emitting field-effect transistors can be realized[186, 187]. By combining the electroluminescent properties of organic semiconductors with micro- and nanofabrication techniques, nanoscale OLEDs have been realized[188, 189]. In both studies, electron beam lithography was used to define the active area, which resulted in electroluminescence from $\sim$ 60 nm diameter areas.

Another approach to a nanoscale light source is to use self-assembled nanocomponents. Lieber and co-workers have demonstrated a nanoscale LED based on either a single heterostructured nanowire[20] or crossed-junction n- and p-type nanowires[17] and have recently shown an addressable LED array entirely based on inorganic semiconducting nanowires[22]. Also making use of inorganic semiconductors, Yang and co-workers integrated both active and passive optical components, such as nanowire lasers and nanoribbon waveguides, into a single nanophotonic device[190, 19]. Potential applications of self-assembled nanocomponents can thus be within nanoscale photonic or optoelectronic circuits or in on-chip optical analysis of chemical or biological samples[22].

Para-hexaphenlyene nanofibers exhibit some equally promising properties as their inorganic counterparts. As described in chapter 2, these organic nanofibers have a polarized, blue photoluminescence output[37] and presumably a similar electroluminescence output[88], they have waveguiding capabilities[87], and they can function as laser gain medium[89]. The use of these appealing properties in for example optoelectronic applications requires the ability to integrate the nanofibers with surrounding circuitry. Since the self-assembly process for nanofiber fabrication requires the use of a special growth substrate[4], an in-situ growth approach, as with carbon nanotubes, appears less viable at present. Recently, Briseno and co-workers did demonstrate an alternative method by fabricating large organic single-crystals on a patterned self-assembled monolayer template[191], but it is not clear if the method is compatible with subsequent microfabrication processing steps. The most promising route at present is thus to have nanofiber fabrication and device construction as two separate, consecutive steps. As shown in chapter 3, it is possible to controllably position nanofibers and establish electrical contact through the shadow mask method.

This chapter will describe the investigation of the electrical properties of p6P nanofiber devices performed in order to gain a detailed understanding of the charge injection and transport properties to enable the realization of efficient injection of both charge species for light generation. It will start with a theoretical treatment of the various aspects of charge injection and transport in organic semiconductors, since these aspects play a vital role in electroluminescence. The second part covers the experimental studies of the electrical properties of single-nanofiber devices.

6.1 Charge Injection and Transport Theory

Electroluminescence in organic semiconductors originate from the radiative decay of an exciton, which has formed by the binding of an electron and a hole polaron. This requires injection of both charge species from the cathode and anode, respectively, and their transport to the recombination zone by an applied electric field[192]. Optimizing the light generation process therefore involves balancing the electron and hole currents. This requires a detailed understanding of the charge injection and transport properties. Fig. 6.1 schematically shows the steps involved in the light generation process.

As shown in fig. 6.1, a simple, organic semiconductor device typically consists of the organic semiconductor contacted by two metal electrodes, which comprise the anode and cathode. The electrical properties of such a device are influenced both by the intrinsic properties of the semiconductor bulk and of the properties of the contacts. The current through an organic semiconductor is thus limited either by an energy barrier at the injecting contact or by the semiconductor bulk. This leads to two different conduc-

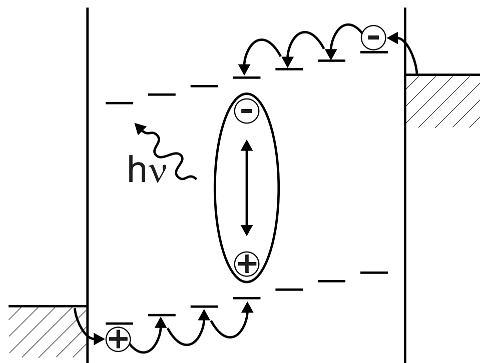

Figure 6.1: Conceptual drawing of the light generation process in an organic semiconductor. Carriers are injected at the electrodes, transported towards each other, form an exciton that finally recombines and emits a photon.

tion regimes[193]: injection-limited current (ILC) and bulk-limited current. However, the contact properties and the bulk properties are not independent, and in a particular device the electrical properties are therefore determined by the specific combination. For example, the injection rate has been shown to depend on carrier mobility[194]. A full description therefore requires the consideration of the device as a whole. Still, investigating the injection and transport mechanisms is alleviated by considering each subject separately. This section will first describe charge injection from a metal to an organic semiconductor, and will next focus on describing the transport.

6.1.1 Charge Injection

When considering charge injection and transport in organic semiconductors, it is useful to adopt a band structure representation similar to that of inorganic crystalline semiconductors[195]. However, at this point some of the important differences described in chapter 2 should be noted: whereas the carriers in an inorganic semiconductor are delocalized over the entire crystal forming broad and continuous energy bands, they localize on individual molecules in an organic crystal and the energy bandwidths are much smaller. The electronic properties are therefore primarily determined by the properties of the individual molecules. A simplified model of the energy bands of a molecular solid is shown in fig. 6.2.

Fig. 6.2(a) shows the energy levels of an isolated molecule with I_i and A_i being the ionization energy and electron affinity, respectively. When the molecules form a crystal, the energy level picture changes to that depicted in (b). In the solid state, the exact positions of the energy levels are shifted due to polarization effects in the surrounding medium. Here, I and A are the ionization energy and electron affinity, respectively, of the crystal, while E_F

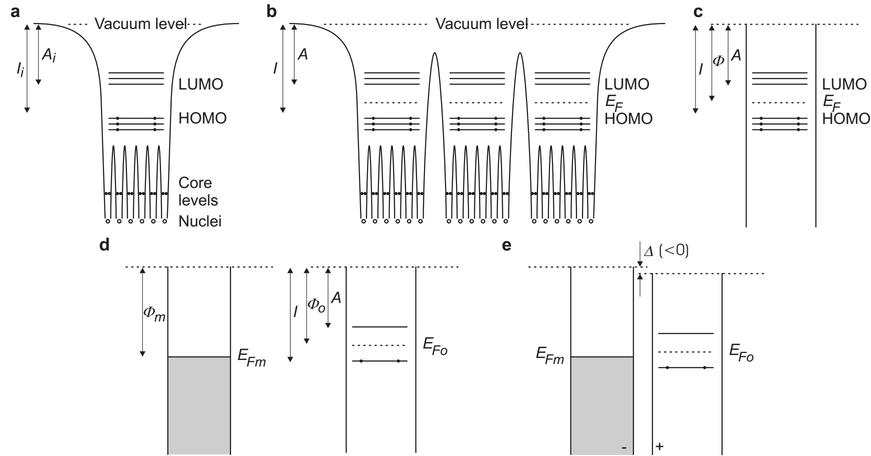

Figure 6.2: Schematic drawing of the organic molecular energy levels and the interface energetics of a metal-organic semiconductor contact. (a) The energy levels of an isolated molecule. The labels are described in the text. (b) The energy levels of a molecular crystal. Due to polarization effects in the surrounding medium, the molecular levels are slightly shifted compared to the isolated case (not shown). (c) A simplified picture of a molecular crystal. (d) A metal and a molecular crystal before contact. (e) A metal and a molecular crystal after contact. Also indicated is a possible vacuum level shift caused by a surface dipole (the indicated shift corresponds to a negative Δ value). Adapted from [195].

is the Fermi energy. A simplified version of (b) is shown in (c), which is used when illustrating the formation of a contact with a metal. (d) shows the situation before contact is made between a metal, characterized by a Fermi energy E_{Fm}, and a molecular crystal. (e) depicts a possible scenario after contact is made. A small vacuum level shift between the metal and semiconductor is indicated, which could be caused by an interface dipole as will be discussed later. The energy scheme depicted in (e) is not in equilibrium as seen from the difference between the two Fermi levels. However, in an impurity-free organic crystal, practically no charge carriers can be thermally excited from the HOMO to the LUMO level, thus making the Fermi level a less well-defined quantity[97]. With very few free carriers, band bending will be negligible and the potential of the organic crystal will therefore primarily be determined by the vacuum level shift Δ. As seen from fig. 6.2 (e), barriers for both hole and electron injection exist with heights of:

$$\phi_h = I - \phi_m - \Delta \tag{6.1}$$

$$\phi_e = \phi_m - A + \Delta, \tag{6.2}$$

where ϕ_h (ϕ_e) is the barrier for hole (electron) injection.

Optimizing the efficiency of light generation involves balancing the hole and electron current. As a first attempt, this can be tried by choosing appropriate cathode and anode materials, which have equal injection barriers to the LUMO and HOMO levels, respectively, in order to balance electron and hole injection. However, this simplified picture is rather crude as it neglects factors such as differences in electron and hole mobilities and variations in the interface between the organic material and different electrode materials. Therefore, a more detailed consideration of the factors influencing injection is necessary.

A possible interface dipole will introduce a vacuum level shift Δ as shown in fig. 6.2(e). This can for example be caused by charge transfer across the interface, interfacial chemical reactions, or other type of charge rearrangement[195]. An often used method for investigating such interface energetics is ultraviolet photoelectron spectroscopy (UPS), which has been used extensively in the study of interfaces between metals and organic semiconductors, including p6P[99, 196, 197]. The Seki group observed a significant vacuum level shift when p6P is deposited on Mg (-0.4 eV) and Au (-0.8 eV)[196]. However, in the opposite case (Au evaporated onto p6P) the spectral features of p6P are still present even after depositing significant amounts of Au. This suggests that Au atoms or clusters penetrate the p6P and the interface is therefore less sharp. Similar results of very little vaccum level shifts was also observed by the Graz group when evaporating Al onto p6P (shift less than 0.1 eV)[197]. This indicates that the Al only physisorps to the p6P and no chemical reaction occurs. In a later study employing Auger electron spectroscopy[198] it was found that there is an interface region where Al and p6P mix. At lower evaporation rates, the interface region becomes narrower. Another study investigated the interface between p6P and Sm - both with p6P on Sm and Sm on p6P[99]. In both cases, very small vacuum level shifts were observed, indicating physisorption and an interface dipole of < 0.2 eV. The exact value of the vacuum level shift is influenced by a number of factors and it is in a particular device difficult to estimate. The sample preparation and investigation in the aforementioned studies have all been performed under UHV conditions. Recently it has been argued that more realistic device fabrication conditions can cause water molecules to be integrated in the interface and cancel the interface dipole[193].

Another important aspect is the injection mechanism. Several theoretical approaches have been proposed to describe carrier injection into an organic semiconductor[97] including thermionic emission across the interface barrier or a tunnelling process. In contrast to conventional inorganic semiconductors, injection in this case occurs into a localized state. Thus, the 'conventional' models are of limited applicability and a model that considers the localization aspect must be used. An important point is that in low mobility semiconductors there can be a significant charge carrier concentration at the injecting contact giving rise to a back-flow of carriers to

the electrode[97]. This can be studied by considering the electrostatic potential experienced by a carrier entering the organic semiconductor. Here, the injection of holes into the HOMO level is considered, however, a similar analysis would apply to the case of electron injection into the LUMO level. The externally applied field F together with the Coulomb interaction with the image charge give rise to an energy barrier $U(x)$

$$U(x) = \phi_h - \frac{e^2}{16\pi\epsilon_r\epsilon_0 x} - eFx, \tag{6.3}$$

measured with respect to the metal Fermi level. e is the elementary charge, $\epsilon_r\epsilon_0$ is the permittivity, and x is the distance from the interface. A schematic illustration of the energy levels associated with the injection process is shown in fig. 6.3.

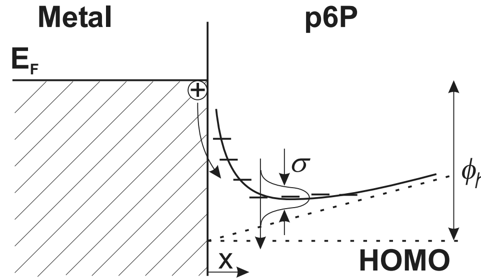

Figure 6.3: Schematic drawing of the carrier injection process from a delocalized state in the metal to a localized state in the organic semiconductor. The energy levels in the semiconductor are determined by the barrier height, the image charge, and the applied electric field.

Scott and Malliaras[199] have suggested a phenomenological model that uses the principle of detailed balance to determine the contributions of the currents crossing the interface in the potential given by eq. 6.3. These are the injected current and the backwards flowing recombination current, which is made up of charges recombining with their own image. At zero bias, the injected current density, caused by thermionic emission over the barrier, is exactly cancelled by the recombination current density. When an electric field is applied, the expression for the total current density becomes[199]

$$J = 4N_0\psi^2 eF\mu \exp\left(\frac{-e\phi_h}{k_BT}\right)\exp(f^{1/2}), \tag{6.4}$$

where N_0 is the molecular density and where the electric field dependence is also included implicitly as the reduced electric field $f = e^3F/4\pi\epsilon_r\epsilon_0 k_B^2T^2$. The exponential term including f accounts for the conventional Schottky lowering of a barrier due to an electric field. ψ is given by $\psi = f^{-1} + f^{-1/2} - f^{-1}(1 + 2f^{1/2})^{1/2}$.

Where thermionic emission dominates at lower barrier heights, the contribution from tunnelling will become more significant at larger barrier heights. An analytical model has been suggested by Arkhipov and coworkers[200] based on thermally assisted tunnelling into localized states. It treats injection as a two step process: 1) injection from the metal electrode into a localized state and 2) either the return of the carrier to the electrode or its diffusive escape into the semiconductor bulk. The injected current density J is therefore found as the product of the tunnelling probability $\exp(-2\gamma x_0)$ (i.e. the probability of the carrier reaching the position x_0 in the first jump), and the escape probability $w_{esc}(x_0)$

$$J \propto \int_a^\infty dx_0 \exp(-2\gamma x_0) w_{esc}(x_0) \int_{-\infty}^\infty dE' \mathrm{Bol}(E') g[U(x_0) - E'], \tag{6.5}$$

where γ is the inverse localization radius and $\mathrm{Bol}(E)$ is a Boltzmann factor

$$\mathrm{Bol}(E) = \begin{cases} \exp\left(-\frac{E}{k_B T}\right), & E > 0, \\ 1, & E < 0. \end{cases} \tag{6.6}$$

The escape probability $w_{esc}(x_0)$ is the probability that a carrier, which has made an initial jump to x_0, will avoid surface recombination i.e. will contribute to the current, and is determined by

$$w_{esc}(x_0) = \frac{\int_a^{x_0} dx \exp\left[-\frac{e}{k_B T}\left(Fx + \frac{e}{16\pi\epsilon_r\epsilon_0 x}\right)\right]}{\int_a^\infty dx \exp\left[-\frac{e}{k_B T}\left(Fx + \frac{e}{16\pi\epsilon_r\epsilon_0 x}\right)\right]}, \tag{6.7}$$

with a being the distance from the electrode to the first site in the semiconductor. $g(E)$ is the density of states. In the case of a single energy level this would correspond to a delta function. However, in the case considered by Arkhipov, it is modelled as a gaussian energy distribution characterized by an energy width σ to account for a possible energy level broadening

$$g(E) = \frac{N_0}{\sqrt{2\pi}\sigma} \exp\left(-\frac{E^2}{2\sigma^2}\right), \tag{6.8}$$

The density of states is also indicated in fig. 6.3.

6.1.2 Charge Transport

The microscopic aspects of charge transport can be described within the framework introduced in chapter 2. Here, a more phenomenological approach is taken, where the intrinsic processes concerning charge transport are not considered, but where the transport properties of a particular organic crystal is expected to be quantified through the mobility μ. As described in chapter 2, an organic semiconductor can transport both electrons and

holes. It should therefore be characterized both by an electron mobility μ_e and a hole mobility μ_h. In the descriptions here it is assumed that the current is determined by the semiconductor bulk, i.e. any contact resistance is considered small and ohmic.

Different conduction regimes exist. At low voltages, the current is due to the drift of the free carriers in response to an applied electric field, which gives rise to a current density J_{Ohm} following Ohm's law[201]

$$J_{Ohm} = en_0\mu F, \tag{6.9}$$

where n_0 is the free carrier density, the electric field F is the applied voltage V divided by device length L, and a single carrier type is assumed.

Due to the large bandgap of most organic semiconductors, only very few carriers are thermally excited from the HOMO to the LUMO level at room temperature and the free carrier density is therefore correspondingly low. Assuming the Fermi level to be located mid-gap between the HOMO and LUMO levels, which in p6P are separated by 3.1 eV[99], the probability of thermally exciting an electron-hole pair can be calculated from Fermi-Dirac statistics to be of the order of 10^{-27}. In an actual crystal, more free carriers will be present due to the inevitable foreign species, however, the free carrier density will still be low compared to traditional inorganic semiconductors.

At higher voltages, the density of the injected carriers will become comparable and eventually exceed the free carrier density. The transport mechanism will then change from eq. 6.9 to the space-charge limited (SCL) regime, where voltage dependence of the current density will be given by the Mott-Gurney formula[201]

$$J_{SCL} = \frac{9\epsilon_r\epsilon_0\mu}{8}\frac{V^2}{L^3}. \tag{6.10}$$

In the derivation of the Mott-Gurney formula, a geometry relating that a parallel-plate capacitor has been used[201]. In other device geometries the length dependence can be different. For example, the in-plane space-charge limited current in a thin semiconductor layer is predicted to scale inversely with the square rather than the cube of the device length[202].

The presented models are idealized versions, where it is assumed that the organic crystal contains no carrier traps and that the current is unipolar. In a practical device, traps will be present which will alter the current-voltage characteristics. If a single level of shallow traps is available (i.e. energetically located where the traps are initially unoccupied), injected carriers will become trapped and the current density will be less than the prediction of eq. 6.10 by an amount equal to the ratio between free and trapped carriers[201]. More complex trap distributions or deeper-lying traps will result in a different functional form of the current-voltage characteristics, which can be used to investigate these trap distributions in more detail. If the current is

carried by both types of carriers, space-charge effects will become less significant and larger current densities can be supported. In this case, which is of particular interest in relation to OLEDs, the transport properties are influenced by a number of additional factors including the recombination cross section and the average lifetime of a carrier before recombination[201].

As discussed previously, charge injection and charge transport are somewhat linked, and both aspects should therefore be considered in the analysis of a particular device. Here, a simple model is proposed, which incorporates both aspects, inspired by a combined model developed by Arkhipov *et al.*[203]. The model considers a device of length L with the injecting contact located at $x = 0$. It uses Ohm's law (eq. 6.9) as the starting point to describe the current in the bulk, however assuming that both the electric field strength and the carrier density can vary along the device length i.e. $F = F(x)$ and $n_0 = n_0(x)$. This is combined with the Poisson equation

$$\frac{dF}{dx} = \frac{en_0}{\epsilon_r \epsilon_0} \tag{6.11}$$

to yield

$$F\frac{dF}{dx} = \frac{J}{\epsilon_r \epsilon_0 \mu}. \tag{6.12}$$

The next step is to solve eq. 6.12 with the appropriate boundary condition, which is that the bulk current density J should equal the injected current density, to yield the electric field along the device. The solution of eq. 6.12 is

$$F(x) = \sqrt{\frac{2J}{\epsilon_r \epsilon_0 \mu} x + k}, \tag{6.13}$$

where k is an integration constant to be determined from the boundary condition, i.e. the injected current density, which can be found from eq. 6.5. Note that in the calculation of the injected current density, the electric field strength *at the injecting contact* should be used, i.e. $F(0)$. The voltage drop across the device can then be found by integrating the electric field (eq. 6.13) along the device.

Due to the somewhat complicated expression for the injected current density, it is not possible to find a closed-form solution to describe the $J-V$ relationship, however, it is possible through an iterative procedure to find corresponding values of J and V as shown in fig. 6.4(b) for a particular set of device parameters. The model can be used to investigate how different parameters influence the electrical properties. Fig. 6.4(a) shows the spatial distribution of the electric field along the device for three different values of the barrier height.

As evident from fig. 6.4(a) the spatial distribution of the electric field depends on the height of the injection barrier. It is of interest to consider the two limiting cases of a vanishing barrier and of a high barrier, corresponding

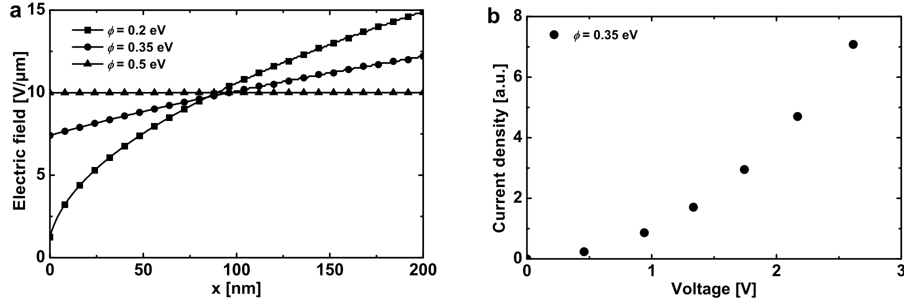

Figure 6.4: (a) Spatial dependence of the electric field along a 200 nm long device with an applied voltage of 2 V for injection into a single energy level. The following values have been used: $\epsilon_r = 1.9$, $\mu = 10^{-1}$ cm^2/Vs, $T = 300$ K, $\gamma = (3\ \text{Å})^{-1}$, and $a = 5.6$ Å. (b) The current density vs. voltage for an injection barrier height of 0.35 eV calculated with the same parameters as in (a).

to purely bulk-limited and purely injection-limited current, respectively. A very low barrier causes a vanishing electric field at the injecting electrode. In this case, the integration constant k in eq. 6.13 becomes negligible, which makes it possible to find a closed-form solution for the current density vs. voltage relation. As expected, this becomes equal to the space-charge limited relationship given by the Mott-Guerney formula (eq. 6.10). In the opposite case of a high barrier, the electric field is constant along the device. This causes the current density to be determined by the injecting contact, i.e. by eq. 6.5 with the electric field at the injecting electrode equal to V/L. It should be emphasized that this model is rather crude. More sophisticated numerical models that incorporate both drift and diffusion currents and recombination processes have been developed[204] that also permits the inclusion of local changes in the organic material such as low mobility regions near the contacts[205].

6.2 Experimental Investigations of Electrical Properties

With the ultimate goal of establishing electroluminescence in p6P nanofibers, a number of experimental investigations of their electrical properties have been performed. These studies were performed in order to obtain a better understanding of the injection and transport properties to be able to optimize for efficient injection of both carrier types.

Parts of these studies were made in a collaboration with Henrik Henrich-

sen, Daniel Engstrøm and Casper Hyttel Clausen, who during their master projects have studied various aspects of p6P nanofibers, either within (DE and CHC) or affiliated with (HH) the Nanointegration group.

6.2.1 Current-Voltage Characteristics

Using the shadow mask technique, a total number of 161 p6P nanofiber devices were fabricated. These were electrically characterized with the custom-built set-up that uses a Stanford Research SR-570 current preamplifier as described in section 3.6. The voltage was incremented in small steps and the corresponding current measured. 24 of the 161 devices showed electrical characteristics that could be interpreted as current conduction through the nanofiber. Some devices were lost due to problems with the shadow mask method as described in chapter 3. However, some samples displayed what appeared to be open circuit characteristics at low voltages and then a non-reversible break down phenomenon would occur at a higher voltage causing a short current pulse to flow, indicating contact problems. These could be due to a possible contamination that could have originated from the growth substrate and could have been transferred along in the micropipette. A second problem could be oxidation of those electrodes not made of noble metals.

The 24 working devices were then examined both with SEM and AFM to determine the nanofiber dimensions. Fig. 6.5 shows how the nanofiber height h, width w, and uncoated length l have been determined.

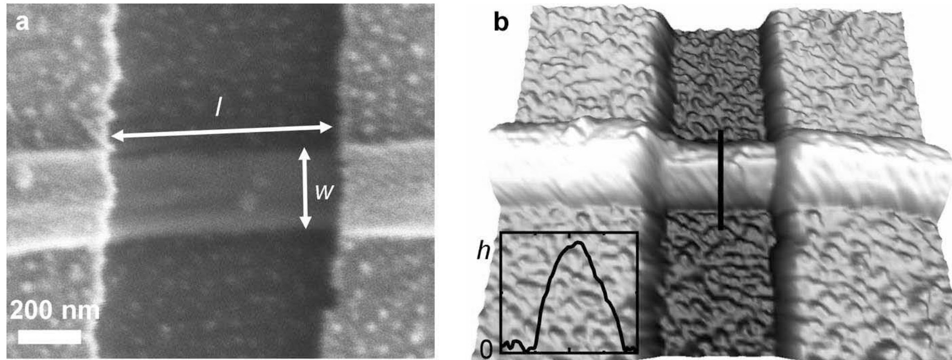

Figure 6.5: (a) SEM image of a p6P nanofiber contacted with two electrodes. w and l are nanofiber width and uncoated length, respectively. (b) 1.9 by 1.6 μm^2 AFM image of the same nanofiber. Its height h is found from the cross sectional profile.

In order to test the influence from the contact, devices with different contact materials were fabricated. Fig. 6.6(a) shows typical current density vs.

voltage ($J-V$) characteristics of a nanofiber contacted with Au electrodes (J determined as $I/(w \cdot h)$).

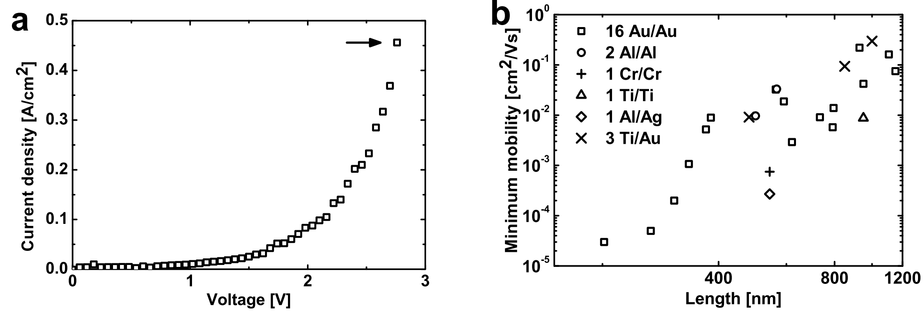

Figure 6.6: (a) Typical $J-V$ characteristics of a p6P nanofiber device with Au contacts. The arrow indicates the last sample point, used to extract a *minimum* mobility value as described in the text. (b) Estimated *minimum* mobility values for all 24 working devices. Syntax: [cathode]/[anode].

Considering the energetics of the Au-p6P interface (Au Fermi energy of $\sim$ 5.1 eV[206] and p6P ionization energy of $\sim$ 6.0 eV[99]), an energy barrier for hole injection of $\sim$ 0.9 eV is expected (neglecting a possible interface dipole). Such a barrier height would typically cause the current to be injection limited[204] as also suggested by the example in fig. 6.4(a) which is close to the real device parameters. However, the apparent parabolic dependence of the last part of the $J-V$ characteristics could indicate SCL behavior. In order to investigate this in more detail, the measured $J-V$ characteristics were analyzed with the Mott-Gurney theory (eq. 6.10). This provides an intrinsic upper limit to the current flow. Contact effects, defects, traps, or any other influencing factors will always cause the current to be smaller than the prediction of eq. 6.10[207]. Thus, if the permittivity and device length are known, an estimate of the *minimum* mobility μ_{min} can be extracted from the $J-V$ measurements by rearranging eq. 6.10

$$\mu_{min} = \frac{8JL^3}{9\epsilon_r\epsilon_0 V^2}. \tag{6.14}$$

The exact appearance of the $J-V$ characteristics measured on different samples vary somewhat with fig. 6.6(a) showing a typical example. It was observed that a high bias voltage could induce a non-reversible break-down process. In order to avoid this, the samples were biased only up to moderate values of voltage. Similar to the method used by de Boer *et al.*[207], the current measured at the maximum bias voltage was used in the calculation of μ_{min} as indicated with an arrow in fig. 6.6(a).

The extracted minimum values of mobility show a significant spread over four orders of magnitude between $3 \cdot 10^{-5}$ cm^2/Vs and $3 \cdot 10^{-1}$ cm^2/Vs. This corresponds to the large spread observed in a similar study on tetracene crystals[207]. In order to investigate the cause of this large spread, the minimum mobility values have been plotted versus device length in fig. 6.6(b). If the current had indeed been space-charge limited, no length dependence of the extracted mobility values is expected as mobility is an intrinsic material property. The observed dependence therefore clearly indicates that the SCL regime is not reached and that the contact barriers have a significant impact on the observed characteristics, i.e. the current is injection-limited. It can be noted that the geometry of the nanofiber devices differs somewhat from the parallel-plate geometry assumed in eq. 6.10. However, using the theory for the in-plane SCL current in thin layers, which predicts the current to depend inversely on the device length squared[202], would lead to the same conclusion regarding injection-limited current.

It should also be noted that hole and electron mobilities in general are different. In fig. 6.6(b) all extracted mobility values have been plotted on the same graph irrespective of the assumed carrier type, which is expected to differ between the different contact metals as discussed shortly. However, no clear dependence on contact material (and thus carrier type) is seen, which indicates that the calculated values could be significantly below their actual mobility values. The extracted values thus only indicate a minimum mobility of $3 \cdot 10^{-1}$ cm^2/Vs. This is in reasonable agreement with a previous report of a hole mobility of 10^{-1} cm^2/Vs measured on a p6P thin film in a FET configuration[208], however, in which contact barriers were also believed to reduce the extracted mobility below its intrinsic value.

Next, the influence of the contact material on the electrical characteristics was investigated. Fig. 6.7(b) shows typical characteristics of devices with different contact metals, where a clear dependence of current density on contact metal is seen.

The work functions of the contact metals are: Al: 4.3 eV, Cr: 4.5 eV, and Au: 5.1 eV[206], while the p6P electron affinity and ionization energy are 2.9 eV and 6.0 eV, respectively[99]. These are also shown in fig. 6.7(a). Au is expected to have the lowest injection barrier of $\sim$ 0.9 eV towards hole injection. This is in agreement with the relatively high current density at low voltages of the gold contacted device. Cr has a large barrier both towards electron ($\sim$ 1.6 eV) and hole injection ($\sim$ 1.5 eV), which agrees with the observation of a relatively low current density. Al has a lower barrier for electron injection ($\sim$ 1.4 eV) and a higher barrier for hole injection ($\sim$ 1.7 eV) than Cr. The higher current density of the Al contacted device compared to the device with Cr contacts thus indicates that the current in the Al device is carried by electrons. However, as the exact interface structures and properties are unknown, this claim would have to be verified for example by examining the transconductance properties in a FET configuration.

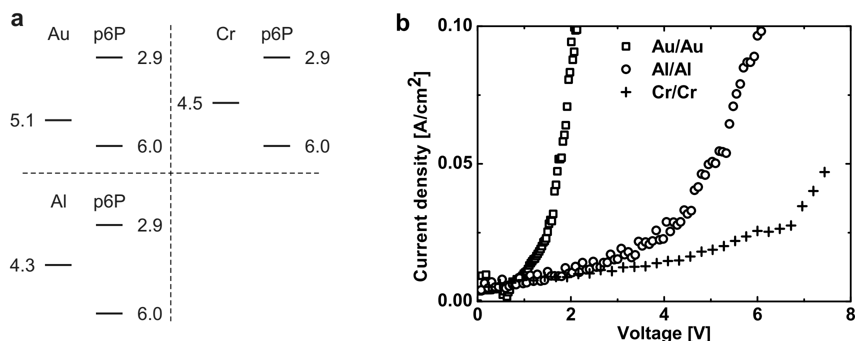

Figure 6.7: (a) The relevant energy level positions in p6P and Au, Cr, and Al (in eV). (b) $J-V$ characteristics of devices with three different contact metals: Au/Au, Al/Al, and Cr/Cr. The voltage was swept from 0 V.

Despite the appearance of the $J-V$ characteristics varying somewhat between in principle similar samples, each sample (with the same anode and cathode material) would typically exhibit symmetric characteristics as the example in fig. 6.8(a) shows. A few working devices with different anode and cathode material were also realized as shown in fig. 3.18. Fig. 6.8 shows both the forward (Au anode) and reverse (Au cathode) characteristics of one of the devices with Ti and Au electrodes.

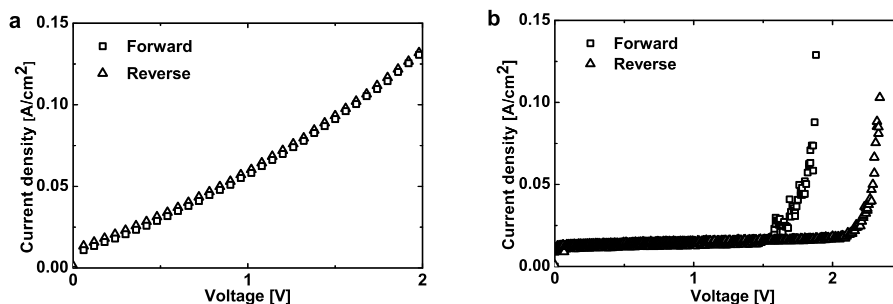

Figure 6.8: (a) $J-V$ characteristics of a device with Au/Au electrodes. (b) $J-V$ characteristics of a device with Au/Ti electrodes. The voltage was swept from 0 V in all measurements.

Fig. 6.8(b) shows that different electrode metals appear to cause asymmetric $J-V$ characteristics with the 'onset' voltage significantly larger under reverse bias compared to forward bias. However, the functional form of

the characteristics differs somewhat from that in fig. 6.8(a) indicating that additional, unknown effects are contributing and a direct comparison can therefore not be made. The asymmetric characteristics nonetheless indicate that the properties of the two contacts are different and therefore that the method for fabricating hetero-contacts as outlined in fig. 3.18 does allow the realization of contacts with different injection properties. Although Au electrodes must be expected to inject holes and Ti presumably is an electron injecting material, no electroluminescence was observed from these Ti/Au contacted devices. However, the difference in barrier heights is probably too large causing only hole injection. Establishing electroluminescence would require more balanced electron and hole currents.

In both fig. 6.7 and 6.8, a DC current off-set can be observed. By sweeping the bias voltage at different rates, it was observed that the value of this DC off-set is proportional to voltage sweep rate. This indicates that the off-set is caused by a capacitive effect. Measurements made without having a sample mounted showed that this capacitive load primarily originates from the sample itself, while measurements on a sample with an empty gap (i.e. with no nanofiber present) exhibited a similar off-set. The sample geometry includes two relatively large metal electrodes and it is presumed that these are causing this capacitive load.

6.2.2 Temperature Dependence of the Injection Current

The investigations show that out of the investigated contact metals, Au has the highest injection rate. In order to investigate the injection process in more detail, current-voltage ($I-V$) characteristics were obtained at different temperatures. These measurements were performed by mounting the sample in a small compartment with electrical feed-troughs where the temperature could be controlled either by lowering the sample into a nitrogen cryostat or by heating it with an attached resistor through Joule heating. Fig. 6.9(a) shows $I-V$ characteristics of an individual, gold contacted nanofiber measured at three different temperatures. As expected for the injection-limited case, the current decreases with decreasing temperature. Fig. 6.9(b) shows the current at a bias voltage of 3 volts versus reciprocal temperature. The injected current has a clear temperature dependence at higher temperatures and stabilizes below $\sim$ 200 K.

The temperature dependent measurements have been analyzed with both the models presented in the previous section (eq. 6.4 and 6.5). Considering a barrier height ϕ_h equal to the difference between the gold work function (5.1 eV) and the p6P ionization energy (6.0 eV) and considering injection into a single energy level, both models predict similar strong temperature dependencies of the injected current. The full squares in fig. 6.9(b) show the predictions from the Arkhipov model[200] (eq. 6.5). Apparently the actual temperature dependence is weaker than this prediction. A possible

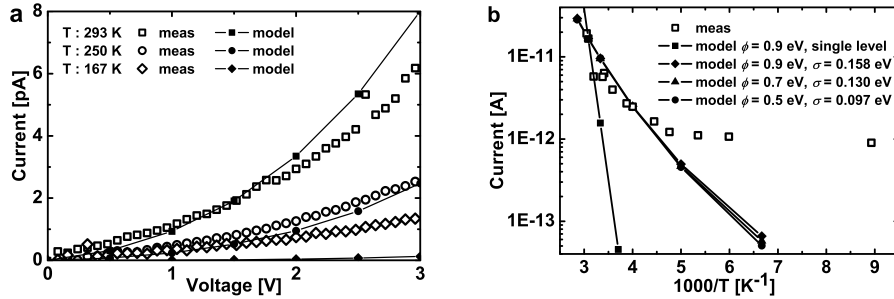

Figure 6.9: (a) $I - V$ characteristics characteristics measured at three different temperatures (open symbols). The filled symbols show model calculations as described in the text with $(\phi_h,\, \sigma) = (0.7 \text{ eV},\, 0.13 \text{ eV})$ (b) The current measured at a bias voltage of 3 volts versus reciprocal temperature (open squares). The filled symbols show model calculations with different model parameters. The capacitive off-set of the order of 1 pA caused by the finite sweeping rate has been subtracted here.

explanation for this deviation could be a barrier lowering due to an interface dipole layer, which has been disregarded in these calculations. As discussed previously, a significant interface dipole is however not expected with the present device fabrication environment[193]. A second possible cause of the comparably low temperature dependence could be that injection does not occur into a single energy level but rather into a distribution of states[200]. Since the barrier height is unknown, the injection current has been modelled assuming different values of barrier height: 0.9 eV, 0.7 eV, and 0.5 eV. The width of the energy distribution has then been modified until a reasonable agreement between injected current and temperature (in the interval above $\sim$ 200 K) was observed. These three model predictions are shown in fig. 6.9(b) (with $\epsilon_r = 1.9$[87], $N_0 = 1.7 \cdot 10^{21}$ cm^{-3}, $\gamma = (3 \text{ Å})^{-1}$, and $a = 5.6$ Å).

The model describes a dependence of the injected current on temperature that is weaker when the carriers are injected into a distribution of states rather than a single energy level: the wider the distribution, the weaker the temperature dependence. Qualitatively, this could explain part of the observed temperature dependence: that the organic layer close to the interface has a disorder induced level broadening that causes more carriers than expected to be injected at lower temperatures. This disorder could be created during the electrode deposition process where hot gold atoms or clusters collide against the organic material. It has been shown that this process can cause a less 'sharp' interface[196]. However, since neither the exact barrier

height nor the width of the energy distribution is known, it is not possible to make an exact estimate. All three model calculations give very similar results that only deviate slightly at low temperatures where the model is not appropriate at all. Fig. 6.9(a) includes the calculated $I - V$ characteristics at three different temperatures together with the measured $I - V$ curves. In these model calculations $(\phi_h, \sigma) = (0.7\text{ eV}, 0.13\text{ eV})$ have been used. A decent agreement is observed at high temperatures although the model predicts the current to increase steeper than observed. At low temperatures the model significantly underestimates the injected current as is also evident from fig. 6.9(b). A similar temperature dependence has also been observed experimentally on p6P films[209] even with the temperature dependence reversing sign at low temperatures. It thus appears that some additional factor is in play causing a high current injection even at low temperatures.

It should be noted that in the nanofiber device geometry the exact electric field distribution is not obvious at all. For simplicity it has here been assumed that the electric field was equal to the applied voltage divided by gap distance. However, strictly speaking this only applies to a geometry relating that of a parallel-plate capacitor. For a more accurate determination of the field, a simulation of the field distribution in this device architecture is necessary, and this may influence the agreement between the model and the measured data.

6.2.3 Influence of UV Light Exposure on Current Flow

As described in chapter 2, the nanofibers have photoluminescent properties, i.e. exposure to UV light causes the generation of excitons. It is thus possible to optically excite carriers in the nanofiber thereby potentially altering its electrical properties. This has been investigated experimentally by measuring the $I - V$ characteristics of a nanofiber device with Au contacts while exposing it to UV light at different intensities.

The UV light exposure of a nanofiber device was accomplished under an Olympus BX51 microscope that had a 100 W high-pressure mercury lamp attached. The light was filtered through an Olympus U-MWU2 fluorescence mirror unit to select the wavelength at 365 nm, while the intensity was varied by changing between different microscope objectives and by attenuating the intensity with one or more neutral density filters. During exposure, electrical characterization was performed with a set-up similar to the one described previously. The UV light intensity was measured with a UVX radiometer and a UVX-36 sensor calibrated for a wavelength of 365 nm.

Fig. 6.10(a) shows five $I - V$ curves acquired in succession (measurements 24 through 28 on this particular sample); the first (M24) in the dark, the next three at different light intensities, and finally the fifth in the dark again. The current is seen to depend on the light intensity - most clearly observed at higher voltages: the higher the light intensity, the larger the current

flow. The inset of fig. 6.10(a) shows the current at an applied voltage of 2 V (not corrected for the capacitive off-set). At zero light intensity (M24), the current is $\sim$ 7.4 pA, while at 53 mW/cm^2 (M25) it has risen to $\sim$ 8.9 pA corresponding to a 20 % increase (or 25 % if a $\sim$ 1.3 pA off-set is subtracted). Although the curves appear to have similar functional forms, which could indicate that the light simply causes the current to increase by a constant factor, a close examination reveals that the curve form is changed slightly. Fig. 6.10(b) shows the difference between a 'light' and a 'dark' measurement, from which it is seen that the influence from the light is stronger at higher voltages.

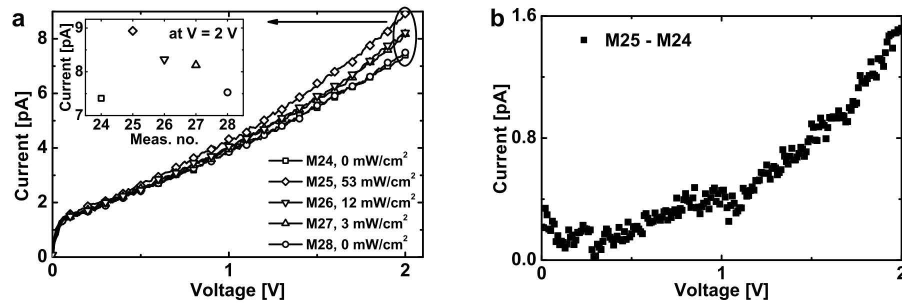

Figure 6.10: (a) Five $I-V$ characteristics measured successively with different exposure levels of UV light intensity (values given in the legend). Inset shows the current at 2 V determined from a linear fit between 1.8 and 2.0 V to reduce the influence from noise. (b) The difference between curves M25 and M24, corresponding to the additional current caused by UV light exposure with an intensity of 53 mW/cm^2.

A clear effect from the UV light exposure can be observed, indicating that more free carriers become available thus causing a higher current. The increased number of free carriers must be due either to a bulk effect that generates free carriers in the nanofiber or to a contact effect that causes a higher injection rate. A bulk effect that could lead to a higher current is the generation of photo induced carriers. UV light exposure generates excitons, i.e. interacting electron-hole pairs spatially located on individual molecules. For these excitons to contribute to the current, they must be dissociated to form free carriers, assisted for example by an applied electric field. The dissociation probability is field dependent[210], which would lead to a stronger-than-linear increase with voltage of the light-induced contribution to the current. A second possibility is that the extra current is caused by a contact effect that could be due to an internal photoemission process enabling more carriers to surmount the injection barrier. This must also be

expected to be non-linear with voltage due to the field-dependent barrier lowering. The exact cause of the light-induced increase in not known. One way of distinguishing between these effects is to use different photon energies. Exciton generation requires a photon energy comparable to or larger than the bandgap, whereas internal photoemission also occurs at sub-gap photon energies[211]. If low-energy photons would have a similar influence, this would indicate an internal photoemission process.

A second observation from the UV light exposure experiments is a clear degradation effect. After exposure to UV light, the current is reduced seemingly with the greatest effect at the first measurements. Fig. 6.11 illustrates this effect.

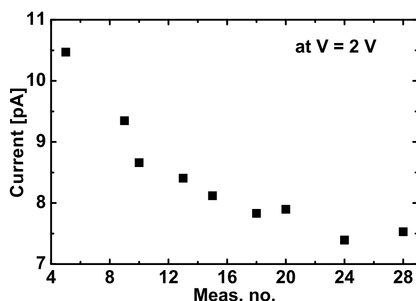

Figure 6.11: The 'dark' current measured at 2 V. Between these measurements, one or several exposures of UV light have been made. (Measurements 1 through 4 were made at lower voltages to determine appropriate settings for the current preamplifier. No degradation was observed here.)

Fig. 6.11 shows the current at a voltage of 2 V for a number of measurements, all acquired in the dark, however, with the sample having been exposed to UV light in between these measurements. Although not completely monotonous, a clear tendency towards a reduced current is observed. Apparently, exposure to UV light has a degrading effect that reduces the current. A similar degradation has been observed in other nanofiber measurements in which no UV exposure was made, however, not at this rate.

Bleaching experiments, where p6P fibers were subjected to high-intensity UV light, have been shown to have a significant degrading effect on the photoluminescence output[212]. This involved at least three processes: intramolecular configuration change, photo-oxidation, and removal of material. The reduction in current observed in fig. 6.11 suggests that similar processes are occurring here. One way of avoiding the oxidation processes would be to encapsulate the nanofiber, which would then presumably lower the influence from degradation processes[212].

6.2.4 Additional Experiments

A few additional experiments on p6P nanofibers were made and will briefly be introduced here. Strain experiments on a gold contacted nanofiber, similar to the experiments performed on MWCNTs as described in chapter 5, showed that the $I-V$ characteristics are strain independent. This is as expected, since the current is injection-limited and the contact properties are not assumed to be affected here. However, it was later realized that the bulk conductance properties are not expected to be much affected by strain either. Theoretical calculations on a similar molecule[93] indicate that the transfer integral t (see eq. 2.12) even in a cofacial configuration is not expected to decrease much upon the application of modest levels of strain.

Electrostatic force microscopy (EFM)[52] was tested to determine if this method is suitable for investigating the spatial potential distribution of a biased nanofiber device. The present device geometry is less suited for such investigations, and no quantitative conclusions could be extracted. An in-depth discussion of various aspects of EFM and the results on nanofiber devices can be found in the master thesis of Casper Hyttel Clausen[213].

6.3 Summary and Outlook

The shadow mask method detailed in chapter 3 has been used to electrically contact individual p6P nanofibers. An investigation of a number of devices showed that their electrical properties are determined primarily by the contact properties and that the nanofiber bulk has less influence. In relation to electroluminescence, this means that appropriate anode and cathode materials must be found, which facilitates efficient injection of holes and electrons, respectively. Different contact metals were tested with gold showing the most efficient carrier (hole) injection properties. A suitable cathode material for efficient electron injection is still needed. The shadow mask method also allows a nanofiber to be contacted with different cathode and anode material, which causes asymmetric $I-V$ characteristics. However, as no appropriate cathode material is yet found, no electroluminescence were observed from these devices.

The injection properties from a gold electrode into a p6P nanofiber was investigated in more detail by measuring how the $I-V$ characteristics depend on temperature. The injection current shows a weaker temperature dependence than what would be anticipated from a simple estimation of barrier height based on the electrode work function and p6P energy levels. A theoretical model that considers charge injection as carrier hopping into a localized state followed by a diffusive escape into the bulk shows that this weak temperature dependence can be explained if one considers injection into a distribution of states rather than a single energy level. This rather simple model is partly in agreement with the measured data, in particular at

temperatures above ~ 200 K, and suggests that some disorder related level broadening is present in the organic material near the electrode interface. This implies that although the organic nanofiber is near-perfect crystalline, an increased-disorder region exists near the electrode interface. This could for instance be due to the load during electrode deposition where hot metal atoms or clusters collide with the organic material. In that case, creating a good contact to organic nanofibers may be far from straight-forward, requiring a high degree of control of the electrode deposition process. Decreasing the metal evaporation rate could be one method of obtaining a better interface. Another option could be to attach the electrodes by some other means than evaporation, e.g. by prefabricating the electrodes on a carrier substrate and placing the organic crystal on top. It should be pointed out, that a well-defined, sharp interface for some applications may not be the optimal situation since level broadening *increases* injection.

The influence from UV light exposure on the electrical properties was also investigated. This showed that in particular at voltages above ~ 1 V a notable increase in current could be observed during light exposure. This must be attributed either to an increased injection or the generation of free carriers in the bulk. In addition, these experiments demonstrated a clear degradation effect that presumably is caused partly by photo-oxidation.

Based on the investigations made here, a number of future studies can be suggested. The realization of an electroluminescent device requires the identification of a suitable cathode material. One possibility would be to test low-work function metals such as Mg (work function: 3.66 eV) or Sm (work function: 2.7 eV)[206]. These should possess a low electron injection barrier. However, both are quite reactive and oxidize rapidly under ambient conditions. They would therefore require some kind of encapsulation to avoid oxidation. Another option would be to use an organic material for the contact. This could for example be BPhen[214], which is an electron transporting material that at the same time has poor hole conduction properties. This and similar materials can be vacuum deposited by thermal evaporation. During this project, a vacuum evaporation system for deposition of such materials was built, with Henrik Henrichsen performing the greater part of the actual construction. This evaporation system is now operational, and the initial characterization experiments demonstrate the ability to deposit a thin film of BPhen, which electrical measurements showed to be conducting. A thorough description of the BPhen deposition investigations can be found in the master thesis of Daniel Engstrøm[215].

Another issue to be dealt with is that of fabricating contacts of different materials. Although the extended shadow mask method is functional, the required manipulation is time consuming and the yield is low, which makes it less suitable for fabricating larger number of devices. Another possibility in terms of realizing contacts to fragile nanostructures is stenciling, which uses a perforated membrane as a shadow mask[216]. This could presumably

allow deposition of different anode and cathode materials by tilting the stencil mask to different angles during the two deposition rounds similar to the principle used for Josephson junctions[217]. A photolithograhy mask has been designed, and a process recipe has been developed, and the first experimental tests are now underway.

Chapter 7

Conclusions

Many nanostructures exhibit intriguing intrinsic properties that point towards their use for technological purposes, i.e. that such structures could be used as nanocomponents. One way of realizing this is to integrate such structures in microsystems to create the necessary interface. Utilization of *individual* nanocomponents calls for the ability to position these with a high accuracy relative to a microsystem and to fabricate appropriate contacts. Such integration requires the study of several interlinked aspects, for example whether the integration process compromise vital component properties or how the contacts influence the device properties. Thus, the development of a nanocomponent based device requires a consideration of the device as a whole, i.e. the nanocomponent(s), the function, and the integration method. During this project, two different types of components and two different integration methods have been investigated with the goal of evaluating two different nanocomponent based devices.

The first type of component is the multi-walled carbon nanotube, which is mechanically and chemically robust and which can potentially by fabricated in-situ, i.e. directly at the desired position in the microsystem. This enables the possible use of a number of different integration methods. The second component type is a much more fragile organic nanofiber consisting of *para*-hexaphenylene (p6P) molecules in a crystal structure. The fragility of such a molecular crystal inhibits the use of several integration methods.

Mechanical manipulation can be used for component integration as it can facilitate accurate positioning of nanocomponents in prefabricated microsystems. This is advantageous for example with 3-D microsystems or with components that cannot endure postprocessing. Mechanical manipulation can be divided into two categories: 2-D and 3-D. Whereas 2-D manipulation is typically used to investigate properties of nanostructures and their interaction with a supporting substrate, 3-D manipulation is technologically more relevant as a prototyping method for nanocomponent positioning typically using adhesive surface forces to perform pick-and-place operations.

AFM based 2-D manipulation has been used to investigate mechanical properties of p6P nanofibers and their ability to be moved along a surface. The nanofibers rupture at a shear stress of $\sim$ 20 MPa, while their Young's modulus is $\sim$ 0.65 GPa. Small pieces of nanofibers can be translated along a surface with a low-adhesion coating, however, on non-coated surfaces this is not possible due to strong adhesive forces.

A system for 3-D manipulation has been constructed based on an optical microscope for observation and piezoelectric actuators for tool motion. This allows manipulation of micro- and nanostructures with the lower size limit primarily set by the microscope. Different manipulation tools and strategies were evaluated, and 3-D manipulation of both robust carbon nanotubes and fragile organic nanofibers was demonstrated. To avoid the destruction of the organic nanofibers during manipulation, a special manipulation 'workbench' consisting of a large number of closely spaced, vertical carbon nanotubes was used. In addition, a method, based on mechanical manipulation of silicon wires with diameters of a few hundred nanometers for local shadow masks during electrode deposition, was used to contact different types of nanocomponents. In conclusion, the method was shown to be versatile and capable of contacting very different nanocomponents.

In-situ growth is a promising method for *parallel* fabrication of carbon nanotube devices as required for high-volume manufacturing. This requires the development and realization of a suitable microsystem with appropriately positioned catalyst particles for determining the nanotube positions. In addition, the growth direction must be controlled to facilitate growth between two electrodes by appropriate design of the microsystem. In this project, a standard cleanroom compatible process has been developed that uses a combination of photolithography and electron beam lithography to define the patterns for microsystem and catalyst material, respectively. The method of electric field guided growth was implemented to try to achieve lateral growth between electrodes.

One difficulty lies in fabricating a microsystem with integrated catalyst particles, here Ni. In most cleanroom laboratories and foundries with different silicon microsystem projects, Ni can potentially contaminate some of the necessary processing equipment. The Ni therefore either has to be deposited at an early stage and then encapsulated, or be deposited at a much later stage after all other processing has been finalized. In collaboration with Kjetil Gjerde, three different process recipes have been developed and tested. All three were found to be successful in protecting the equipment against Ni contamination but only partially successful in producing the expected device result. Based on these investigations, a fourth process recipe was developed, where the catalyst material patterning and deposition are performed as the final steps. Initial investigations of this recipe showed promising results, however, a few complicating factors that require additional optimization were encountered.

A chemical vapor deposition system for nanotube growth has been constructed. This consists of a vacuum chamber with a gas supply system that allows the flow rate of three gases: acetylene, methane, and hydrogen to be controlled independently. A heatable sample stage supplies the energy, and a special sample holder enables the application of an electric field during growth. Initial optimization experiments were performed to determine suitable growth parameters as described in section 4.2. These parameters resulted in nanotube-like structures as observed with SEM. Growth of individual nanotube-like structures from catalyst particles was partly successful although the resulting structures were shorter and less regular than expected. Electric field guided growth was attempted, but these experiments were unsuccessful. When the chips were contacted with macroscopic electrodes in the growth chamber, an electric discharge caused the destruction of the microscopic electrodes on the chips.

A carbon nanotube integrated in a microcantilever system can potentially function as a strain gauge. This concept has been investigated experimentally for the case of MWCNTs. A suitable microcantilever system has been designed and realized by conventional microfabrication techniques. Individual MWCNTs were integrated by use of the silicon wire shadow mask method and their electromechanical properties were investigated by probing their electrical characteristics while deflecting the cantilever to induce mechanical strain. These results were then compared to the performance of a cantilever system with a silicon piezoresistor[146]. In one fourth of the fabricated MWCNT devices, good electrical contact was established as assessed from the initial low-bias current-voltage characteristics. However, only very few devices showed gauge factors comparable to or larger than that of a silicon piezoresistor (which has a gauge factor of ~ 50), while a large proportion of the devices showed none or very limited response. Although a theoretical model predicts that MWCNTs should have lower gauge factors than SWCNTs (which can have gauge factors up to ~ 1000), this can not account for the results. One explanation can be structural defects that cause a current path different from the idealized case where the outermost shell carries most current. If a significant number of shells are carrying the current, and some of these shells are not stretched or are non-responsive, this could effectively 'short-circuit' a possible larger response in an outer shell. This would suggest the use of MWCNTs with fewer defects which, however, require synthesis methods not compatible with in-situ fabrication like laser ablation or arc-discharge.

A theoretical comparison of the noise properties of two different Si piezoresistors and a MWCNT integrated in cantilevers was performed. This was done in order to evaluate if the high levels of $1/f$ noise observed in carbon nanotubes[80] would further impede their application as sensors. The Si resistors were chosen so one had dimensions of several tens of μm as in [146], whereas the other was in the 100 nm range, i.e. of comparable size

to a large MWCNT. Three noise sources were considered: thermal electrical (Johnson) noise, $1/f$ noise, and thermal vibrational noise of the cantilever. At low frequencies, the most significant noise source is the $1/f$ noise as expected, however, much more pronounced in the both the small Si resistor and the MWCNT than in the large Si resistor ($\sim$ five and six orders of magnitude larger, respectively). Thus, a small sensor will exhibit a significant $1/f$ noise irrespective of material. At larger frequencies, the $1/f$ noise becomes less pronounced, however, for the MWCNT it remains the dominating noise source up to the GHz range in the considered example. This also limits the usefulness of nanotubes or any other nanostructures for sensitive sensing applications unless the gauge factors are orders of magnitude higher than in silicon.

Individual p6P nanofibers were contacted using the shadow mask method and their electrical properties were investigated. This was done to investigate charge injection and transport properties with the ultimate goal of realizing efficient injection of both carriers types and, trough their recombination, electroluminescence, i.e. an organic nanofiber based light-emitting device. Different models for charge injection and transport were reviewed and used in the analysis of current-voltage characteristics obtained from nanofiber devices. This analysis showed that using the contact metals Au, Al, and Cr all result in an injection-limited current, i.e. that significant contact barriers are the main current limiting factor. Based on these measurements, a *minimum* value of the carrier mobility of $3 \cdot 10^{-1}$ cm^2/Vs was found, however, it should be noted that this could be well below the actual mobility. The different metals each have different injection properties. Au has a comparably low ($\sim$ 0.9 eV) hole injection barrier, which causes comparably higher injected current densities than with the other contact metals. Devices with different anode and cathode material showed asymmetric current-voltage characteristics as expected, but no electroluminescence was observed - presumably due to the large mismatch between hole and electron injection barriers.

The injection properties were studied with low temperature measurements. As expected, the injection current decreases when the temperature is lowered. However, the temperature dependence of the current is weaker than what would be anticipated from a simple estimation of injection barrier based on electrode work function and p6P energy levels. A theoretical model, that considers injection into a localized state followed by the carrier's diffusive escape into the bulk, shows that the weak temperature dependence can be explained if one considers injection into a distribution of states rather than a single energy level. This implies that although the nanofiber initially is near-crystalline, a region with an increased energetic level broadening exists near the interface towards the electrode or the nanofiber crystal structure is no longer intact. Level broadening near the interface could be created during the electrode deposition process where hot metal atoms or clusters

impinge on the nanofiber surface. This is expected to create a region with an increased disorder. Creating a suitable metal contact thus requires a high degree of control over the electrode deposition process.

The influence of UV light exposure on the electrical characteristics has also been studied. Compared to conductance measurements in the dark, UV exposure causes a larger current to flow: the higher the light intensity, the larger the current. This is attributed either to the generation of free carriers in the nanofiber bulk, or to an enhanced injection due to internal photoemission.

7.1 Outlook

Mechanical manipulation is a robust, flexible, and straight-forward method for pick-and-place operations. With the 'workbench' used in the 3-D manipulation of organic nanofibers it is now possible to manipulate even very fragile structures. A further optimization of this technique could involve the development of better tools for example with functionalized surfaces for easier component release. This is within the scope both of two present EU projects: Nanorac[1] and Nanohand[2], both with participation of the Nanointegration group at MIC, DTU.

In-situ growth of carbon nanotubes is a fast process that can provide parallel nanotube integration on a wafer scale. Growth of nanotubes between electrodes on microcantilevers can presumably be obtained and with a further optimization of the developed process recipe, it is expected that microsystems with appropriate catalyst particles can be fabricated with an acceptable yield. The nanotube growth system is operational and working growth parameters are established. A further optimization of these must be expected to enable fabrication of nanotubes with a better quality. The problem of electric discharges destroying the electrodes must be solved on a trial-and-error basis to locate and eliminate the cause.

The use of MWCNT strain gauges as deflection sensors in a microcantilever system is significantly hindered by a number of factors. Parallel fabrication requires that for example the in-situ growth method is optimized significantly. The experimental investigations showed a low yield of responsive MWCNT. As this is partly attributed to intrinsic properties (defects), this can only be remedied by the fabrication of high-quality MWCNTs. Still, the yield must be expected to be low compared to microfabricated Si piezoresistors. In addition, the noise properties of MWCNTs constitutes a further obstacle that is difficult to overcome. All in all, the outlook for this is not bright.

In contrast, the concept of organic nanofiber-based LEDs appear more

[1] `http://www.amir.uni-oldenburg.de/en/12603.html`
[2] `http://www.nanohand.eu/`

promising. Although no electroluminescence was observed, the obtained results suggest a number of further studies towards this goal. Organic contacts should be tested - in particular in the search of a suitable cathode material. More efficient contact methods such as nanostenciling should be investigated as these would enable a more efficient device fabrication.

Appendix A

List of Publications

This list is ordered chronologically by date of submission.

- S. Dohn, J. Kjelstrup-Hansen, D. N. Madsen, K. Mølhave, and P. Bøggild *Multi-walled carbon nanotubes integrated in microcantilevers for application of tensile strain* Ultramicroscopy, 2005, 105, 1-4, pp. 209-214

- J. Kjelstrup-Hansen , H. H. Henrichsen, P. Bøggild, and H.-G. Rubahn *Electrical properties of a single p-hexaphenylene nanofiber* Thin Solid Films, 2006, 515, 2, pp. 827-830

- J. Kjelstrup-Hansen, P. Bøggild, J. Hvam, A. Majcher, and H.-G. Rubahn *Micromanipulation of organic nanofibers for blue light emitting microstructures* Physica Status Solidi (a), 2006, 203, 6, pp. 1459-1463

- K. Gjerde, M. F. Mora, J. Kjelstrup-Hansen, T. Schurmann, L. Gammelgaard, M. Aono, K. B. K. Teo, W. I. Milne, and P. Bøggild *Integrating Nanotubes into Microsystems with Electron Beam Lithography and In Situ Catalytically Activated Growth* Physica Status Solidi (a), 2006, 203, 6, pp. 1094-1099

- J. Kjelstrup-Hansen, S. Dohn, D. N. Madsen, K. Mølhave, and P. Bøggild *Versatile Method for Manipulating and Contacting Nanowires* Journal of Nanoscience and Nanotechnology, 2006, 6, 7, pp. 1995-1999

- J. Kjelstrup-Hansen, O. Hansen, H.-G. Rubahn, and P. Bøggild *Mechanical Properties of Organic Nanofibers* Small, 2006, 2, 5, pp. 660-666

- K. Gjerde, J. Kjelstrup-Hansen, C. H. Clausen, K. B. K. Teo, W. I. Milne, H.-G. Rubahn, and P. Bøggild *Carbon nanotube forests: a non-stick workbench for nanomanipulation* Nanotechnology, 2006, 17, 19, pp. 4917-4922

- P. Bøggild, D. H. Petersen, J. Kjelstrup-Hansen, K. Mølhave, K. N. Andersen, and Ö. Sardan *Microfabricated tools for pick-and-place of nanoscale components* Proceedings of IFAC Mechatronics 2006, *submitted*

- J. Kjelstrup-Hansen , P. Bøggild, and H.-G. Rubahn *Charge Injection and Transport in Organic Nanofibers* Journal of Physics: Conference Series, 2006, *submitted*

- H. Henrichsen, J. Kjelstrup-Hansen, D. Engstrøm, C. H. Clausen, P. Bøggild, and H.-G. Rubahn *Electrical Conductivity of Organic Single-nanofiber Devices with Different Contact Materials*, 2006, *in preparation*

- J. Kjelstrup-Hansen, P. Bøggild, H. H. Henrichsen, J. Brewer, and H.-G. Rubahn *Device-oriented studies on electrical, optical and mechanical properties of individual organic nanofibers* in *New organic nanostructures for next generation devices*, eds. K. Al-Shamery, H.-G. Rubahn, and H. Sitter, 2006, Springer

Appendix B

Process Recipe

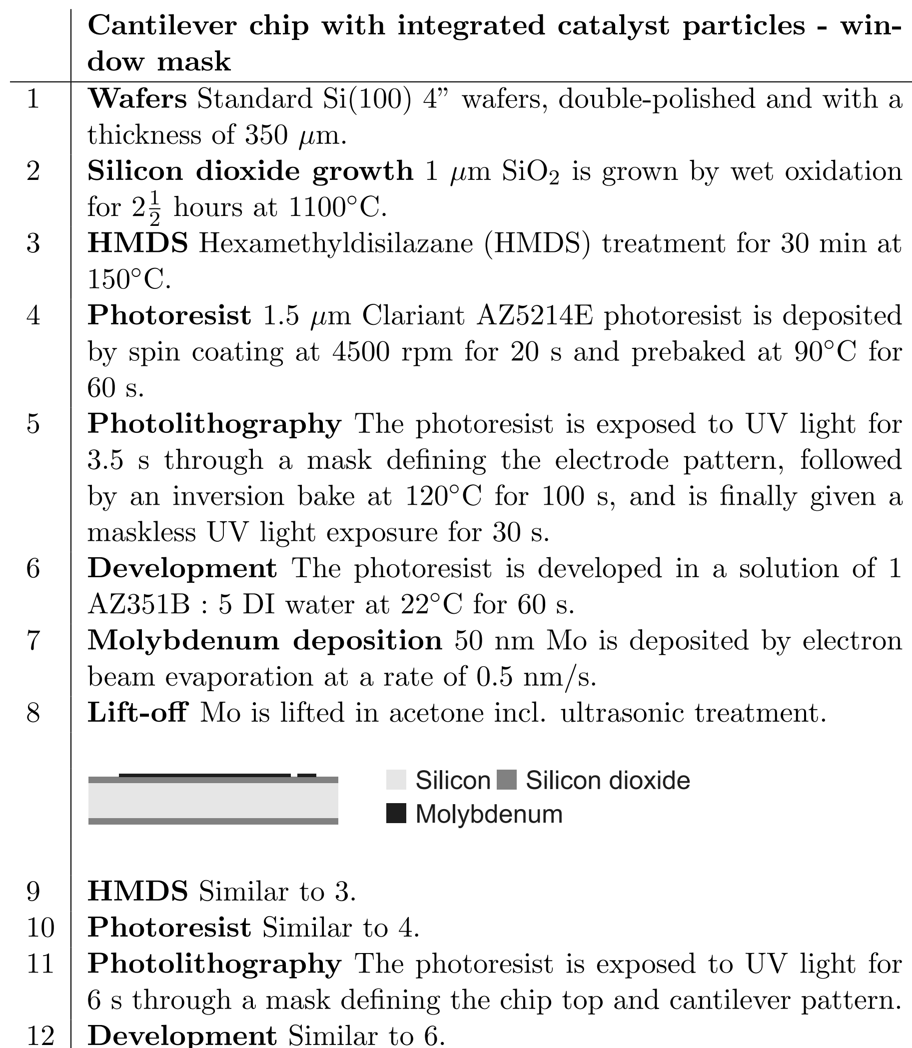

	Cantilever chip with integrated catalyst particles - window mask
1	**Wafers** Standard Si(100) 4” wafers, double-polished and with a thickness of 350 μm.
2	**Silicon dioxide growth** 1 μm SiO_2 is grown by wet oxidation for $2\frac{1}{2}$ hours at 1100°C.
3	**HMDS** Hexamethyldisilazane (HMDS) treatment for 30 min at 150°C.
4	**Photoresist** 1.5 μm Clariant AZ5214E photoresist is deposited by spin coating at 4500 rpm for 20 s and prebaked at 90°C for 60 s.
5	**Photolithography** The photoresist is exposed to UV light for 3.5 s through a mask defining the electrode pattern, followed by an inversion bake at 120°C for 100 s, and is finally given a maskless UV light exposure for 30 s.
6	**Development** The photoresist is developed in a solution of 1 AZ351B : 5 DI water at 22°C for 60 s.
7	**Molybdenum deposition** 50 nm Mo is deposited by electron beam evaporation at a rate of 0.5 nm/s.
8	**Lift-off** Mo is lifted in acetone incl. ultrasonic treatment.
	Silicon, Silicon dioxide, Molybdenum
9	**HMDS** Similar to 3.
10	**Photoresist** Similar to 4.
11	**Photolithography** The photoresist is exposed to UV light for 6 s through a mask defining the chip top and cantilever pattern.
12	**Development** Similar to 6.

Cantilever chip with integrated catalyst particles - window mask (continued)

13 **Silicon dioxide etch** The pattern is transferred to the silicon oxide layer by etching in BHF for 13 min.

14 **Photoresist strip** The resist is stripped in acetone.

15 **Silicon nitride deposition** 450 nm low-stress silicon nitride is deposited by PECVD on the wafer frontside at 20 W, 6 s (13.56 MHz)/20 W, 2 s (380 kHz), 650 mtorr, 1470 sccm N_2, 30 sccm SiH_4, and 30 sccm NH_4 for 39 min.

16 **Silicon nitride deposition** 150 nm low-stress silicon nitride is deposited by PECVD on the wafer backside at 20 W, 6 s (13.56 MHz)/20 W, 2 s (380 kHz), 650 mtorr, 1470 sccm N_2, 30 sccm SiH_4, and 30 sccm NH_4 for 13 min.

17 **HMDS** Similar to 3.

18 **Photoresist** Similar to 4 but on the wafer backside.

19 **Photolithography** The photoresist is exposed to UV light for 6 s through a mask defining the chip outline on the wafer backside.

20 **Silicon nitride etch** The backside pattern is transferred to the silicon nitride layer by reactive ion etching at 30 W, 80 mtorr, 40 sccm SF_6 and 8 sccm O_2 for 12 min.

21 **Photoresist strip** The photoresist is stripped in acetone.

22 **Bulk silicon etch** The chips are etched out and the cantilevers are released by KOH etching at 80°C for $4\frac{1}{2}$ h.

23 **Silicon nitride etch** The silicon nitride is removed by reactive ion etching with similar parameters as in 20 but for 36 min. (Alternatively, the silicon nitride could be removed in H_3PO_4 at 160°C for 30 min).

24 **HMDS** Similar to 3.

25 **Photoresist** 2.2 μm Clariant AZ5214E photoresist is deposited by spin coating at 2000 rpm for 20 s and prebaked at 90°C for 60 s.

26 **Photolithography** The photoresist is exposed to UV light for 14 s through a mask defining the window pattern.

27 **Development** Similar to 6.

	Cantilever chip with integrated catalyst particles - window mask (continued)
28	**Poly-silicon deposition** p-Si is deposited by sputtering in an Ar atmosphere at a pressure of 0.02 mbar and an RF power of 400 W for $5\frac{1}{2}$ min.
29	**Lift-off** p-Si is lifted in acetone.
	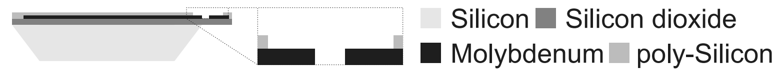
30	**Electron beam lithography resist** 100 nm ZEP-520A7 electron beam lithography resist is deposited by spin coating a solution of 1 ZEP 520A7 : 3 Anisole at 3000 RPM for 30 s and baking at 160°C for 10 min.
31	**Electron beam lithography** The catalyst particle pattern is transferred to the resist by electron beam lithography using an acceleration voltage of 100 kV and a dose of 600 μC/cm^2.
32	**Development** The photoresist is developed in ZEP N-50 developer for 90 s.
33	**Nickel deposition** 5 nm Ni is deposited by electron beam evaporation.
34	**Lift-off and Poly-silicon etch** Ni is lifted by dissolving both the resist and the p-Si layer in KOH at 80°C for 25 s.
	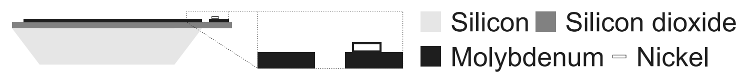

Bibliography

[1] S. Iijima, Nature **354**, 56 (1991).

[2] K. Hiruma *et al.*, Applied Physics Letters **59**, 431 (1991).

[3] M. Reches and E. Gazit, Science **300**, 625 (2003).

[4] F. Balzer and H.-G. Rubahn, Applied Physics Letters **79**, 3860 (2001).

[5] M. Bockrath *et al.*, Science **275**, 1922 (1997).

[6] S. J. Tans *et al.*, Nature **386**, 474 (1997).

[7] R. Martel, T. Schmidt, H. R. Shea, T. Hertel, and P. Avouris, Applied Physics Letters **73**, 2447 (1998).

[8] Y. Huang, X. Duan, Q. Wei, and C. M. Lieber, Science **291**, 630 (2001).

[9] M. Burghard, G. Duesberg, G. Philipp, J. Muster, and S. Roth, Advanced Materials **10**, 584 (1998).

[10] R. Krupke, F. Hennrich, H. v. Löhneysen, and M. M. Kappes, Science **301**, 344 (2003).

[11] P. Avouris *et al.*, Applied Surface Science **141**, 201 (1999).

[12] K. Mølhave, T. M. Hansen, D. N. Madsen, and P. Bøggild, Journal of Nanoscience and Nanotechnology **4**, 279 (2004).

[13] N. R. Franklin *et al.*, Applied Physics Letters **81**, 913 (2002).

[14] A. Ural, Y. Li, and H. Dai, Applied Physics Letters **81**, 3464 (2002).

[15] B. J. Ohlsson *et al.*, Applied Physics Letters **79**, 3335 (2001).

[16] S. J. Tans, R. M. Verschueren, and C. Dekker, Nature **393**, 49 (1998).

[17] X. Duan, Y. Huang, Y. Cui, J. Wang, and C. M. Lieber, Nature **409**, 66 (2001).

[18] J. Kong *et al.*, Science **287**, 622 (2000).

[19] D. J. Sirbuly *et al.*, Proceedings of the National Academy of Sciences of the United States of America **102**, 7800 (2005).

[20] M. S. Gudiksen, L. J. Lauhon, J. Wang, D. C. Smith, and C. M. Lieber, Nature **415**, 617 (2002).

[21] J. A. Misewich *et al.*, Science **200**, 783 (2003).

[22] Y. Huang, X. Duan, and C. M. Lieber, Small **1**, 142 (2005).

[23] F. Patolsky and C. M. Lieber, Materials Today **8**, 20 (2005).

[24] T. W. Tombler *et al.*, Nature **405**, 769 (2000).

[25] C. M. Lieber, Scientific American **285**, 59 (2001).

[26] J. Nygård, D. H. Cobden, M. Bockrath, P. L. McEuen, and P. E. Lindelof, Applied Physics A **69**, 297 (1999).

[27] R. H. Baughman, A. A. Zakhidov, and W. A. de Heer, Science **297**, 787 (2002).

[28] A. M. Morales and C. M. Lieber, Science **279**, 208 (1998).

[29] K. Hiruma *et al.*, Journal of Applied Physics **77**, 447 (1995).

[30] M. T. Björk *et al.*, Nano Letters **2**, 87 (2002).

[31] L. J. Lauhon, M. S. Gudiksen, D. Wang, and C. M. Lieber, Nature **420**, 57 (2002).

[32] J. Xiang *et al.*, Nature **441**, 489 (2006).

[33] Y. Xia *et al.*, Advanced Materials **15**, 353 (2003).

[34] M. R. Ghadiri, J. R. Granja, R. A. Milligan, D. E. McRee, and N. Khazanovich, Nature **366**, 324 (1993).

[35] F. Favier, E. C. Walter, M. P. Zach, T. Benter, and R. M. Penner, Science **293**, 2227 (2001).

[36] C. Z. Li, H. X. He, A. Bogozi, J. S. Bunch, and N. J. Tao, Applied Physics Letters **76**, 1333 (2000).

[37] F. Balzer and H.-G. Rubahn, Advanced Functional Materials **15**, 17 (2005).

[38] D. Qian, G. J. Wagner, W. K. Liu, M.-F. Yu, and R. S. Ruoff, Applied Mechanics Reviews **55**, 495 (2002).

[39] N. Hamada, S. Sawada, and A. Oshiyama, Physical Review Letters **68**, 1579 (1992).

[40] P. Avouris, J. Appenzeller, R. Martel, and S. J. Wind, Proceedings of the IEEE **91**, 1772 (2003).

[41] R. Saito, G. Dresselhaus, and M. S. Dresselhaus, *Physical Properties of Carbon Nanotubes* (Imperial College Press, 1998).

[42] M. S. Dresselhaus, G. Dresselhaus, and P. Avouris, *Carbon Nanotubes: Synthesis, Structure, Properties and Applications* (Springer, 2001).

[43] A. Thess *et al.*, Science **273**, 483 (1996).

[44] A. P. Graham *et al.*, Small **1**, 382 (2005).

[45] C. Zhou, J. Kong, and H. Dai, Physical Review Letters **84**, 5604 (2000).

[46] J. W. G. Wildöer, L. C. Venema, A. G. Rinzler, R. E. Smalley, and C. Dekker, Nature **391**, 59 (1998).

[47] T. W. Odom, J.-L. Huang, P. Kim, and C. M. Lieber, Nature **391**, 62 (1998).

[48] S. Frank, P. Poncharal, Z. L. Wang, and W. A. De Heer, Science **280**, 1744 (1998).

[49] S. Datta, *Electronic Transport in Mesoscopic Systems* (Cambridge University Press, 1995).

[50] P. L. McEuen and J.-Y. Park, MRS Bulletin **29**, 272 (2004).

[51] J. Kong *et al.*, Physical Review Letters **87**, 106801 (2001).

[52] A. Bachtold *et al.*, Physical Review Letters **84**, 6082 (2000).

[53] J.-Y. Park *et al.*, Nano Letters **4**, 517 (2004).

[54] Z. Yao, C. L. Kane, and C. Dekker, Physical Review Letters **84**, 2941 (2000).

[55] J. Appenzeller *et al.*, Physical Review Letters **89**, 126801 (2002).

[56] Y.-M. Lin, J. Appenzeller, J. Knoch, and P. Avouris, IEEE Transactions on Nanotechnology **4**, 481 (2005).

[57] H. Dai, E. Wong, and C. M. Lieber, Science **272**, 523 (1996).

[58] J.-C. Charlier and J.-P. Issi, Applied Physics A **67**, 79 (1998).

[59] P. G. Collins, M. S. Arnold, and P. Avouris, Science **292**, 706 (2001).

[60] B. Bourlon, C. Miko, L. Forro, D. C. Glattli, and A. Bachtold, Physical Review Letters **93**, 176806 (2004).

[61] L. Yang and J. Han, Physical Review Letters **85**, 154 (2000).

[62] A. Kleiner and S. Eggert, Physical Review B **63**, 073408 (2001).

[63] E. D. Minot *et al.*, Physical Review Letters **90**, 156401 (2003).

[64] J. Cao, Q. Wang, and H. Dai, Physical Review Letters **90**, 157601 (2003).

[65] A. Maiti, A. Svizhenko, and M. P. Anantram, Physical Review Letters **88**, 126805 (2002).

[66] C. Stampfer *et al.*, Nano Letters **6**, 233 (2006).

[67] D. S. Bethune *et al.*, Nature **363**, 605 (1993).

[68] K. B. K. Teo, C. Singh, M. Chhowalla, and W. I. Milne, *Catalytic Synthesis of Carbon Nanotubes and Nanofibers* in *Encyclopedia of Nanoscience and Nanotechnology* (American Scientific Publishers, 2004).

[69] J. Kong, H. T. Soh, A. M. Cassell, C. F. Quate, and H. Dai, Nature **395**, 878 (1998).

[70] J. Kong *et al.*, Applied Physics A **69**, 305 (1999).

[71] C. A. Bower, O. Zhou, W. Zhu, D. J. Werder, and S. Jin, Applied Physics Letters **77**, 2767 (2000).

[72] Y. Avigal and R. Kalish, Applied Physics Letters **78**, 2291 (2001).

[73] Y. Zhang *et al.*, Applied Physics Letters **79**, 3155 (2001).

[74] Y.-T. Jang, J.-H. Ahn, B.-K. Ju, and Y.-H. Lee, Solid State Communications **126**, 305 (2003).

[75] Z. F. Ren *et al.*, Applied Physics Letters **75**, 1086 (1999).

[76] K. B. K. Teo *et al.*, Nanotechnology **14**, 204 (2003).

[77] Y. Li *et al.*, Nano Letters **4**, 317 (2004).

[78] F. N. Hooge, Physics Letters A **29a**, 139 (1969).

[79] P. Dutta and P. M. Horn, Reviews of Modern Physics **53**, 497 (1981).

[80] P. G. Collins, M. S. Fuhrer, and A. Zettl, Applied Physics Letters **76** (2000).

[81] E. S. Snow, J. P. Novak, M. D. Lay, and F. K. Perkins, Applied Physics Letters **85**, 4172 (2004).

[82] Y.-M. Lin, J. Appenzeller, J. Knoch, Z. Chen, and P. Avouris, Nano Letters **6**, 930 (2006).

[83] R. Tarkiainen, L. Roschier, M. Ahlskog, M. Paalanen, and P. Hakonen, Physica E **28**, 57 (2005).

[84] P.-E. Roche, M. Kociak, A. Kasumov, B. Reulet, and H. Bouchiat, The European Physical Journal B **28**, 217 (2002).

[85] D. H. Reneker and I. Chun, Nanotechnology **7**, 216 (1996).

[86] M. Schiek *et al.*, Applied Physics Letters **86**, 153107 (2005).

[87] F. Balzer, V. G. Bordo, A. C. Simonsen, and H.-G. Rubahn, Physical Review B **67**, 115408 (2003).

[88] M. Klemenc, F. Meghdadi, S. Voss, and G. Leising, Synthetic Metals **85**, 1243 (1997).

[89] F. Quochi *et al.*, Applied Physics Letters **88**, 041106 (2006).

[90] S. Guha *et al.*, Physical Review Letters **82**, 3625 (1999).

[91] R. Resel, Thin Solid Films **433**, 1 (2003).

[92] R. Waser, *Nanoelectronics and Information Technology*, 2 ed. (Wiley-VCH, 2005).

[93] J.-L. Bredas, J. P. Calbert, D. A. da Silva Filho, and J. Cornil, Proceedings of the National Academy of Sciences of the United States of America **99**, 5804 (2002).

[94] P. Puschnig and C. Ambrosch-Draxl, Physical Review B **60**, 7891 (1999).

[95] J.-L. Bredas, D. Beljonne, V. Coropceanu, and J. Cornil, Chemical Reviews **104**, 4971 (2004).

[96] W. Warta and N. Karl, Physical Review B **32**, 1172 (1985).

[97] J. C. Scott, Journal of Vacuum Science and Technology A **21**, 521 (2003).

[98] I. G. Hill, A. Kahn, Z. G. Soos, and R. A. Pascal Jr., Chemical Physics Letters **327**, 181 (2000).

[99] N. Koch *et al.*, Advanced Functional Materials **11**, 51 (2001).

[100] K. Sakanoue, M. Motoda, M. Sugimoto, and S. Sakaki, Journal of Physical Chemistry A **103**, 5551 (1999).

[101] J.-L. Bredas *et al.*, Synthetic Metals **125**, 107 (2001).

[102] T. B. Lynge and T. G. Pedersen, Computational Materials Science **30**, 212 (2004).

[103] X.-Y. Li, X. S. Tang, and F.-C. He, Chemical Physics **248**, 137 (1999).

[104] M. N. Bussac, J. D. Picon, and L. Zuppiroli, Europhysics Letters **66**, 392 (2004).

[105] H. Yanagi and S. Okamoto, Applied Physics Letters **71**, 2563 (1997).

[106] F. Balzer *et al.*, IEEE Transactions on Nanotechnology **3**, 67 (2004).

[107] F. Balzer and H.-G. Rubahn, Surface Science **507-510**, 588 (2002).

[108] B. Bhushan, *Handbook of Nanotechnology* (Springer, 2004).

[109] T. J. Senden and C. J. Drummond, Colloids and Surfaces A: Physicochemical and Engineering Aspects **94**, 29 (1995).

[110] K. Mølhave, T. Wich, A. Kortschack, and P. Bøggild, Nanotechnology **17**, 2434 (2006).

[111] M. Sitti and H. Hashimoto, IEEE/ASME Transactions on Mechatronics **5**, 199 (2000).

[112] J. Israelachvili, *Intermolecular and Surface Forces* (Academic Press, 1992).

[113] P. Lambert, P. Letier, and A. Delchambre, Proceedings of the 2003 IEEE International Symposium on Assembly and Task Planning , 54 (2003).

[114] M. K. Chaudhury, T. Weaver, C. Y. Hui, and E. J. Kramer, Journal of Applied Physics **80**, 30 (1996).

[115] M.-F. Yu, T. Kowalewski, and R. S. Ruoff, Physical Review Letters **86**, 87 (2001).

[116] P. E. Sheehan and C. M. Lieber, Science **272**, 1158 (1996).

[117] D. M. Eigler and E. K. Schweizer, Nature **344**, 524 (1990).

[118] S.-W. Hla, Journal of Vacuum Science and Technology B **23**, 1351 (2005).

[119] R. M. Taylor II *et al.*, Proceedings of the IEEE Visualization Conference , 467 (1997).

[120] J. Cumings and A. Zettl, Science **289**, 5479 (2000).

[121] J. K. Luo, A. J. Flewitt, S. M. Spearing, N. A. Fleck, and W. I. Milne, Journal of Micromechanics and Microengineering **15**, 1294 (2005).

[122] P. Kim and C. Lieber, Science **286**, 2148 (1999).

[123] P. Bøggild, T. M. Hansen, C. Tanasa, and F. Grey, Nanotechnology **12**, 331 (2001).

[124] K. Mølhave and O. Hansen, Journal of Micromechanics and Microengineering **15**, 1265 (2005).

[125] S. Dohn, K. Mølhave, and P. Bøggild, Sensor Letters **3**, 300 (2005).

[126] P. Bøggild *et al.*, Proceedings of IFAC Mechatronics 2006 *submitted* (2006).

[127] D. N. Madsen *et al.*, Nano Letters **3**, 47 (2003).

[128] J. E. A. M. Van Den Meerakker, R. J. G. Elfrink, W. M. Weeda, and F. Roozeboom, Physica Status Solidi A **197**, 57 (2003).

[129] K. Gjerde *et al.*, Nanotechnology **17**, 4917 (2006).

[130] S.-W. Lee and W. M. Sigmund, Colloids and Surfaces A **204**, 43 (2002).

[131] H. Dai, J. H. Hafner, A. G. Rinzler, D. T. Colbert, and R. E. Smalley, Nature **384**, 147 (1996).

[132] M. R. Falvo *et al.*, Nature **389**, 582 (1997).

[133] M. R. Falvo *et al.*, Nature **397**, 236 (1999).

[134] E. W. Wong, P. E. Sheehan, and C. M. Lieber, Science **277**, 1971 (1997).

[135] D. A. Walters *et al.*, Applied Physics Letters **74**, 3803 (1999).

[136] S. De Franceschi *et al.*, Applied Physics Letters **83**, 344 (2003).

[137] K. A. Dick *et al.*, Nano Letters **5**, 761 (2005).

[138] T. W. Cornelius *et al.*, Nanotechnology **16**, S246 (2005).

[139] J. Villarrubia, Journal of Research of the National Institute of Standards and Technology **102**, 425 (1997).

[140] M. Guthold *et al.*, Biophysical Journal **87**, 4226 (2004).

[141] S. D. Senturia, *Microsystem Design* (Academic Publishers, 2001).

[142] L. D. Landau and E. M. Lifshitz*Theory of Elasticity, Course of Theoretical Physics* Vol. 7, 3 ed. (Butterworth-Heinemann, 1986).

[143] M. Yang, K. Wang, L. Ye, Y.-W. Mai, and J. Wu, Plastics, Rubber and Composites **32**, 21 (2003).

[144] P. J. de Pablo *et al.*, Applied Physics Letters **74**, 323 (1999).

[145] S. Dohn, J. Kjelstrup-Hansen, D. N. Madsen, K. Mølhave, and P. Bøggild, Ultramicroscopy **105**, 209 (2005).

[146] J. Thaysen, A. Boisen, O. Hansen, and S. Bouwstra, Sensors and Actuators A **83**, 47 (2000).

[147] C. L. Petersen, F. Grey, I. Shiraki, and S. Hasegawa, Applied Physics Letters **77**, 3782 (2000).

[148] M. Dimaki, *Dielectrophoretic Assembly of Carbon Nanotube Devices*, PhD thesis, Technical University of Denmark, 2004.

[149] Y.-S. Han, J.-K. Shin, and S.-T. Kim, Journal of Applied Physics **90**, 5731 (2001).

[150] C. Gau, C. L. Chan, S. H. Shiau, C. W. Liu, and S. H. Ting, 5th IEEE Conference on Nanotechnology **2**, 857 (2005).

[151] S. Huang, X. Cai, and J. Liu, Journal of the American Chemical Society **125**, 5636 (2003).

[152] T. M. Hansen, *Tools for Nanoscale Conductivity Measurements*, PhD thesis, Technical University of Denmark, 2003.

[153] K. B. K. Teo *et al.*, Applied Physics Letters **80**, 2011 (2002).

[154] A. M. Rao *et al.*, Applied Physics Letters **76**, 3813 (2000).

[155] K. Gjerde, *Large Scale Integration of Carbon Nanotubes in Microsystems*, PhD thesis, Technical University of Denmark, 2006.

[156] K. B. K. Teo *et al.*, Applied Physics Letters **79**, 1534 (2001).

[157] A. Javey, Private Communication.

[158] L. Gammelgaard, S. Dohn, R. J. Wojtecki, A. Boisen, and P. Bøggild, Proceedings of MNE'06 , 3A6 (2006).

[159] W. Z. Li *et al.*, Science **274**, 1701 (1996).

[160] G. Binnig, C. F. Quate, and C. Gerber, Physical Review Letters **56**, 930 (1986).

[161] R. Berger *et al.*, Science **276**, 2021 (1997).

[162] J. Fritz *et al.*, Science **288**, 316 (2000).

[163] T. Thundat, E. A. Wachter, S. L. Sharp, and R. J. Warmack, Applied Physics Letters **66**, 1695 (1995).

[164] G. Meyer and N. M. Amer, Applied Physics Letters **53**, 1045 (1988).

[165] M. Tortonese, H. Yamada, R. C. Barrett, and C. F. Quate, Transducers'91 - 1991 International Conference on Solid-State Sensors and Actuators , 448 (1991).

[166] J. Thaysen, *Cantilever for Bio-Chemical Sensing Integrated in a Microliquid Handling System*, PhD thesis, Technical University of Denmark, 2001.

[167] C. L. Petersen, *Microscopic Four-Point Probes*, PhD thesis, Technical University of Denmark, 1999.

[168] S. Niyogi *et al.*, Accounts of Chemical Research **35**, 1105 (2002).

[169] H. T. Soh *et al.*, Applied Physics Letters **75**, 627 (1999).

[170] P. G. Collins, M. S. Hersam, M. Arnold, R. Martel, and P. Avouris, Physical Review Letters **86**, 3128 (2001).

[171] C. Schönenberger, A. Bachtold, C. Strunk, J.-P. Salvetat, and L. Forro, Applied Physics A **69**, 283 (1999).

[172] A. Kanda, Y. Ootuka, K. Tsukagoshi, and Y. Aoyagi, Applied Physics Letters **79**, 1354 (2001).

[173] M.-F. Yu *et al.*, Science **287**, 637 (2000).

[174] C. Buia, A. Buldum, and J. P. Lu, Physical Review B **67**, 113409 (2003).

[175] O. Hansen and A. Boisen, Nanotechnology **10**, 51 (1999).

[176] S. Rast, C. Wattinger, U. Gysin, and E. Meyer, Nanotechnology **11**, 169 (2000).

[177] R. Sandberg, K. Mølhave, A. Boisen, and W. Svendsen, Journal of Micromechanics and Microengineering **15**, 2249 (2005).

[178] J. L. Arlett, J. R. Maloney, B. Gudlewski, M. Muluneh, and M. L. Roukes, Nano Letters **6**, 1000 (2006).

[179] B. Lassagne *et al.*, New Journal of Physics **8**, 1 (2006).

[180] K. Mølhave, D. N. Madsen, S. Dohn, and P. Bøggild, Nanotechnology **15**, 1047 (2004).

[181] A. Tsumura, H. Koezuka, and T. Ando, Applied Physics Letters **49**, 1210 (1986).

[182] V. C. Sundar *et al.*, Science **303**, 1644 (2004).

[183] C. W. Tang and S. A. VanSlyke, Applied Physics Letters **51**, 913 (1987).

[184] G. He *et al.*, Journal of Applied Physics **95**, 5773 (2004).

[185] M. Era, T. Tsutsui, and S. Saito, Applied Physics Letters **67**, 2436 (1995).

[186] A. Hepp *et al.*, Physical Review Letters **91**, 1574061 (2003).

[187] C. Santato *et al.*, Synthetic Metals **146**, 329 (2004).

[188] F. A. Boroumand, P. W. Fry, and D. G. Lidzey, Nano Letters **5**, 67 (2005).

[189] H. Yamamoto *et al.*, Nano Letters **5**, 2485 (2005).

[190] M. Law *et al.*, Science **305**, 1269 (2004).

[191] A. L. Briseno *et al.*, Journal of the American Chemical Society **127**, 12164 (2005).

[192] I. D. Parker, Journal of Applied Physics **75**, 1656 (1994).

[193] Y. Shen, A. R. Hosseini, M. H. Wong, and G. G. Malliaras, ChemPhysChem **5**, 16 (2004).

[194] Y. Shen, M. W. Klein, D. B. Jacobs, J. C. Scott, and G. G. Malliaras, Physical Review Letters **86**, 3867 (2001).

[195] H. Ishii, K. Sugiyama, E. Ito, and K. Seki, Advanced Materials **11**, 605 (1999).

[196] H. Oji *et al.*, Journal of Electron Spectroscopy and Related Phenomena **101-103**, 517 (1999).

[197] N. Koch *et al.*, Advanced Materials **10**, 1038 (1998).

[198] N. Koch *et al.*, Applied Physics Letters **74**, 2909 (1999).

[199] J. C. Scott and G. G. Malliaras, Chemical Physics Letters **299**, 115 (1999).

[200] V. I. Arkhipov, E. V. Emelianova, Y. H. Tak, and H. Bässler, Journal of Applied Physics **84**, 848 (1998).

[201] M. A. Lampert and P. Mark, *Current Injection in Solids* (Academic Press, 1970).

[202] J. A. Geurst, Physica Status Solidi **15**, 1 (1966).

[203] V. I. Arkhipov, H. Von Seggern, and E. V. Emelianova, Applied Physics Letters **83**, 5074 (2003).

[204] P. S. Davids, I. H. Campbell, and D. L. Smith, Journal of Applied Physics **82**, 6319 (1997).

[205] T. Li, P. P. Ruden, I. H. Campbell, and D. L. Smith, Journal of Applied Physics **93**, 4017 (2003).

[206] H. B. Michaelson, Journal of Applied Physics **48**, 4729 (1977).

[207] R. W. I. de Boer *et al.*, Journal of Applied Physics **95**, 1196 (2004).

[208] D. J. Gundlach, Y.-Y. Lin, T. N. Jackson, and D. G. Schlom, Applied Physics Letters **71**, 3853 (1997).

[209] S. Tkaczyk and I. V. Kityk, Applied Surface Science **241**, 287 (2005).

[210] M. Pope and C. E. Swenberg, *Electronic Processes in Organic Crystals* (Oxford University Press, 1982).

[211] I. H. Campbell, T. W. Hagler, D. L. Smith, and J. P. Ferraris, Physical Review Letters **76**, 1900 (1996).

[212] C. Maibohm, J. R. Brewer, H. Sturm, F. Balzer, and H.-G. Rubahn, Journal of Applied Physics **100**, 054304 (2006).

[213] C. H. Clausen, Integration and characterization of *para*-hexaphenylene nanofibers, Master's thesis, Technical University of Denmark, 2006.

[214] S. Naka, H. Okada, H. Onnagawa, and T. Tsutsui, Applied Physics Letters **76**, 197 (2000).

[215] D. Engstrøm, Establishing hole/electron current and electroluminescence in para-hexaphenylene nanofibres, Master's thesis, Technical University of Denmark, 2006.

[216] J. Brugger *et al.*, Microelectronic Engineering **53**, 403 (2000).

[217] G. J. Dolan, Applied Physics Letters **31**, 337 (1977).